Elucidating Network Motifs and Improving Microcircuit Manipulations in the Primate Hippocampus

Aaron David Garcia

A dissertation

submitted in partial fulfillment of the

requirements for the degree of

Doctor of Philosophy

University of Washington

2023

Reading Committee:

Elizabeth Buffalo, Chair

Bingni Brunton, Chair

Sheri Mizumori

Anitha Pasupathy

Program Authorized to Offer Degree:

Neuroscience

University of Washington

Abstract

Elucidating Network Motifs and Improving Microcircuit Manipulations in the Primate Hippocampus

Aaron David Garcia

Chairs of Supervisory Committee:
Elizabeth Buffalo
Department of Physiology and Biophysics

Bingni Brunton
Department of Biology

The overall objective of this thesis is to elucidate previously unexplored nuances of hippocampal network communication while providing novel experimental and computational tools to motivate and enrich primate research. Much of the existing literature on the physiology and function of the hippocampus stems from work in rodents. However, while many anatomical features, physiological hallmarks, and reported functions of the rodent hippocampus translate well to studies in monkeys and humans, several primate-specific phenomena exist. Anatomical investigations reveal dramatic shifts in the organization of the hippocampus relative to other brain areas in the evolution from rodent to primate. Studies of continuous signals reveal that, in contrast to rodents, the primate hippocampus does not elicit continuous oscillations in recorded local field potentials (LFPs) as animals explore a given environment. Unfortunately, work in non-human primates (NHPs, monkeys) has historically lagged rodent hippocampal research in its conceptualizing of primate-specific theories of hippocampal function and

applying novel tools, such as gene manipulation techniques. However, recent technological advances are bringing work in NHPs to new prominence.

The work in this thesis presents several novel advancements in our theory of primate hippocampal function, our understanding of primate hippocampal physiology, methods for improving surgical methods related to genetic manipulations, and computational methods for analyzing noisy, non-stationary signals. In Chapter 2, I synthesize existing findings from the main cortical input to the monkey hippocampus, the entorhinal cortex (EC), to suggest that this region in primates is not just a simple relay to the hippocampus, but rather a diverse processor of multiple information streams that conveys highly specialized information to downstream regions. Chapter 3 contains a pipeline for planning and validating *in*-vivo the types of intra-cranial viral injections needed for genetic manipulation procedures such as optogenetics. Chapter 4 presents novel methods for detecting sharp-wave ripples (SPW-Rs) co-occurring across the monkey hippocampus during quiescence and provides the first evidence of species-specific motifs of traveling ripples across the entire longitudinal axis in primates. Finally, Chapter 5 introduces a novel method for mitigating artifact in large, noisy datasets while preserving the underlying signal, as well as a visualization technique to characterize non-stationary time series data. The overarching objective of this thesis serves to elucidate nuances of hippocampal network communication not previously explored and provide new tools, both hands-on and computational, to empower primate researchers to continue to explore the unique unknowns of the primate hippocampus.

TABLE OF CONTENTS

TABLE OF FIGURES

MAIN FIGURES

TABLES

SUPPLEMENTARY FIGURES

ACKNOWLEDGMENTS

There are many people who have helped make this thesis come to fruition. The following list is not exhaustive but represents a few folks who have made my journey possible and worthwhile.

To my mentors Beth and Bing: Thank you for taking a chance on me, and giving me multiple avenues to grow and learn. I know at times the ship looked lost in the night, but I’m grateful for your guidance through all the unknowns to reach this point.

To Jon: Thank you for your friendship and mentorship. You are the best big science brother a fledgling could ask for. You have looked out for me since day 1, and although our paths collided a few times in the tail end of things, I am beyond happy that we got to finish on the best collaborative note.

To Aaron Dean: Thanks for always being the best hunk and commiserator a lil amigo could ask for. I’m pumped for your turn.

To Emily Payne and Derek Brickey: We’re a bit scattered these days but I love you guys, and I appreciate your friendship and support through this weird period of doctoral funkiness.

To Raymond Sanchez, Rapheal Williams, Michael Kiflezghi, Mohammad Tariq, and Ryan Farero: None of this would be possible without you all going through the process with me and helping me figure out all the tubular BS that comes with navigating graduate school. Your guys’ friendship has made this process worth it, and I am beyond elated to see how our friendships continue to grow. Go Soft Bodies.

To the Familia Garcia: I am fortunate enough to have been supported in my wild endeavors by my family, despite them not always understanding what exactly I have spent almost a decade working towards. I am grateful for your love, and I am looking forward to more regular visits and family parties!

To Kara, Rusty, and Dot: You three girls make my world go round. I love you all. Kara, you are the love of my life, and I am grateful that you were willing to put up with all my grouchiness while writing this manuscript. Thank you for being you, Bub. I love you.

CHAPTER 1 || INTRODUCTION

The hippocampus is one of the most prolifically studied brain areas and has garnered heavy scientific attention since early anatomical dissections of the hippocampal formation in ancient Egypt (1). Despite centuries of research, this area continues to enthrall neuroscientists looking to better understand various phenomena ranging from evolutionary anatomy to electrophysiology to neuropathological diseases such as Alzheimer's Disease (1). Investigations into this structure have even received a Nobel Prize for elucidating how the rodent hippocampus maps a given environment (2,3). Yet, our historical understanding of the function of the hippocampus has changed dramatically over the years (1), and even the Nobel-prize worthy theories that the function of the hippocampus is to provide cognitive maps of traversed space are not widely accepted amongst hippocampal researchers (4,5,13). The divide further widens when considering the hippocampus in translation across different species. Lesions to and electrical recordings from the rodent hippocampus across several labs reveal amnesic effects and the previously mentioned neuronal responses to space, respectively (3,6). However, efforts to identify the same effects in primates are varied at best (7-10). Evolutionarily, part of the observed differences between the primate and rodent hippocampus stem from large conformational changes of these structures in the brain, divergent proportions of different cell populations, and species-specific intrinsic and extrinsic connectivity patterns (11,12). As a result of these changes, several state-of-the-art techniques used to catapult our understanding of rodent hippocampal physiology and function have historically been either severely limited or impossible to conduct in this species.

This chapter serves primarily to review existing findings on hippocampal anatomy, physiology, and function from both rodent and primate work. I will discuss findings from anatomical, lesion, electrophysiological, and genetic manipulation studies of the hippocampal formation to highlight convergent and divergent features across the rodent and primate hippocampus, lapses in our understanding of various aspects of primate hippocampal physiology, and the difficulty in performing surgical procedures associated with state-of-the-art genetic manipulations in the primate hippocampus. The main body of this thesis subsequently addresses these items. In chapter 2, I provide a through review of existing literature on the primate entorhinal cortex to suggest an elevated role of cortical information processing within this structure. In chapter 3, I develop and successfully implement a novel surgical pipeline to improve planning and targeting strategies, which can subsequently be validated *in-vivo* up to 24-hours post-procedure. Chapter 4 leverages high-density electrophysiological recordings in the primate hippocampus to provide the first evidence for intra-regional communication across the entirety of the structure. Finally, in Chapter 5 I develop novel tools for de-noising and visualizing large, noisy datasets of continuous signals, and I apply these tools to both simulated data and local field potentials collected from the primate hippocampus. When applied to the hippocampal recordings, I successfully show subregion-specific oscillatory profiles that are present only when animals are engaged in goal-dependent behaviors. With these novel postulations and findings, the overall aim of this work is to continue advancing our understanding monkey hippocampus and motivate a new era of research in this species and structure.

1.1 WHAT IS THE HIPPOCAMPUS?

1.1.1 ANATOMY AND HISTORICAL PERSPECTIVES

The hippocampus is one component of the larger hippocampal formation (HF), which is located deep within the primate medial temporal lobe (15,16). The broader HF is a group of structures that includes not just the hippocampus proper (the CA fields), but also the dentate gyrus, the subicular complex (subiculum, presubiculum, and parasubiculum), and the entorhinal cortex (15). This tissue runs along the floor of the lateral ventricles and earned its name from anatomical dissections that revealed a peculiar seahorse-like shape of this tissue (1). Classifications of hippocampal cytoarchitecture by Ariens-Kappers and Brodmann would reveal a predominantly three-layered cortex, with only one distinct cell layer compared to more elaborate five- and six-layered cortices (16). Because of this simplicity, it was dubbed allocortex (“strange cortex”) and archicortex (“old cortex”) (16). Not included in this distinction were the entorhinal cortex, presubiculum, and parasubiculum, which had a six-layered structure and were coined peri-allocortex since they surrounded the allocortical hippocampus (16). However, the other areas that were counted as archicortex were those of the olfactory system. Because of the proximity between and similarity of these regions, some of our first theories of hippocampal function were that this area was merely an extension of smell processing (1,16,17). However, in a 1947 review of hippocampal literature, Alf Brodal would debunk this theory with the pivotal claim that olfactory bulb efferents did not innervate the rodent HF at all and that the hippocampus proper played no role in olfaction (17). He claimed that entorhinal cortex had a minor role by way of secondary communications with other areas innervated by olfactory cortices. Modern neuroanatomical studies would refute this claim with the discovery of direct projections from the olfactory bulb, piriform cortex, and other areas to the entorhinal cortex (18). With entorhinal being the largest input into the hippocampus, one might expect some influence of olfaction on hippocampal function. To this point, Brodal would presciently state that the entorhinal cortex is responsible for sensory integration rather than pure olfactory processing (17).

Spurred by the debunking of this olfactory hypothesis and unique connectivity with subcortical structures, the next prominent theory would be championed by James W. Papez, who claimed that the HF was critical for emotional processing (19). The theoretical Papez circuit was based off connectivity from the HF to the hypothalamus, anterior thalamic nuclei, the anterior cingulate gyrus, and back to the HF. Investigations by Kluver and Bucy would seemingly support this theory, as lesions to the medial temporal lobe of monkeys severely dampened the animals' responses to pre-operatively fearful stimuli (20). Unfortunately, work by the late Mortimer Mishkin, John Aggleton and others would show that it was not the hippocampus but the amygdala that was responsible for a loss of fear response in these animals (21,22). However, another symptom of the Kluver-Bucy lesions was a profound memory impairment in lesioned animals. They constantly experienced objects as though they were novel, even after long windows of engagement with the stimuli. Similar findings were observed by Brown and Shafer half a century earlier and serendipitously provided some of the earliest evidence of a hippocampal role in memory formation (23).

The most influential insights into the role of the HF in learning and memory came from the observations of human patients with epilepsy, such as the famous Patient H.M (7). After surgical bilateral lesions to his medial temporal lobe to cure his intractable epilepsy, H.M. suffered profound retrograde and anterograde episodic amnesia. Specifically, he could neither remember facets of his life that occurred within a decade of his procedure, and despite retaining the ability to learn new skills and complete rote memory tests, he was incapable of forming new memories of his experiences post-operatively (7). While much debate remains in the field and will be discussed below, one of the leading dogmatic theories is that the hippocampus and broader HF are critical for learning and memory.

1.1.2 THE MODERN ERA DEBATE OVER HIPPOCAMPAL FUNCTION

The early observations of Patient H.M. and related findings in rodents paint a rosy picture that the HF is critical for the processing of episodic memories. However, attempts at discerning the specific role of the structures within the HF have been fraught with much argument and disagreement in the field. In rats, lesions limited to the hippocampus proper produce profound navigational memory deficits (24), spatial memory deficits across various delays (25), and even relational memory deficits in behaviors with complex hierarchical associations (6). These findings, combined with evidence from neuroanatomical (26) and electrophysiological studies in the rodent (discussed in Sections 1.2.3 & 1.3), introduced a framework by which spatial information from an experienced event is processed by neocortical and HF areas in a parallel but functionally unique stream from temporal and object information (27). Under this model of memory formation, the hippocampus proper sits as the critical head of memory formation by combining the “where” information with the “what/when”. This theory, which was championed by the late Howard Eichenbaum, seemed like a perfect explanation for a hippocampal role in memory processing. However, results from primate lesion studies provide inconclusive results that the hippocampus is necessary for either spatial, temporal, or relational memories (9,28). In a comprehensive combination of meta-analysis and novel experiments, Basile and colleagues revealed that focal lesions to the primate hippocampus fail to produce impairments on multiple classical testing paradigms, including transitive inference, source memory, and temporal-order memory (9). Impairments in spatial memory after primate hippocampal lesions have been observed (29,30), but even such findings have been challenged (31). In personal conversations with Dr.

Eichenbaum, he suggested that overtraining animals on limited recognition paradigms led to behaviors that simply were not hippocampal dependent*. This hypothesis has been echoed by others in the field (32). However, an alternative hypothesis was posed to me during anecdotal conversations with Dr. Mishkin, who claimed that our assignment as a field of the hippocampus as the “seat of memory” was misguided and failed to address the critical role of the entorhinal cortex in memory processing[1].

1.1.3 THE OVERLOOKED PROCESSOR OF INFORMATION FLOW TO THE HIPPOCAMPUS: THE ENTORHINAL CORTEX

It would be tremendously naïve to say that we know nothing about the entorhinal cortex (EC; Brodmann Area 28) or its role in learning and memory. Anatomically, the EC sits behind the hippocampus proper in rodents and occupies the most postero-ventral position of the rodent brain. Perplexingly, this region undergoes a significant migration in primates and is located anterior to the hippocampus in the most antero-ventral portion of the temporal lobe (11). This makes it incredibly difficult to access in primates, and as such only a handful of lesion studies and electrophysiological recordings have been performed in this structure. Yet, this limited body of work strongly parallels findings in rodent research, which is in stark contrast to the inconsistencies observed from the hippocampal lesion work described in the previous section. As mentioned, the historical perspective on EC is a bifurcated subdivision between the medial EC (MEC) and lateral EC (EC), which handle “where” and “what/when” information, respectively. However, new research suggests a more complicated and conjunctive organization of information processing in the entorhinal cortex of rats (33). Bilateral lesions to the entorhinal cortex impair acquisition of delayed spatial alternation tasks (34). Yet, in work performed by myself and others in Howard Eichenbaum’s lab, we found that temporary lesions to the rat MEC during mnemonic delays in a non-spatial object discrimination task

---

[1] Personal conversations with Mishkin and Eichenbaum during meetings on these issues while in their respective labs.

severely impair behavioral performance (35). Importantly, this deficit was specific to the delay, such as when animals were required to hold stimulus information in memory. No performance detriments were observed when EC was inactivated during non-task-relevant epochs, such as running around the maze to begin a new trial, or during object sampling. These findings mirror lesion studies in primates that show a specific role of EC in holding information across mnemonic delays (36). Moreover, in non-spatial behaviors, lesions to the primate EC are particularly detrimental when complex relationship between stimuli are required to be remembered (37), including during tasks that are not affected by hippocampal lesions (9).

Rather than serving as a strict input structure to the hippocampus, these findings suggest—in primates especially, that the EC itself is critical for memory formation and retrieval. Yet, much of the current school of thought still minimizes the influence of EC and considers this area a simple updating relay and support structure to the hippocampus in attractor-style network models (13,38). For these models, the critical seat of memory processing is the hippocampus itself rather than the EC. In Chapter 2 I challenge this idea and show through a comprehensive review of existing neuroanatomical and neurophysiological evidence in primates that the EC has evolved to be a complex processor of conjunctive information rather than a passive relay of information (published in 12). I highlight novel findings across species and motivate further research to bolster our understanding of the anatomical and functional features of this critically important brain area for memory processing.

1.1.4 NEURONAL RESPONSES IN THE HIPPOCAMPUS

Although the main work in this thesis does not concern itself with the activity of putatively identified single neurons in the hippocampus, it is important to briefly touch upon identified roles of single unit activity (SUA) across the hippocampus and HF at large in order to better understand some of the rationale behind contemporary theories of hippocampal function. The now famous investigations of rodent hippocampal neurophysiology by O’Keefe and Dostrovsky revealed that principal cells in the CA fields hippocampus only fire action potentials when animals are in a particular location in an environment (2).

These findings have been replicated numerous times over the years (39,40), and similar “place cell” phenotypes have also been observed in the dentate gyrus (41,42) and subiculum (43-45). Across a population, the various place fields have been shown to tile an environment and, depending on what aspect of the hippocampus one is recording from, populations and individual units will remap as animals are exposed to multiple, unique environments (41-46). Hippocampal place cell findings were bolstered by the observations of other types of spatial responses in other aspects of the rodent HF. In the subiculum, place responses are observed in conjunction with neurons that respond when animals are facing in a particular direction (head direction cells) or are a set distance from environmental borders (border cells/boundary vector cells) (43,44). In addition to head direction and border cells, the EC of rodents elicits grid cell firing patterns, which consist of multiple firing fields from single units that tile an environment in a regularly spaced, triangular pattern (3,47). Place selectivity in the primate hippocampus is a burgeoning field, and investigations suggested that animals’ viewing position mattered more than their physical location in space (10, 48). Work from our lab has identified view cells in the monkey hippocampus both in 2-D and 3-D visual environments (49,50), grid cells in the primate EC that elicit regular firing fields tiling visual space (51), and even head direction cells (51).

While this evidence supports the role of the HF as a series of spatial “cognitive maps” (4,5), non-spatial responses from rodent and monkey hippocampal neurons that track temporal delays (52, 53) and respond only during salient phases of spatial and non-spatial tasks (54, 55) have motivated novel models of hippocampal function. These models deviate from standard cognitive map theories and propose topological/relational frameworks by which the HF orders experiences (13, 28, 56), as opposed to older models bound by rigid spatiotemporal dimensions (4, 57). In these models, the periodicity of grid cells is generated predominantly by extrinsic sensory inputs, and the conjunction of multiple grid inputs onto hippocampus neurons produces the more selective place cell firing. Multiple place cells become intrinsically linked together over the course of learning, and these connections are further facilitated by the periodicity of grid cell input. Unfortunately, this precisely describes the EC as an updating relay, as discussed earlier. In Chapter 2 I provide evidence from the primate literature elucidating the potential for more elaborate neuronal responses in the primate EC.

1.2 HALLMARKS OF SYNCHRONY IN THE HIPPOCAMPUS

1.2.1 MEASURING SYNCHRONY

The study of mesoscopic neural synchrony has its roots in the occult and mystical. In the early 20th century, Hans Berger, a scientist and soldier in the Prussian army received a letter from his sister in which she had a premonition that he would fall off his military horse and break his leg (reviewed in 58). Supposedly, as he was reading of this his horse bucked him off, breaking his leg. Believing that some telepathic force allowed willed this premonition into existence, Berger would go on to investigate whether electromagnetic forces arising from the brain were sufficient to induce telepathic communication between brains. To study this, he placed electrical contacts on the scalp of himself and other subjects and inadvertently performed the first recordings of synchronous neural activity (58). This technique would be coined electroenchephalograpahy (EEG) and now represents an entire field of recording continuous activity from large populations of neurons (58). The continuous EEG signals reflect the rhythmic fluctuations of the extracellular gradient of ions generated by millions of post-synaptic potentials. The activity of neuron is too low amplitude to detect through these types of recordings, and similarly the syncopated or de-synchronous activity of a population tends to produce faster, noisier, and lower amplitude signals. By contrast, more synchronous brain areas produce larger, slower waves of activity. EEG performed on the scalp has poor spatial resolution and determining the brain areas responsible for observed oscillatory fluctuations can be challenging. However, the development of macroelectrodes capable of being surgically placed into the brain has allowed for EEG recordings predominantly from neurons in putative area(s) of interest. Because the electrical field induced by post-synaptic potentials now reflects local changes near the electrode tip, these recordings are called local field potential (LFP) recordings.

LFP signals are typically amplified during recordings, and because the recording electrodes are effectively tuning into all electrical activity strong enough to travel to the recording site, recorded neural activity can become contaminated by artifactual noise. Particularly devastating artifacts may arise from such sources as blinking and eye movements, electrical line noise, chewing, and even mechanical noise, and special care needs to be taken to ensure recorded signals only reflect the local neurogenic signal (reviewed in 59). Nevertheless, studies of LFP and its relationship to behaviors highlight the tremendous role of synchronous neuronal oscillations at illuminating hallmarks of functionally relevant activity. Recordings from motor cortex reveal unique hallmarks of motor planning (60), motor movement execution (61), the direction of a movement (61), and even applied force (62). In the hippocampus, LFP recordings of synchronous activity have helped us better understand systems-level mechanism of memory encoding, consolidation. Moreover, they reflect unique circuit-level mechanics for processing serially experienced information, such as that experienced during episodic memories.

1.2.2 OSCILLATIONS IN THE HIPPOCAMPUS DURING ACTIVE EXPLORATION

Early LFP recordings in the hippocampus of freely moving rabbits (63) and rodents (64, 65) revealed a large, slow, long-lasting oscillation that appeared to dominate the electrical recordings while animals were actively moving around in an environment. These slow waves, occurring between 6 and 12 Hz in these rodents, were dubbed theta oscillations and seemingly reflected large-scale hippocampal engagement during active behaviors and locomotion. Theta oscillations have been shown to correlate with animals' speed as they traverse an environment (66) and synchronize with behaviors they use to explore an environment (67). However, the most pivotal findings of the importance of theta come from our understanding of this oscillation's relationship to ordered place cells firing. As rodents run around, hippocampal neurons are continuously discharging their place fields (Section 1.2.3) concurrent with the more global theta oscillations in the LFP record. What Skaggs, Buzsaki, and others showed was that the firing of neurons with adjacent place fields in familiar environments occurred in short, advancing sequences as animals traversed space (38, 68, 69). Importantly, they observed that these sequences were bracketed by windows of inhibition observable in the theta oscillation. Cells with place fields in the rats' current position fired at the trough of the theta oscillation, when disinhibition is at its maximum. Navigating from that position produces firing at earlier phases for that neuron and firing at the theta trough by cells representing the updated position of the animal—this phenomenon is known as phase precession (38, 68, 69). When the medial septum, a subcortical pacemaker responsible for one of the dominant modes of hippocampal theta synchrony, is disrupted, theta virtually disappears in all regions within the HF (70, 71). Importantly, grid cell spatial periodicity in EC changes drastically (70) while place fields largely maintain their spatial information content (71). Despite this preserved place information, the disruption of theta severely impairs memory-guided and navigatory behaviors, thus suggesting that the organization provided from theta-paced organization of hippocampal cell assemblies is critical for memory (71).

In both freely moving and head-fixed primates, theta is not as consistent during exploratory behaviors (48, 72). Work from our lab and others provides evidence instead for short bouts of similar frequency oscillations in the primate HF (48, 72). These oscillations synchronize with eye movements similar to the synchrony observed with rodent theta and sniffing and whisking and also correlate with better memory performance in visual matching behaviors (72). Intriguingly, in freely moving monkeys the frequency of observed theta bouts inversely correlates with the speed of the animals' movement (48). Moreover, only a small subset of cells was shown to phase precess in the primate hippocampus, suggesting species-specific differences in the organization of cell firing by global processes (48). A compounding factor may be that the LFP of higher-order organisms such as primates may reflect non-oscillatory, or at least non-stationary processes that jump through many different frequency states during active exploration. This has been shown in bats, where novel methods were employed to detect phase locking and phase precession were detected in the hippocampus and entorhinal cortex across a range of rapidly and dramatically changing frequencies (73). Similar methods to identify non-stationary traveling waves have also recently been developed that do not force a rigid frequency when determining relevant signals (74).

The other set of waking oscillations observed during active exploratory behaviors are the fast gamma rhythms in the hippocampus, which are fast, low amplitude rhythms ranging from 25-90Hz and are often nested within the larger amplitude theta rhythms in rodents (38, 65). These gamma rhythms have been shown to reflect rhythmic inhibitory post-synaptic potentials from hippocampal interneurons (reviewed in

38), and studies with selective inhibitory agents revealed two functionally distinct gamma modes: a slow gamma (~25-50Hz) and fast gamma (~60-90Hz) (65). Modulation of hippocampal subregion CA1 fast gamma has been observed by manipulating inputs from the EC, whereas manipulating CA3 inputs alters the presence of slow gamma (38). Slow and fast gamma have been suggested to have different roles in memory function, and despite some debate over specifics, it appears that both play similar, if not complimentary roles in memory processing (38). In primates, both low and high gamma in the hippocampus have been observed, and work from our lab has shown a direct relationship between hippocampal gamma and memory performance (48, 75). In animals performing a preferential looking task in which novel items hold focus and gaze more than familiar stimuli, recorded gamma band oscillations and spike-amplitude coherence with both low and high gamma reflected improved recognition of familiar stimuli (75).

Unfortunately, work on primate hippocampal LFP does not specify ontogeny at the sub-region level for waking oscillations (and quiescent rhythmic activity discussed in Section 1.3.2). It has been shown in rodents that theta rhythms emerging in CA1 and CA3 have offset phase relationships and arise from different sources (65). Moreover, the fast and slow gamma rhythms that arise in the hippocampus have different ontogenies. One stems from EC input to CA1 and the other from CA3 (38, 65). Because of the acute nature of recordings in traditional primate EEG studies, such functional distinctions are nearly impossible to deduce. While novel recording technologies implemented in our lab and others using chronically implanted high density drives are beginning to come online (48, 50, 76), more work needs to be done to validate what homologous sub-regional interplay of LFP signals exist in the primate HF. In Chapter 5 I will address both dilemmas and utilize novel analyses from high-density, chronic implanted EEG arrays to analyze the non-stationary signals within the primate HF.

1.2.3 OSCILLATIONS OBSERVED DURING SLEEP AND QUIESCENCE

In contrast to the regularly occurring, highly oscillatory phenomena observed in rodent hippocampal LFP during active exploration, during sleep and quiescence this region is remarkably quiet. Intermixed with this relative silence are sporadic phenomena initially called large irregular activity and now known as sharp-wave ripples (SPW-R) (38,65). SPW-Rs are two simultaneously occurring LFP phenomena with a slow and fast component. The slow component is known as a sharp wave and is a large amplitude, sharp, single deflection in the electrical signal lasting 40-100ms. Nested within the sharp wave is a lower amplitude fast oscillation between 100-200Hz. SPW-R complexes have been observed in humans during recollection of episodic memories (77), and evidence for SPW-R involvement in memory consolidation has been shown in rodent neurophysiology experiments. In these experiments, the same theta-driven sequences of hippocampal place cells observed during active exploration fire in the same ordered pattern during subsequent epochs of sleep (38, 78). Interestingly, these reactivated sequences unfold in a temporally compressed manner relative to their activation during exploration, and these "replays" observed during awake ripples correlate with remembering alternative choices after training on complex memory paradigms (79). Inactivation of SPW-Rs during long periods of quiescence after training on memory-dependent paradigms also induces severe memory deficits during subsequent testing, highlighting a causal role of this phenomenon in memory consolidation (80).

The presence of SPW-Rs is conserved in primates, and this phenomenon is largely similar in form and function to those identified in rodents (81,82). Ripples in primates also elicit an inhibitory post-ripple wave that is a large, slow deflection in the LFP that occurs after a ripple and reflects a system-wide period of inhibition after the synchronous excitation (82). These refractory waves are weakly present in rodents (83), and what makes them more prominent in primates is unclear. Moreover, the identification of ripples along the longitudinal axis of the hippocampus has yet to be performed because of limited spatial specificity and sparsity of acute recordings. In Chapter 4 of this work, I identify the prevalence of SPW-Rs across the longitudinal extent of the primate hippocampus using chronic, high-density recordings. I provide the first evidence for ripples with complex topographical relationships along the hippocampus. Importantly, I discover that ripples can travel throughout the entire longitudinal axis of the primate hippocampus, which is a divergent feature from traveling ripple motifs identified in rodents and reflects primate-specific communication with downstream structures such as the prefrontal cortex (83, 84).

1.3 APPLYING GENETIC TECHNOLOGIES TO STUDIES OF HIPPOCAMPAL FUNCTION

Our present discussion of the function and physiology of the primate HF has continually mentioned the limitations of the methodology typically employed. Unfortunately, similar limitations also exist that hinder primate researchers' abilities to perform state-of-the-art genetic manipulations, such as opto- or chemo-genetics. Specifically, the position of the primate HF at ventral levels of the temporal lobe makes it a difficult target to reliably target, and the multi-centimeter long, tubular shape of the hippocampus makes injecting viral payload to this structure non-trivial. When combined with unknowns related to viral expression (I.e. knowing what viruses will successfully infect cells in the structure), viral methods contain too high a risk for researchers looking to perform causal experiments. Thus, the main method of manipulating the hippocampus is to lesion it, and while lesions still carry accuracy and completion of removal, even successful lesions produce unintended damage to surrounding structures (29-31). Additionally, long post-operative recovery time may induce unintended plasticity, which confounds findings of impairment (36). To circumvent issues such adaptive plasticity, applying trans-genetic tools to primate research is integral to improving our ability to draw better conclusions about hippocampal functions. Rather than standard lesions, methodologies such as optogenetics can be utilized in theory to provide focal transient lesions. In optogenetics, a genetic subset of the neural population is infected with light-sensitive channels that activate in response to light of a particular wavelength. In rodents, infecting the EC indiscriminately with inhibitory optogenetic channels reveals a dependency on EC for proper time cell organization and working memory function (35). The beauty of this technique is that it allows for within-session control testing, such as inactivating during various task phases or running trials with no inactivation. Aside from surgical limitations, optogenetic procedures in the hippocampus may still be limited by the degree of viral expression, as well as light spread to a sufficient volume of the structure. However, successfully applying these temporary lesions to monkeys would dramatically improve our ability to ascribe function to distinct brain areas. In the case of animals performing memory-dependent behaviors, successfully inactivating EC repeatedly may show sustained behavioral impairments and no sporadic plasticity across the tenure of the experiment as opposed to the transient effect and adaptive plasticity observed in (36). Similarly, optogenetically tagging a subset of glutamatergic neurons from the medial septum, which is upstream from the hippocampus and is a major driver of the theta oscillation, has proved incredibly useful in studies looking to observe the preferred frequencies of oscillations within the hippocampus (86). Selective tagging of hippocampal ensembles only during particular behaviors can even be used to reproduce learned behaviors of a particular type in novel conditions, or at the wrong time (87-88).

The primate field is already beginning to adopt these new techniques in structures adjacent to the HF to identify time-dependent changes in object recognition (89). However, adopting this technique in the hippocampal field is not without its challenges. Firstly, primates are an expensive, scarce resource. Whereas rodent studies may be performed on as many as a hundred mice (85), typical primate experiments have under ten subjects (9, 10, 21-23, 29, 30, 48-51, 55, 72, 76, 81, 82). This scarcity means that primate researchers cannot haphazardly pilot new procedures to test the best possible application of a novel technique. As alluded to earlier, injection procedures are typically performed without in-vivo validation of accuracy, and researchers typically must wait ~two months before assessing a successful infection through testing. However, an unsuccessful infection could be the result of either surgical/payload delivery error or because the virus itself failed at successfully infecting cells of interest. Unfortunately, traditional surgical methods prohibit disentangling surgical errors from viral failures because injections are performed blind in the operating room with no in-vivo validation of targeting and payload spread. Thus, the widespread utilization of these novel techniques is often fraught with much hesitation and concern. In Chapter 3 of this thesis, I present a pipeline that combines computational, benchside, and in-vivo techniques to ameliorate the surgical unknowns present in typical intracranial injections. This method utilizes an infusion technique to rapidly deliver viral agents across a large, uniform area, and I provide a model based off in-vivo injections to estimate the expected spread of a viral agent relative to the volume of a given infusion across a wide array of brain areas. Additionally, I provide an *in vivo* validation method that builds upon existing methods for co-infusing with MRI-compatible radiolabels to visually validate the injection accuracy and spread up to 24-hours postoperatively.

1.4 CONCLUSIONS AND RATIONALE FOR THIS WORK

Ultimately, work in understanding the primate HF has come a long way but has a long way yet to go. This thesis joins the growing body of modern work aimed at both providing direct insight into hippocampal function and providing new theories and tools to motivate new generations of hippocampal research. The authors maintain that a critically understudied portion of the primate hippocampal formation is the entorhinal cortex, and despite our many insights into its function and physiology over the years, the difficulty in accessing this structure has served as a prohibitive block for asking more eloquent questions that match the nature of those asked in rodents. The logistical, financial, and biological challenges with applying novel tools to questions like these and others similarly hinders the scope of questions researchers can ask. Our lab has pioneered some of the first high-density chronic arrays for depth EEG recordings, and although various oscillatory phenomena have been well documented in primates during active exploration and quiescence, our specific understanding of concepts such as dominant oscillatory modes and propagating waves of synchrony remains to be tested. Similarly, the types of computations that I use to answer these types of questions requires a severe update.

I hope that readers of this thesis gain knowledge and inspiration from reading this body of work. I hope that the tools, techniques, and findings presented provide meaningful insights that help facilitate current experiments, and I hope that our theories help motivate novel ones.

CHAPTER 2 || ANATOMY AND FUNCTION OF THE PRIMATE ENTORHINAL CORTEX

Chapter adapted from published work: **Garcia AD**, Buffalo EA. *Anatomy and Function of the Primate Entorhinal Cortex.* Annu Rev Vis Sci. 2020 Sep 15;6:411-432. doi: 10.1146/annurev-vision-030320-041115. Epub 2020 Jun 24. PMID: 32580662.

2.1 INTRODUCTION

The hippocampal formation has long been implicated in learning and memory (Milner 1972, Mishkin 1982, Squire & Zola-Morgan, 1983; Squire & Zola-Morgan, 1991). The entorhinal cortex (EC) is a critical element of this network of integrated structures and receives a wide array of converging inputs from polymodal sensory association cortices, as well as subcortical arousal areas (Brodmann & Garey 2006). In turn, the EC itself is the major source of cortical input into the hippocampus proper. The first reported investigations into the EC came from dissections in rodents performed by Santiago Ramón y Cajal in the early twentieth century. His findings highlighted a portion of rat cortex with substantial reciprocal connections with the hippocampus. Ramón y Cajal (1899) posited that this rich interconnectivity strongly implicated this cortical region as necessary for proper hippocampal function. This hypothesis inspired the current dogma of the EC as a gatekeeper of cortical communication with the hippocampus and has shaped the ways in which this structure has been studied (Amaral et al. 1987). As such, it will come as no surprise that the bulk of contemporary work on EC function has focused on elucidating how the physiology of this structure facilitates hippocampal processing. This field has been driven predominantly by research in rodents performing spatial navigation paradigms (Burgess et al. 2007, Hafting et al. 2005). Through this work, medial (MEC) and lateral (LEC) subdivisions of the rodent EC have been identified that are distinguishable by both their anatomy and their function (Witter et al. 2017). While EC input is limited to the distal two-thirds of the molecular layer of the dentate gyrus (DG), MEC projects to the middle third, whereas LEC projections terminate on the outer third (Witter 2007). Functionally, MEC's constituent cells, including grid cells, are largely driven by allocentric spatial reference frames (Hafting et al. 2005, Sargolini et al. 2006, Solstad et al. 2008). By contrast, LEC neurons have been reported to elicit temporally modulated firing patterns (Tsao et al. 2018), as well as responses to specific objects, regardless of where in space those objects exist (Deshmukh & Knierim 2011, Tsao et al. 2013).

While these findings in the rodent EC have had a significant impact on the trajectory of primate research, several incongruences arise when directly comparing this structure across species. Anatomically, the EC takes a much more rostral position in the primate temporal lobe than in the rodent; in the primate, it sits largely anterior to the hippocampus. Additionally, whereas the EC in rodents is flatter and more ellipsoid, this structure adopts a C-like shape in primates (Strange et al. 2014) (Figure 1a). The primate EC contains more pervasive connectivity patterns with visual processing areas compared to that of the rodent (Burwell 2006, Insausti et al. 1987a), a fact that is likely explained by the reliance of primates on vision as their primary exploratory modality, compared to olfaction in rodents (Schroeder et al. 2010). Given the cognitive deficits associated with Alzheimer's-derived atrophy of the EC—one of the initial neuropathologies in humans with this disease (Khan et al. 2014)—it is imperative that we continue to investigate the relationship between this structure's physiology and higher-order cognitive processes, including episodic memory. In this review, we synthesize the growing field of primate EC research aimed at doing just that. We examine how recent research has both elaborated on findings from rodent studies and identified key differences between species. First, we review the anatomy of the primate EC, highlighting its privileged position: The EC serves as a conduit to the hippocampus and as a remarkably efficient site of information convergence. Second, we discuss the diverse network of communications within the hippocampal formation, including interactions between the EC and hippocampus, as well as the robust intrinsic connectivity within the cortical layers of the EC. Finally, we discuss how these anatomical findings have motivated ideas regarding EC function, and we review the lesion and neurophysiological studies that have examined various functional hypotheses. Clearly, the field has made significant headway in uncovering the function of the EC; however, the emergence of new tools for neurophysiological recordings and targeted manipulations have the potential to dramatically increase our understanding. We hope that this review will inspire and motivate further studies of this structure in the primate.

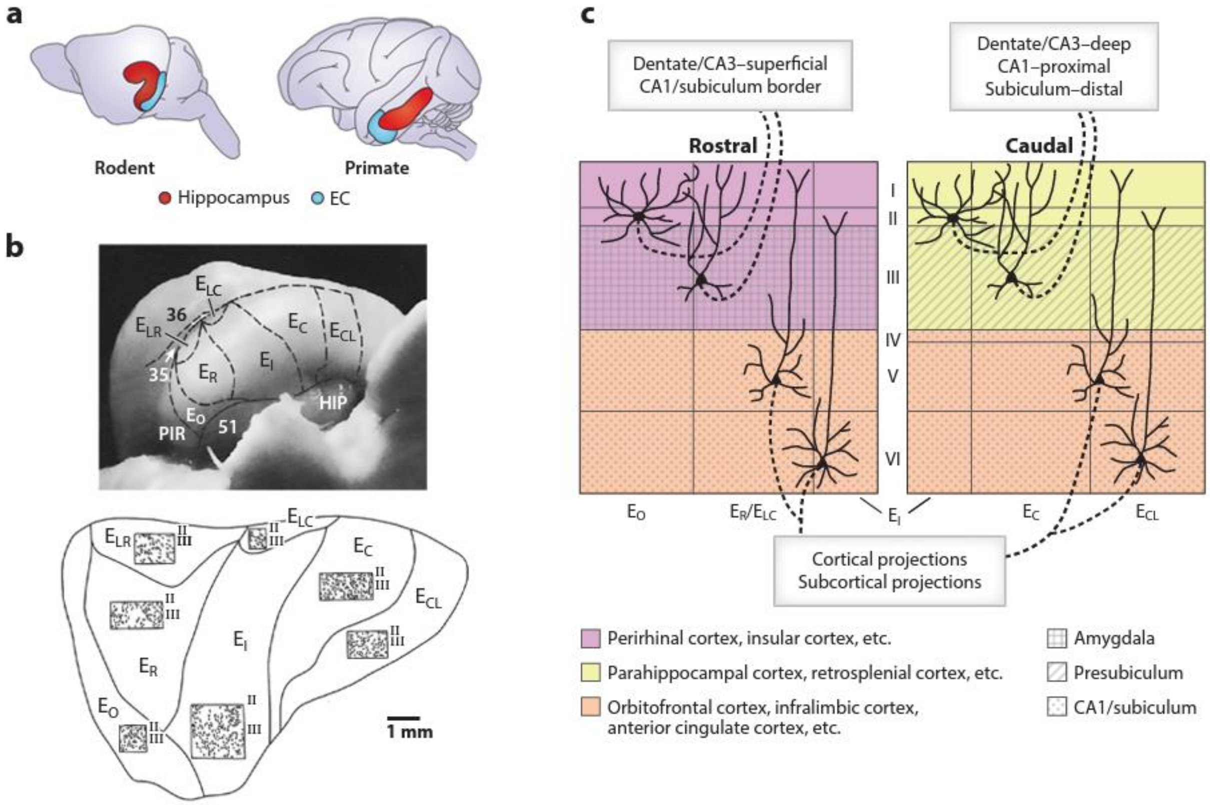

Figure 2.1 The Primate Entorhinal Cortex, its Subdivisions, and Major Connectivity Patterns

(A) Illustration showing the variation of anatomical placement of the entorhinal cortex (EC) between rodents and primates. Panel adapted with permission from Strange et al. (2014). (B) Photomicrograph of the ventral surface of the temporal lobe and flattened illustration of EC subfields as defined by Amaral et al. (1987). Note the change in Layer II and III cell density across the different subregions. Panel adapted with permission from Amaral et al. (1987) (EO: Olfactory EC, ER: Rostral EC, EI: Intermediate EC, ELR: Rostro-lateral EC, ELC: Rostro-caudal EC, EC: Caudal EC, ECL: Caudo-limiting EC). (C) Schematic of major EC connectivity. Panel adapted with permission from Insausti et al. (1987a).

2.2 WHAT IS THE ENTORHINAL CORTEX?

2.2.1 ETYMOLOGY AND ORIGIN

In the primate, the EC is situated in the anterior medial temporal lobe (MTL). It begins ventral to the amygdala and anterior to hippocampus. From there, it extends caudally underneath the hippocampus for approximately 5 mm. The earliest usage of the term “entorhinal cortex” was given by Brodmann after his dissections of human tissue, during which he identified a cortical field extending medially from the rhinal sulcus (Brodmann’s area 28) with distinct cytoarchitecture from the tissue surrounding the sulcus (perirhinal cortex; Brodmann’s area 35) and the tissue extending laterally from it (ectorhinal or inferior temporal cortex) (Amaral et al. 1987, Brodmann & Garey 2006).

2.2.2 CYTOARCHITECTURE

Despite the EC being recognized as an independent brain region by its unique cytoarchitecture, anatomists have historically been in disagreement over this region’s exact cytoarchitectonic composition. Ramón y Cajal (1899) proposed a seven-layer architecture in his initial dissections, although follow-up investigations by his student, Lorente di No, reduced that number to six (Amaral et al. 1987). After many subsequent years of disagreement, it is now broadly agreed that the EC is in fact a six-layered structure in rodents (Witter et al. 2017) and primates (Amaral et al. 1987; Van Hoesen & Pandya 1975a,b). However, as we discuss in Sections 3 and 4, the promiscuous connectivity of layers I–V has been the most intriguing to researchers studying the functional role of EC. The proportionate layer sizes and constituent cell densities change across the various subdivisions of the primate EC; however, the cell morphologies (or lack thereof) that constitute each layer remain consistent. Layer I is devoid of cell bodies and contains axially directed axons. Layer II is comprised of cells that are morphologically modified pyramidal cells, typically referred to as stellate cells. Layer III is the canonical pyramidal cell layer often found in the cortex, and, like layer II, it changes in thickness and density across the various EC subregions. Layer IV is similar to layer I in that it is devoid of cell bodies; accordingly, this area is typically labeled the lamina dissecans. Like layer I, layer IV is a fiber-heavy zone. Layer V, another thick pyramidal cell layer similar to layer III, contains a density gradient of its constituent cells such that they are most densely packed superficially. Because of this cell density gradient, this layer is often subdivided into sublaminae Va, Vb, and Vc. Layer VI—perhaps the least-studied portion of the EC—houses variously sized neurons in bands of differing density. In contrast to the rest of the EC, the sub-bands of this layer are interesting in that they take a much more curved shape compared to those of other layers (Amaral et al. 1987).

2.2.3 ENTORHINAL SUBREGIONS

The canonical subdivision of the rodent EC into MEC and LEC has its basis in several facets of anatomy and physiology. The cytoarchitecture of the LEC is consistent with the majority of the cortex and has smooth, continuous cell layers, which is a stark contrast from the patchy, interrupted cell layers seen in the MEC (Witter et al. 2017). In addition, differing patterns of connectivity (Witter 2007) and unique neurophysiological responses to behavioral phenomena serve to distinguish these subregions (Deshmukh & Knierim 2011; Fyhn et al. 2004; Hafting et al. 2005; Sargolini et al. 2006; Solstad et al. 2008; Tsao et al. 2013, 2018). Our ability to subdivide the primate EC has also been steeped in a history of contradictions (Amaral et al. 1987). In Brodmann's initial dissections of the EC of various species, he opted not to subdivide the EC of primates despite delineating medial and lateral aspects in the brains of bats, hedgehogs, and other nonprimate species (Brodmann & Garey 2006). Subsequently, others have divided the primate EC into as many as 14 subareas in monkeys and 23 in humans based on cytoarchitectonics alone (Amaral et al. 1987). Just as the disagreements over gross cytoarchitecture were resolved, a subtle agreement has been reached within the field over how to sub-divide the primate EC since the era of these initial studies. In rhesus monkeys, pivotal work by Van Hoesen & Pandya (1975a,b) highlighted three predominant subfields—a caudal, an intermediate, and a rostral area. One of the main findings to support this separation was the changing cytoarchitecture between the caudal EC and the more rostral EC elements. Specifically, in the rostral area, layer IV is virtually nonexistent, and the stellate cells in layer II form small, discontiguous clusters of islands. In the intermediate zone, the layer II islets become more prominent and consistent, moving caudally in conjunction with layer IV becoming increasingly visible. Finally, layer II is a continuous band of cells, and the cell-less layer IV is significantly more prominent in the caudal area. These findings were largely corroborated by Amaral and colleagues (1987) in cynomologus macaques; however, Amaral and colleagues also observed strong departures from the rhesus brain that led them to identify seven distinct EC subregions (Figure 1b). The most rostral element, the olfactory EC (EO), is the only subregion delineated by its unique inputs. As its name suggests, this region receives strong, direct terminations from the olfactory bulb. Just behind the EO lies the region labeled the rostral EC (ER). The ER bears many similarities with the rostral area in the rhesus. However, it lacks the cell-less layer IV and contains patchy islets of cells in its superficial layers. The intermediate EC (EI) sits directly behind the ER and serves as the transitionary bound between the interrupted cell islands in the more anterior portions of the EC and the continuous layers in more posterior elements. Lateral to both ER and EI, the portion of EC that runs along the medial edge of the rhinal sulcus is cytoarchitectonically distinct from its more medial subregions. Because of changing cytoarchitecture even along its rostro-caudal extent, this lateral element of EC has been divided into two distinct areas. The rostral portion (ELR) sits lateral to ER, and the caudal element (ELC) lies lateral to EI. Layers II and III house thick islands of cells in both regions, with the ELC containing more dense clusters. The cell-less layer I increases in size in the ELR relative to the ELC, although there is no visible layer IV in either area. Interestingly, a rhesus homolog of these regions was identified by Van Hoesen & Pandya (1975a,b), and it was named prorhinal cortex. Yet Amaral et al. (1987) opted not to label this an independent brain area because its projection patterns were similar to other subregions within the EC of cynomologous macaques. The caudal EC is divided into two fields, EC and ECL. The EC sits directly behind the EI and the caudal-limiting field (ECL) behind the EC. In both regions, the islands of layer II cells become thicker and more robust as one moves caudally, such that, in the most posterior elements of the EC and all of the ECL, the layer looks like a uniform band of neurons (Amaral et al. 1987).

2.3 NONHIPPOCAMPAL ENTORHINAL CONNECTIVITY

2.3.1. SUBCORTICAL CONNECTIVITY

The EC receives substantial input from subcortical areas, including the amygdala, claustrum, striatum, basal forebrain, and others (Insausti et al. 1987b). Interestingly enough, with rare exceptions, there is no strong evidence of topographic bias of subcortical projections onto the EC. Additionally, subcortical sites appear to project only ipsilaterally to the EC, as opposed to bilaterally (Insausti et al. 1987b). However, the diversity of these diffuse subcortical inputs, combined with the immense topography of cortical termination patterns onto the EC (see Section 3.2), amplifies the high degree of specialized information that this structure can convey to the downstream hippocampus. The number of subcortical sites that project to the EC is tremendous; in this section, we highlight a few key areas that specifically communicate with the primate EC in the service of learning and memory. In the rodent, the medial septal nucleus (MS) and diagonal band of Broca (DBB), components of the basal forebrain, are considered to be among the most critical cholinergic and GABAergic inputs into both the EC and hippocampus because of their strong influence on the rhythmic mesoscopic properties of neuronal activity in these regions (Carpenter et al. 2017, Dragoi et al. 1999, Mitchell et al. 1982). In the monkey, there exists strong projections between the MS/DBB and the EC. However, in contrast to findings in rodents suggesting a strong topography of connectivity (Kondo & Zaborszky 2016), the primate MS/DBB efferents to the EC appear to be considerably more diffuse across the structure (Insausti et al. 1987b). In addition, strong cholinergic projections (Liu et al. 2015) from the nucleus basalis of Meynert terminate onto the primate EC (Amaral & Cowan 1980, Insausti et al. 1987b, Mesulam et al. 1983). Projections from this region are virtually nonexistent in the rodent (Kondo & Zaborszky 2016), suggesting that there is an additional excitatory drive into the EC that is primate-specific. This largely unexplored interaction between the nucleus basalis and EC in primates may explain some of the observed differences in the neurophysiology of this region across species (see Section 5.3). Surprisingly, the largest subcortical projections to the EC come not from the basal forebrain nuclei, but rather by way of the amygdala, which has been implicated in numerous behavioral phenomena including fear conditioning, reward processing, and memory-associated processes (Blair et al. 2001, Chudasama et al. 2009, LaLumiere 2014). Most of the projections from the amygdala to the EC originate in the lateral nucleus of the amygdala, with sparser projections arising from the accessory basal nucleus and periamygdaloid complex (Aggleton 1986, Insausti et al. 1987b). In contrast to other subcortical termination patterns, these projections are biased toward rostral elements of the EC (Insausti et al. 1987b), with the heaviest subregions innervated by the amygdala being the Eo, Er, and ELR. In these regions, anterograde tracing experiments highlighted robust amygdala terminations specifically in layers I, III, and V, whereas amygdalar input is restricted to layer I in more intermediate and caudal EC regions (Insausti et al. 1987b).

With respect to inputs from diencephalic structures, the primate EC receives considerable input from both the thalamus and hypothalamus (Amaral & Cowan 1980, Insausti et al. 1987b). Thalamic input to the EC is dominated mostly by the central lateral nucleus, which has been indicated by rodent studies to be responsive to noxious, visceral stimulation (Ren et al. 2009). Retrograde tracing also suggests noticeable terminations in EC after injections made in the paraventricular, parataenial, and pulvinar nuclei (Amaral & Cowan 1980, Insausti et al. 1987b). Although efferents from the nucleus reuniens are also present in primate EC, the density of these projections appear to be sparser than those in rodents (Dolleman-Van Der Weel & Witter 1996, Insausti et al. 1987b). Several nuclei within the hypothalamus also project to the EC. Of these, the most prominent projection comes from the supramammilary area (Amaral & Cowan 1980, Insausti et al. 1987b). This is another region that contributes to rhythmic synchrony in the neurophysiology of the rodent EC, both through its direct influences on the structure and through interactions with the MS/DBB (Vertes & Kocsis 1997). Its promiscuous connectivity in the primate EC suggests an analogous synchronizing function with the hippocampal formation of primates. Several neuromodulatory systems in the brainstem also innervate the EC. Considerable projections from the dorsal raphe nucleus and ventral tegmental area (VTA) have been observed through retrograde tracing (Insausti et al. 1987b). In the most anterior EC subregion, EO, additional retrograde labeling can be seen in the substantia nigra and parabrachial nucleus, among others, suggesting a unique interaction of reward-related and visceral brainstem areas with the most rostral element of the EC.

2.3.2 SENSORY AFFERENTS

The EC serves as the main sensory relay into the hippocampus (Figure 2a), and the strongest of these sensory projections is sent directly from the olfactory bulb to the most rostral element of the EC, EO (Carmichael et al. 1994, Insausti et al. 1987a). As mentioned above, this is the only entorhinal subregion defined on the basis of its cortical inputs, and no other unimodal sensory area has been shown to project directly to the EC in primates. The piriform cortex, which acts as the first cortical relay for the olfactory bulb, sends modest projections to both ER and ELR and a much sparser projection to EI. Retrograde tracing studies have definitively shown that neither auditory cortices nor high-level visual cortices such as area TE in the inferior temporal cortex project to any entorhinal subfield (Insausti et al. 1987a).

As may be expected, the majority of sensory input into the primate EC comes from polymodal association cortices (Figure 2a). Two of the heaviest projections into EC come from perirhinal cortex (area 35/36) and parahippocampal cortex (TF/TH) (Insausti et al. 1987a, Van Hoesen & Pandya 1975b). While these areas have been implicated in the processing of somatosensory and auditory stimuli, they receive predominantly visual input (Baxter et al. 1999, Fritz et al. 2005, Ramos 2014). The perirhinal cortex has been associated with the processing of complex visual objects (Buffalo et al. 1999, 2000; Gaffan & Murray 1992; Murray & Mishkin 1998), and, in the parahippocampal cortex, this culmination of sensory processing is geared toward spatial information processing (Aguirre et al. 1996). It has long been accepted that in rodents, homologous regions project to distinct parts of the EC and form discrete functional domains by way of parahippocampal–MEC and perirhinal–LEC interactions (Burwell & Amaral 1998). However, this dogma has been recently challenged by Doan and colleagues (2019). Through a combination of tract tracing and in-vitro physiology experiments, Doan et al. (2019) identified a heavy bias of both perirhinal and parahippocampal input towards LEC, with only minimal projections from parahippocampal cortex to a limited portion of MEC. These recent findings parallel the diffuse perirhinal and parahippocampal projection patterns to the EC of primates. Anterograde and retrograde tracing experiments have shown that both the perirhinal and parahippocampal cortices project to all subregions of the EC apart from the most rostral EO and the lateral elements ELR and ELC (Insausti et al. 1987a, Insausti & Amaral 2008, Suzuki & Amaral 1994) (see Figure 2b for retrograde injection placements). Perirhinal cortex projects more strongly to rostral elements of the EC, with only sparse terminations on caudo-lateral EC. In tandem, the parahippocampal cortices are biased toward more caudo-central portions, with only minor projections to rostro-lateral EC (Insausti & Amaral 2008, Suzuki & Amaral 1994) (Figure 2a). Interestingly, a restricted portion of posterior parahippocampal cortex originates projections to the most caudo-medial portion of EC, akin to what has been observed in rodents (Doan et al. 2019, Suzuki & Amaral 1997, Insausti & Amaral, 1987a). Thus, the input patterns of the rodent and primate ECs with their respective perirhinal and parahippocampal cortices are consistent in that polymodal information converges onto lateral portions of the EC in both species.

The dorsal polymodal areas of the superior temporal gyrus also send projections to the EC, and tracing studies implicate a bias toward more caudal aspects (Insausti & Amaral 2008, Insausti et al. 1987a) (Figure 2a). Similar to the collective functions of the perirhinal and parahippocampal cortices, these inputs from the superior temporal sulcus provide an additional avenue by which the caudal EC receives highly processed visual information for object recognition and biological motion processing (Chaplin et al. 2018, Desimone & Ungerleider 1986). The rostral EC receives unique polysensory input from the insula, and anterior portions of this region (the agranular insula) innervate the anterior EC subregions ER, ELR, and anterior EI (Insausti & Amaral 2008, Insausti et al. 1987a). These inputs have been reported to carry audio-visual information, although the insula has been implicated in widespread sensory and cognitive functioning (Evrard 2019). For all sensory areas, the strongest sites of laminar termination were located in layers I–III (Insausti & Amaral 2008) (Figure 1c). Thus, with the exception of the olfactory area Eo, the data suggest that all areas of the EC receive largely visually modulated information about putative objects and relevant motion information from neocortical sites.

2.3.3 FRONTAL AND CINGULATE AFFERENTS

The frontal and cingulate cortices also send extensive projections to the primate EC (Figure 2a). One of the largest inputs from the frontal cortices in primates to the EC originates in the orbitofrontal cortex (OFC; area 13/13a) (Insausti & Amaral 2008, Insausti et al. 1987a, Rempel-Clower 2000, Van Hoesen & Pandya 1975b Witter et al. 1989). These inputs preferentially innervate the rostro-lateral elements of the EC but synapse on all subregions with the exception of ECL. These projections have been shown in retrograde tracing experiments to most strongly emanate from caudal elements of areas 13/13a. Sparser projections have also been observed from more rostral orbitofrontal areas 11 and 12, ventromedial area 14, and dorsolateral frontal cortices (Insausti & Amaral 2008, Insausti et al. 1987a). Anterior cingulate areas 32, 24, and 25 project strongly to ER and ELR, with minor projections to more caudal aspects of EC. The retrosplenial cortex (areas 29 & 30) constitutes the major projection from the posterior cingulate. This region provides robust input to the more caudal elements of the EC, such as the posterior EI, EC, and ECL (Insausti & Amaral 2008, Insausti et al. 1987a). The projections from these frontal and cingulate areas are similar to inputs from sensory areas (Section 3.2) in that they terminate preferentially onto layers I–III, although in the case of the retrosplenial cortex and some of the caudo-medial portions of the OFC, the laminar distribution of projections included deep layers V and VI (Insausti & Amaral 2008, Rempel-Clower 2000). The OFC and anterior cingulate cortices have long been associated with reward-based learning and complex contextual learning, respectively (Setogawa et al. 2019, Walton & Mars 2007). In contrast, the retrosplenial cortex has been shown to be critical in maintaining allocentric heading during navigatory behaviors (Chen et al. 1993, Clark et al. 2010). The parcellation of these functionally unique inputs onto distinct rostro-caudal sites suggests an additional route of information specialization within the various subregions of the primate EC.

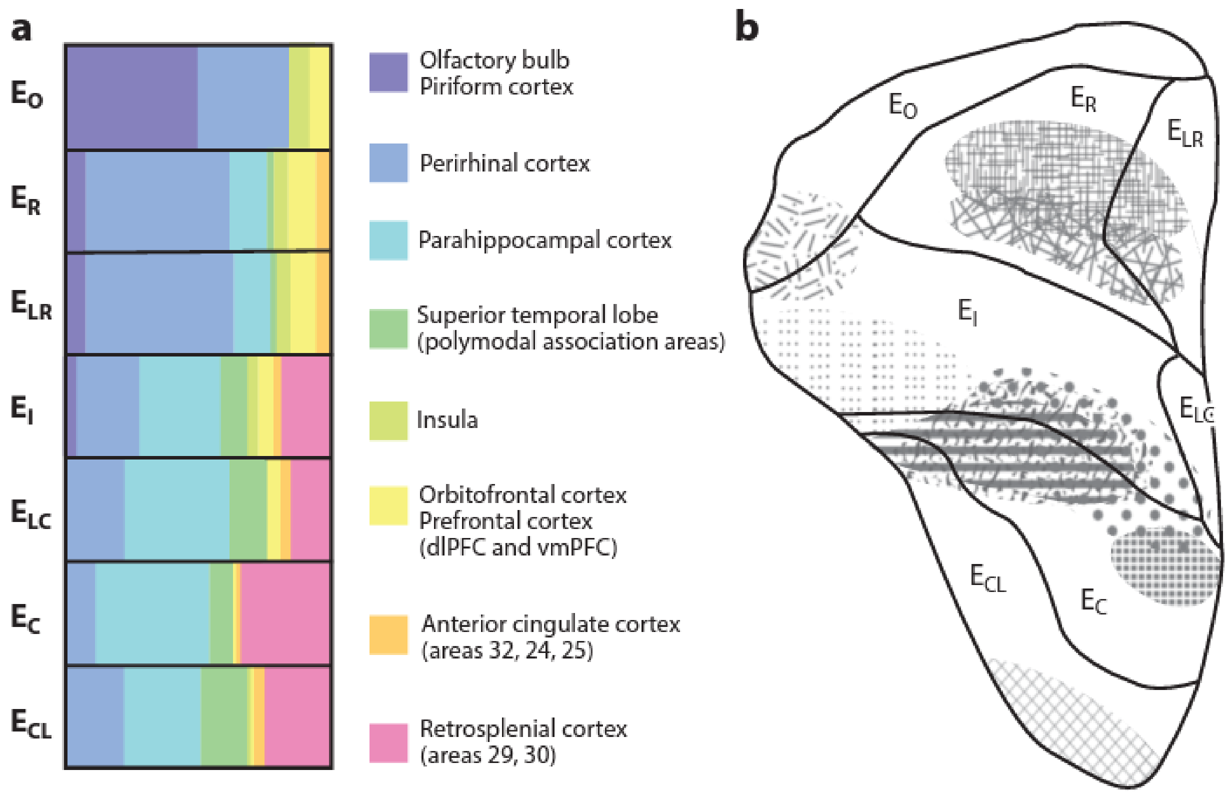

Figure 2.2 Summary of the major sensory and cortical afferents to the primate entorhinal cortex

(A) The general topography of respective cortical termination patterns (EO: Olfactory EC, ER: Rostral EC, EI: Intermediate EC, ELR: Rostro-lateral EC, ELC: Rostro-caudal EC, EC: Caudal EC, ECL: Caudo-limiting EC). Data adapted with permission from Insausti et al. (1987a). (B) Flattened map of EC showing the placement of retrograde tracer injections that contribute to panel a. Image adapted with permission from Insausti et al. (1987a).

2.4 ENTORHINAL CONNECTIVITY WITHIN THE HIPPOCAMPAL FORMATION

As mentioned above, the EC is the main source of cortical input to the hippocampus. In all species, the perforant pathway provides the strongest connection between these two regions (Witter et al. 1989). In macaque brains, layers II and III of the EC comprise the majority of perforant path projections, with deeper layers V and VI providing only sparse efferents (Van Hoesen 1975a, Witter & Amaral 1991, Witter et al. 1989). Layers II and VI communicate specifically to the DG and CA3, whereas layers III and V projections are more biased toward CA1 and the subiculum (Witter & Amaral 1991). In turn, feedback from CA1 and the subiculum in the hippocampus terminates predominantly onto the deep layers V and VI, with very sparse projections onto layer III (Witter & Amaral 1991) (Figure 1c).

The various connections between the hippocampus and EC are not homogenously distributed and actually span three distinct topographies. In the first, cells located laterally in layers II and III of the EC project to more caudal aspects of the hippocampus, while more medially situated cells terminate rostrally (Witter & Amaral 1991, Witter et al. 1989). Two distinct topographies have also been identified along the rostral-caudal axis of the EC. Efferent projections to the DG and CA3, which arise largely from layer II, are oriented such that rostral connections from the EC synapse onto more superficial aspects of the dendrites of the principal cells within each area. Specifically, rostral projections terminate onto the dendrites of granule cells in superficial aspects of the molecular layer of the DG, whereas more caudal efferents terminate deeper in the molecular layer. Additionally, rostral projections terminate onto pyramidal cell dendrites more distally in the strata lacunosum moleculare within CA3 in comparison to the more proximal terminations by caudal efferents (Van Hoesen & Pandya 1975a, Witter & Amaral 1991). Projections to CA1 from layer III of the EC also have a rostro-caudal termination pattern, such that rostral efferents target distal CA1 near its border with CA3 and the proximal subiculum, with increasingly caudal projections synapsing onto more proximal CA1 and the distal subiculum (Suzuki & Amaral 1994). In contrast, the recurrent projections from the hippocampus to the deep layers of the EC appear more homogenous in their distribution (Witter & Amaral 1991).

Alongside its myriad projections to the hippocampus, the diverse intrinsic connectivity of the EC adds an additional level of complexity when interpreting the role of this structure within the hippocampal formation. As in rodents, the EC of primates can be distinguished as having at least three discrete bands of interconnectivity (Chrobak & Amaral 2007). Rostro-medial layer V and VI neurons synapse onto caudo-medial layer II and III cells (and vice versa for caudal-medial layer V and VI cells), and similar recurrent projection patterns are observed for intermediate and lateral aspects of the EC. However, unlike in rodents, the bands do not span the entire length of the primate EC. Instead, they are limited to between one-third to one-half the length of the EC (approximately 3–5 mm), with rostral bands being shorter and less dense than more caudal elements (Chrobak & Amaral 2007). Interestingly, the deep-to-superficial orientation of intrinsic EC connectivity has been identified to be largely excitatory and asymmetric, with 56% of the projections from layer V and VI being glutamatergic and synapsing onto stellate and pyramidal cells, respectively (Chrobak & Amaral 2007). The remaining 44% synapse onto the dendritic shafts of putative interneurons, however, suggesting parallel mechanisms of gain modulation between deep and superficial layers of the EC. Only 5% of total identified projections in superficial layers were identified as recurrent in the monkey EC. Additionally, layer II cells of the lateral EC (ELC and ELR) send projections to layer II of all other subregions of the structure (Chrobak & Amaral 2007).

2.5 FUNCTION OF THE ENTORHINAL CORTEX

2.5.1 FUNCTIONAL IMPLICATIONS FROM ANATOMY

Considering the diversity of cortical input to the EC, of EC projections to the hippocampus, and within the intrinsic connectivity of EC, it is reasonable to assume that there are distinct processing domains within the EC that enable it to send unique information to the downstream hippocampus. For example, given the topography of projections from the perirhinal and parahippocampal cortices to the EC (see Section 3.2), we might expect that the rostral and caudal portions of this structure are somewhat biased towards information processing of objects and space, respectively (Insausti & Amaral 2008, Insausti et al. 1987a). The caudo-medial portion of EC that receives projections from parahippocampal cortex, but not perirhinal cortex, seems uniquely specialized for spatial processing, and this is where spatial representations have been observed in electrophysiological recordings from our lab (see Section 5.3). In contrast, the convergence of information on lateral portions of the EC suggests that neurons in this region have the capacity to encode highly conjunctive and complex information. Additionally, in contrast to the rodent EC, the intrinsic circuitry across different rostro-caudal elements of the monkey EC is discontinuous throughout the length of the structure (Chrobak & Amaral 2007). This suggests more distinct functional specialization within the primate EC by virtue of the fact that there is virtually no feedback from portions of the EC that receive different cortical inputs.

Similar functional hypotheses can be posited from frontal connectivity with the primate EC. Both the OFC and retrosplenial cortex project to the EC. The OFC is strongly implicated in value-based decision making (Setogawa et al. 2019), whereas the retrosplenial cortex is more associated with allocentric navigation (Chen et al. 1993, Clark et al. 2010). With respect to EC connectivity, as described in Section 3.3, the OFC synapses primarily onto rostral elements of the EC, and the retrosplenial cortex terminates onto caudal sites. Again, because of limited feedback between different sections along the EC's rostro-caudal extent (Chrobak & Amaral 2007), this anatomical evidence suggests domains in the primate EC that are functionally distinct by virtue of their different frontal influences. Because of the difficulty in accurately targeting putative EC subareas, it has been difficult to test many of these hypothesized functional distinctions. As electrophysiological recordings and elegant manipulation paradigms continue to evolve, it will be important to assess how the diverse connectivity into and within the EC facilitates the specificity of the information that it sends to the hippocampus in the service of learning and memory.

2.5.2 LESION RESULTS

Over the past two decades, lesion studies have directly examined the role of the EC in various visually guided memory-dependent behaviors. The most ubiquitous of these paradigms are the delayed match-to-sample (DMS) task and its nonmatch variant, in which subjects are rewarded for choosing a stimulus that either matches or is distinct from an initially viewed sample after a delay period. Monkeys are remarkably skilled at performing these behaviors and achieve scores significantly above chance levels, even when the delays between the sample and choice phases are extended to beyond 10 min (Buckmaster et al. 2004, Leonard et al. 1995, Murray & Mishkin 1998, Zola et al. 2000). Interestingly, unlike the cases of recognition memory deficits observed in animals with lesions of the hippocampus alone (Nemanic et al. 2004, Pascalis & Bachevalier 1999, Zola et al. 2000) or lesions that include the perirhinal and parahippocampal cortices (Buffalo et al. 1999, 2000; Gaffan & Murray 1992; Meunier et al. 1993), animals with EC lesions show only transient impairment, with normal performance on tests of recognition memory observed after approximately 1 year post lesion. (Leonard et al. 1995). Leonard and colleagues (1995) showed through histological analyses that perirhinal cortex projections to CA1 become significantly more robust in animals with EC lesions; providing a potential mechanism by which plasticity can induce the observed behavioral recovery. Perirhinal involvement in object recognition observed through permanent lesions (Buffalo et al. 1999, 2000; Gaffan & Murray 1992; Meunier et al. 1993) has been corroborated by recent work using optogenetic techniques in which neurons in this region were manipulated to bias recognition of a series of objects (Tamura et al. 2017). These transient and highly local manipulations were effective in biasing animals' perception of novel objects as familiar and familiar objects as novel when neurons were activated or inhibited, respectively. Whether acute manipulations of the EC produce a deficit in object recognition remains to be tested.

Intriguingly, EC lesions produce deficits on tasks that require the flexible manipulation of learned associations (Buckmaster et al. 2004), suggesting a role for this structure in supporting the relational organization of memory. Buckmaster and colleagues (2004) examined both monkeys with EC lesions and intact monkeys in a series of memory-related paradigms that probed the animals' ability to form associational relationships between objects and flexibly access those relationships. The first of these was the paired-associates (PA) task, in which subjects are rewarded for choosing the correct object from two choices, based on a centrally located visual cue (Figure 3). The correct choice item can then serve as a sample for a proceeding pair of objects, one of which is again rewarded by association with the cue.

Monkeys with EC lesions were just as capable of learning these two premise pairs as unoperated controls, although they did take slightly longer to reach the established acquisition criterion. When presented with another pair of problems, the initial training in controls facilitated much more rapid acquisition. In stark contrast, monkeys with EC lesions were just as slow at learning the associations in these new problems as they were during initial training. Conducting the PA task with overlapping stimuli allowed for a critical inference test in which the sample from the first trial was presented with the choice stimuli from the second trial. Because these objects have never been shown together, the monkey must draw upon the overlapping relationships between the experienced objects to solve this inherently novel problem. During these probe trials, monkeys with EC lesions were incapable of linking the sample to the indirectly associated choice object. By contrast, control monkeys were able to use their previously acquired associations flexibly to correctly solve the probe trials. Similar results were observed in the transitive inference (TI) paradigm. In TI, overlapping pairs of objects form a transitively associated hierarchy (i.e., A > B > C > D > E). If the EC is critical for either creating the overall reward hierarchy or flexibly manipulating the relationships that constitute it, then monkeys with EC lesions should fail at an inference test where discontinuous objects in the hierarchy are presented together (i.e., B versus D). This is exactly what was observed in the study by Buckmaster et al. (2004). Although monkeys with EC lesions were not impaired at learning the initially presented pairs, they were incapable of successfully employing the learned associations between items to discriminate between nonadjacent items. By contrast, when presented with the first and last objects of the hierarchy (the only items consistently rewarded and not rewarded, respectively), monkeys with EC lesions performed normally, suggesting that they were able to leverage the consistent reward history of the objects to solve the problem. Similar findings have been observed in monkeys with combined lesions of the hippocampus and fornix, although the performance impairment observed in these animals might be explained by the unintended damage of subcortical EC projections running through the fornix (Saunders & Weiskrantz 1989). Given this apparent role of the EC in flexibly linking experiences with objects, one might wonder if this structure plays a role in associating objects with other physical features such as spatial location. Buckmaster and colleagues tested this potential function using a serial-delayed recognition span task, which rewarded monkeys for choosing one item from an identical set on a multisite board when that item was in a novel spatial location. Results showed that monkeys with EC lesions were incapable of holding even one spatial location in memory. Taken together, lesion studies suggest that, although the EC is not critical for remembering putative objects or even simple associations between experienced objects, it is necessary for employing existing relational frameworks between objects to navigate novel experiences.

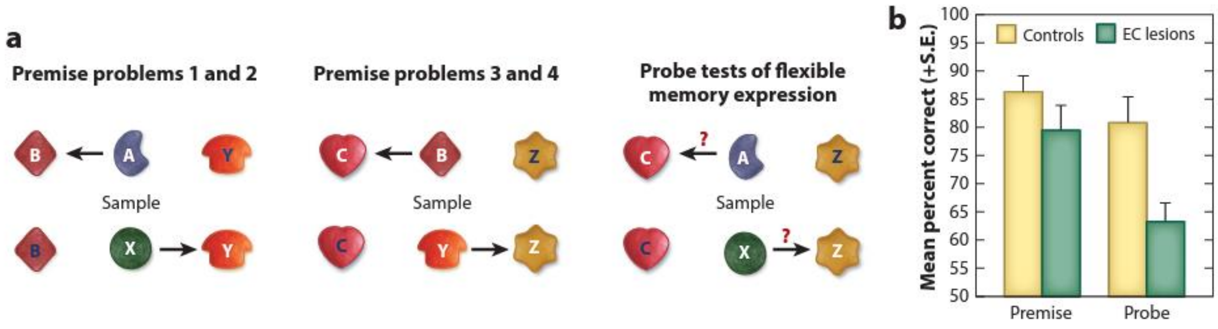

FIGURE 2.3 FLEXIBLE MEMORY DEPENDS ON THE ENTORHINAL CORTEX

(A) PAIRED ASSOCIATES (PA) TASK SCHEMATIC. MONKEYS ARE TRAINED TO SELECT ONE STIMULUS IN THE PRESENCE OF A CENTRALLY LOCATED CUE. IN THE FOLLOWING TRIAL, THE PREVIOUSLY CHOSEN STIMULUS BECOMES THE SAMPLE CUE FOR A NOVEL PAIR OF CHOICE STIMULI. THE CRITICAL INFERENCE TEST UTILIZES THE INITIALLY CUED STIMULUS WITH THE LATTER PAIR OF CHOICE STIMULI, AND ANIMALS ARE REWARDED FOR USING THE INDIRECT RELATIONSHIP BETWEEN OBJECTS TO INFER THE REWARDED ASSOCIATIONS. (B) PERFORMANCE SCORES FOR THE PA TASK SHOW THAT MONKEYS WITH ENTORHINAL CORTEX (EC) LESIONS (GREEN BARS) PERFORM JUST AS WELL AS UNOPERATED CONTROLS (YELLOW BARS) AT THE INITIAL PREMISE PAIR TRAINING. HOWEVER, MONKEYS WITH EC LESIONS ARE SIGNIFICANTLY IMPAIRED AT DISCERNING THE CORRECT PAIRED STIMULUS DURING INFERENCE PROBES. FIGURE ADAPTED WITH PERMISSION FROM BUCKMASTER ET AL. (2004).

2.5.3 PHYSIOLOGICAL FINDINGS

One of the neurophysiological hallmarks of the rodent hippocampal formation is high-amplitude, rhythmic neuronal activity that occurs in its constituent structures as animals actively explore an environment. This activity is typically present as a consistent, theta-band (6–12 Hz) oscillation in recorded local field potentials as animals translocate (Dragoi et al. 1999, Vanderwolf 1969), and it is strongly correlated with olfactory exploratory behaviors such as sniffing and whisking (Komisaruk 1970). By contrast, rhythmic activity in the theta band observed in the monkey hippocampal formation, including the EC, is not observed as a sustained oscillation, but instead occurs in interrupted bouts (Courellis et al. 2019; Hoffman et al. 2013; Jutras & Buffalo 2010, 2014; Jutras et al. 2013; Killian et al. 2012; Talakoub et al. 2019). These discontinuous bouts of theta are also observed in the hippocampus proper of humans (Aghajan et al. 2017, Bohbot et al. 2017, Lega et al. 2012) and in both the hippocampus and EC of bats (Eliav et al. 2015, Ulanovsky & Moss 2007, Yartsev & Ulanovsky 2013, Yartsev et al. 2011). Additionally, whereas non-REM sleep in rodents is characterized by a lack of sustained theta activity in MTL structures (Constantinou et al. 2016, Vanderwolf 1969), evidence suggests that structures within the hippocampal formation in primates, including the EC, paradoxically elicit stronger and longer bouts of theta-band activity during transitions from awake behavior to sleep (Talakoub et al. 2019). Future work will be critical to advance our understanding of the synchronized network states that organize neuronal activity in the primate hippocampus and EC.

In addition to research focused on the mesoscopic physiology of this region, analysis of the responses of EC neurons during memory-dependent paradigms has begun to elucidate the ways in which the distinct neurophysiology of the EC facilitates its function, as proposed by anatomical (Sections 3, 4, and 5.1) and lesion investigations (Section 5.2). The EC receives input from neurons in the most anterior portions of the ventral visual stream, which do not themselves respond to simple stimulus features (Miller et al. 1993). It is therefore not surprising that EC neurons do not show selective responses to particular features of object stimuli, such as color or contour (Suzuki et al. 1997). Instead, single-unit recordings in the EC have identified memory-related responses to visual stimuli. For example, EC neurons show stimulus-specific increases in firing rate in response to the presentation of the sample stimulus in a DMS task (Riches et al. 1991, Suzuki et al. 1997). If the EC were simply relaying object identity to the downstream hippocampus, then one would expect the firing rates of sample-selective neurons to be similar between repeated presentations of the same stimulus. However, during match trials, EC neurons demonstrated modulations in firing rates, showing both increases and decreases (Fahy et al. 1993, Riches et al. 1991, Suzuki et al. 1997) (Figure 4a–b), and these match enhancement and suppression effects on firing rate are observed before the animal makes its response during the test phase. Similar patterns of activity have been observed in the hippocampus (Jutras & Buffalo 2010), perirhinal cortex (Miller & Desimone 1994), and prefrontal cortex (Miller et al. 1996); these patterns suggest that the EC is potentially tuning its responses to facilitate memory-based decision making. Alternatively, given the dopaminergic inputs from the VTA mentioned in Section 3.1, stimulus novelty may drive the responses in this structure. In fact, when unique nonmatching stimuli are presented between the sample and matching test item, EC neurons elicit elevated firing (Suzuki et al. 1997). Interestingly, during interstimulus delays, EC neurons show sustained firing across numerous delay lengths, and in the majority of cases, these responses are sample selective, suggesting a possible influence of working memory on these neurons (Suzuki et al. 1997) (Figure 4c). These delay-sustained responses stand in contrast to responses of the upstream perirhinal cortex, in which any delay activity was eliminated upon presentation of intervening stimuli (Miller et al. 1993). Although lesion studies suggest only a transient role of the EC in simple object recognition (see Section 5.2), these memory-related neural responses may underlie the role of the EC in the flexible manipulation of learned associations (Buckmaster et al. 2004).

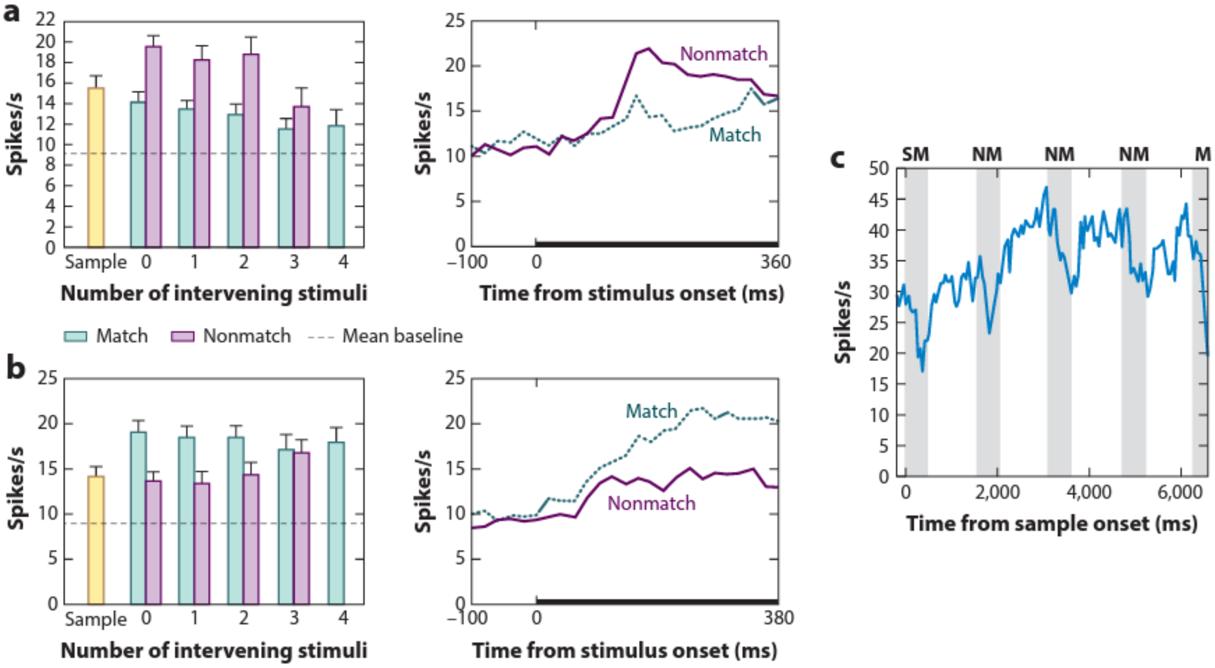

Figure 2.4 Memory-associated neurophysiological responses

(A) Average firing-rate histogram (left) and time course (right) of stimulus-selective cells in the monkey entorhinal cortex (EC) that show match suppression during delayed match-to-sample (DMS) with various intervening stimuli. (B) Average firing-rate histogram (left) and time course (right) of cells that exhibit match enhancement during DMS under the same conditions as in panel A. (C) Firing-rate histogram of an EC neuron with significant delay period activity. As memory load increases with intervening irrelevant stimuli, the firing rate of this neuron increases. Figure adapted with permission from Suzuki et al. (1997).

The most prominent neural response that has been identified in the rodent hippocampal formation relates to allocentric spatial representations (Fyhn et al. 2004, Hafting et al. 2005, O'Keefe & Dostrovsky 1971, Sargolini et al. 2006); one of the major hypotheses of the function of the hippocampal formation is that of a cognitive map that represents not just physical space but also relational object space (Buffalo 2015, Eichenbaum 2017, O'Keefe & Nadel 1978, Schiller et al. 2015). During a spatial task in which monkeys were rewarded for responding to a stimulus located in the same position as it was during a sample phase (delayed match-to-place), a proportion of EC neurons elicited biased responses for particular locations (Suzuki et al. 1997). Recent studies have also explored the extent to which EC neurons show place-specific firing relative to visual exploration. In rodents, exploration in physical space elicits a range of neuronal responses in the EC, including firing in symmetric, triangular patterns (grid cells) (Fyhn et al. 2004, Hafting et al. 2005, Sargolini et al. 2006); firing in relation to experienced physical boundaries (border cells) (Solstad et al. 2008); and firing relative to an animal's orientation within an environment (head-direction cells) (Sargolini et al. 2006). Work from our own lab in head-fixed animals viewing images on a computer screen shows that some cells in the primate EC elicit spatial responses based on locations of gaze, including grid-like firing fields and responses that are selective to fixations made at the borders of visual stimuli (Killian et al. 2012) (Figure 5a–c). In addition, and potentially analogous to rodent head-direction cells, a population of primate EC neurons were identified that were tuned to fire when the animal made saccades in a particular direction (Killian et al. 2015) (Figure 5d). Grid cells in the monkey EC display a gradient of grid field size and spacing such that both parameters increase in more medial recording sites. These findings are consistent with the gradient of changing grid field structure along the longitudinal extent of the EC that has been observed in both rodents (Hafting et al. 2005) and bats (Yartsev et al. 2011). In more recent work, a large proportion of nongrid but spatially responsive EC neurons have been identified during visual exploration (Meister & Buffalo 2018). The firing fields of these neurons are spatially reliable but more amorphous than those of grid cells. These findings are consistent with a recently described population of rodent EC cells (Diehl et al. 2017). Recordings in the monkey EC identified multiple frames of reference among the population of nongrid spatial cells (Meister & Buffalo 2018). When monkeys viewed an image that shifted to multiple positions on a screen, the firing patterns of one population of EC neurons remained the same relative to the image regardless of its position within the screen. In contrast, a second population of EC neurons elicited egocentric firing preferences. As images shifted on the screen, these neurons stably represented where on the screen the animal was looking, as opposed to boundaries established by the visual image. Finally, spatial responses in the monkey EC were also identified relative to the location of attention, even in the absence of any movement (Wilming et al. 2018). In this study, monkeys were trained to maintain fixation on a small cross presented at the center of the screen and covertly attend to a small dot moving in the periphery. Monkeys were rewarded for releasing a bar in response to a subtle luminance change in the dot. The luminance change was titrated to ensure that selective attention to the cue was required for successful performance. The responses of EC neurons were examined relative to the location of the monkey's attention on successful trials, and a significant proportion of EC neurons demonstrated grid-like responses. These findings, taken together with recent similar findings in humans (Julian et al. 2018, Nau et al. 2018a), suggest that primate EC neurons may have the ability to regularly tile experience, independent of specific sensory or environmental dimensions.

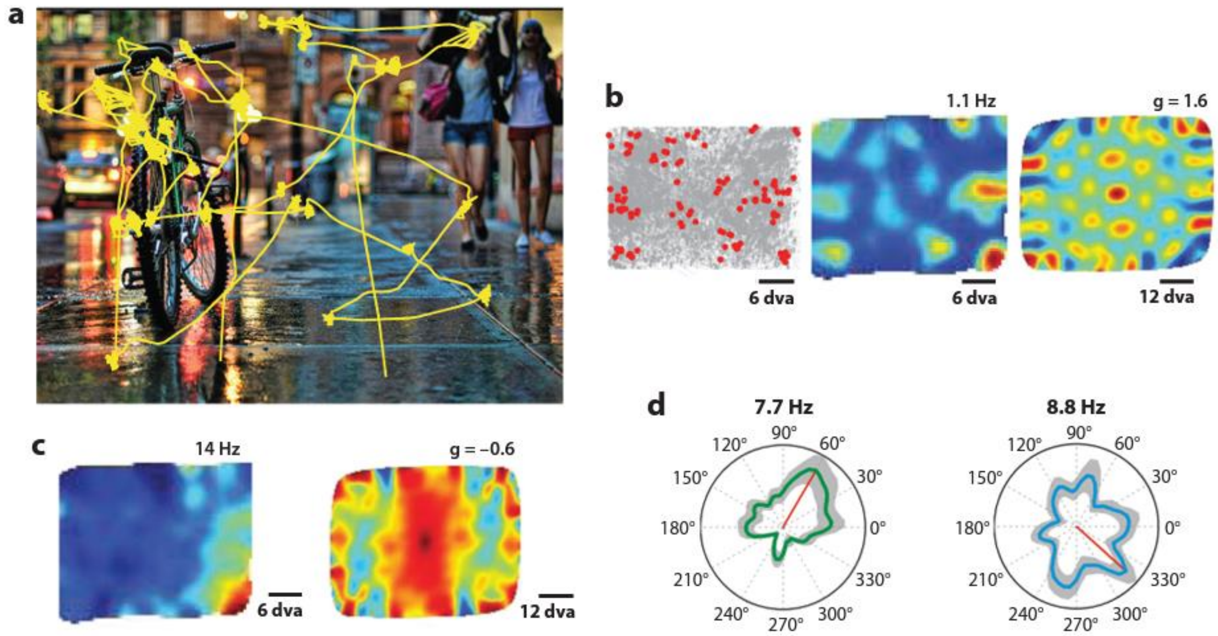

Figure 2.5 Spatial responses in the entorhinal cortex

(A) Example image presented on a computer screen during head-fixed visual exploration, with an example visual scan path overlaid (yellow trace). (B) Combined eye trace trajectories (gray traces), with spikes from a putative entorhinal cortex (EC) grid cell overlaid (red dots). Note the regular interval of spike clusters that is also apparent in the adjacent firing-rate map of this cell and best exemplified by the spatial autocorrelation map. (C) Firing-rate map (left) and autocorrelation map of a border cell isolated during the same visual exploration paradigm. Panel adapted with permission from Killian et al. (2012). (D) Example polar histograms of EC neurons that elicited strong firing rate modulations for saccades in a particular direction made immediately before (green trace) or after (blue trace) spikes were collected. Panel adapted with permission from Killian et al. (2015).

One might expect that, in addition to responding to particular places and things during an experienced event, a structure implicated in episodic memory would also process information about the temporal order of those experiences, and several forms of timing-related responses have been observed in the primate EC. When monkeys are rewarded for remembering the order of a list of individually presented objects, EC neurons demonstrate selective responses for objects in a particular position within the presented list (Naya & Suzuki 2011, Naya et al. 2017) (Figure 6a–b). In contrast to neurons recorded from the ventral prefrontal cortex (Naya et al. 2017), EC neurons also elicit conjunctive object-list position specificity. Recent work has demonstrated timing responses in the monkey EC as monkeys perform a free-viewing task (Bright et al. 2019). Many neurons in the EC responded to image onset, showing large changes relative to baseline shortly after image onset. Interestingly, these neurons showed a wide variety of rates with which they relaxed back to baseline, extending from hundreds of milliseconds to over 5 s (Figure 6c–d). Results from a linear discriminant analysis suggested that elapsed time could be decoded from the population, along with the identity of the presented image. Taken together, these neurophysiological investigations provide evidence that information about what, when, and where is represented within the monkey EC.

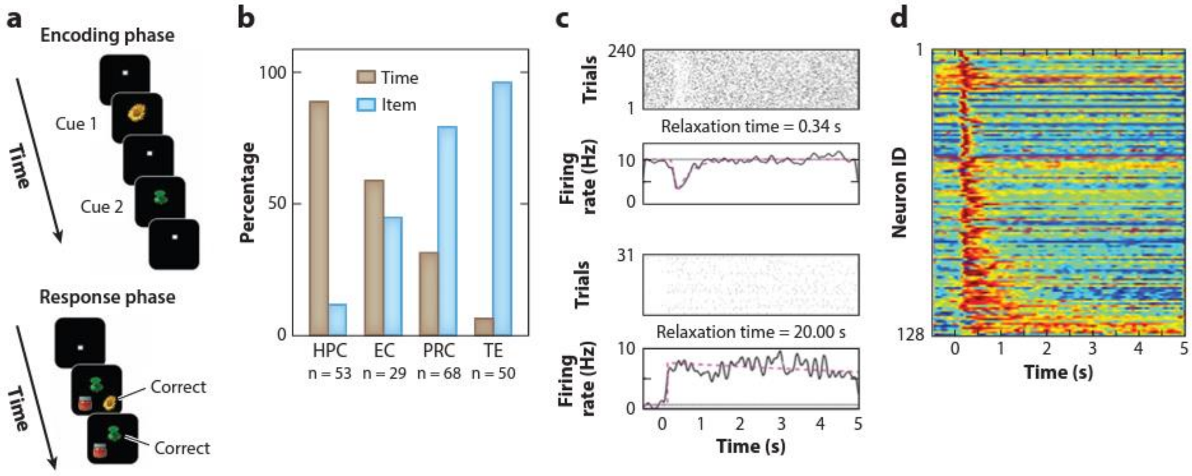

Figure 2.6 Temporal order & delay tracking responses in the entorhinal cortex

(A) Schematic of the temporal order memory task from Naya et al. (2011, 2017). Monkeys were shown two cues separated by brief delays (encoding phase). During the response phase, monkeys were rewarded for selecting the first, then second observed object from a cluster of simultaneously presented items. (B) Percentage of order- and item-specific cells isolated from various regions in the medial temporal lobe. Note that, in contrast to the strong temporal selectivity in hippocampal neurons and item selectivity in perirhinal cortex and inferior temporal lobe neurons, cells in the entorhinal cortex (EC) are heavily mixed in their temporal order and stimulus selectivities (HPC: Hippocampus, ERC: Entorhinal Cortex, PRC: Perirhinal Cortex, TE:Inferotemporal Cortex). Panel adapted with permission from Naya & Suzuki (2011). (C) Raster plots and firing-rate histograms of putative temporal context cells acquired during a visual exploration paradigm (see Figure 4a) that differentially modulate their firing rate relative to a prestimulus baseline with differing rates of relaxation. (D) Normalized firing rate map of 128 EC neurons sorted by their time of return to baseline firing rate. All recorded cells elicited little variance in their response latency to the presented image. However, their variance in relaxation time

OVER THE COURSE OF PRESENTATION SUGGESTS THE ABILITY OF EC NEURONS TO TRACK THE PASSAGE OF TIME AT DIFFERENT TIMESCALES. PANEL ADAPTED WITH PERMISSION FROM BRIGHT ET AL. (2019).

2.6 PARALLELS WITH THE HUMAN ENTORHINAL CORTEX

There is a growing body of evidence suggesting that the EC in humans closely mirrors what has been observed in nonhuman primates in both its anatomy and function. Although tracing experiments are not possible in humans, homologous subregions of the human EC were identified in functional connectivity experiments using functional magnetic resonance imaging (fMRI) (Maass et al. 2015, Schröder et al. 2015). Specifically, a strong blood oxygen level–dependent (BOLD) signal was observed in the rostro-lateral EC and caudo-medial EC that was coherent with the BOLD signal measured in the perirhinal and parahippocampal cortices, respectively. As described in Section 3.2, tracing studies in nonhuman primates also strongly imply topographic biases of projections from the perirhinal cortex to the rostro-lateral EC and from the parahippocampal cortex to the caudo-medial EC (Insausti & Amaral 2008, Suzuki & Amaral 1994). Unique functional connectivity between proximal and distal portions of the human subiculum with the rostro-lateral and caudo-medial EC was also observed, which is consistent with the patterns of projections observed through tracing experiments in nonhuman primates (Maass et al. 2016, Schröder et al. 2015, Suzuki & Amaral 1994).

The rostro-lateral and caudo-medial aspects of the human EC also exhibit behavioral selectivity in their respective BOLD activity preferences, with the rostro-lateral elements being more object responsive and the caudo-medial portions eliciting more spatially correlated BOLD responses (Schröder et al. 2015). While additional research is needed to confirm homologous functional specialization of EC subregions in nonhuman primates, these observed functional specializations in humans parallel the respective object and spatial specificity of the LEC and MEC in rodents (Deshmukh & Knierim 2011; Fyhn et al. 2004; Hafting et al. 2005; Sargolini et al. 2006; Solstad et al. 2008; Tsao et al. 2013, 2018). Deep brain stimulation of the human EC during virtual spatial navigation has shown a critical, albeit still not fully understood, influence of this structure in remembering previously visited locations (Jacobs et al. 2016, Suthana et al. 2012). As mentioned in Section 5.2, EC lesions in nonhuman primates produce profound deficits in spatial memory (Buckmaster et al. 2004). Neurophysiological recordings and imaging studies have also identified neural firing motifs within the human EC homologous to those observed in other species (see Section 5.3). Specifically, fMRI reveals macroscopic activity patterns with hexadirectionally selective, grid-like regularity in healthy subjects navigating a virtual reality open field maze (Doeller et al. 2010). Like rodent grid cells, these grid-like BOLD signals are anchored to allocentric cues, and certain signals were conjunctively modulated by the direction of virtual movement. These hexadirectionally modulated patterns are also present when subjects are tasked with imagining a route to a target stimulus (Horner et al. 2016), during visual scan behaviors (Nau et al. 2018b), and when subjects are required to conceptually organize information along two orthogonal discriminative axes (Constantinescu et al. 2016), suggesting a generalized coding scheme within the human EC for flexibly encoding and retrieving continuous information across behaviors. These imaging findings have been corroborated by single-unit recordings taken from human epileptic patients, in which EC neurons with grid-like firing fields (Jacobs et al. 2013) and those with direction-selective firing patterns (Jacobs et al. 2010) were identified during virtual reality navigation paradigms. Taken together, the growing body of converging evidence suggests that both the anatomical and functional features of the EC are largely conserved across species.

2.7 SUMMARY

The primate EC provides the majority of the cortical input to the hippocampus; however, data from lesion and neurophysiological studies suggest that the EC functions as much more than a simple information relay. The impairments observed following lesions restricted to the primate EC are distinct from those following hippocampal or perirhinal lesions, and the diverse neural activity observed among EC neurons is similarly distinct from that of its neighboring regions. In particular, the EC is only transiently necessary for simple object recognition but becomes critically important when the relationships between indirectly related objects must be inferred and when previously experienced locations must be remembered. Along with the object-related delay activity and timing responses that have been observed in the EC, these neurons also display robust and reliable spatial responses similar to the exquisite spatial representations identified in the rodent EC. Anatomically, the EC is a site of convergence of multiple cortical information streams, many with their own topographical projection patterns. Combined with the EC’s own limited intrinsic connectivity and topographically biased projections to different subregions within the hippocampus, this suggests that the EC is a computationally diverse area with elegant targeting of downstream structures. However, all of these anatomical findings come from only a handful of injections, and additional tracing studies should be performed to validate the complexity and subregional specificity of these different patterns of connectivity. Moreover, to date, the functions of these distinct processing streams have not been fully characterized. Novel technologies, including large-scale chronic recordings to densely sample neurons across EC subregions simultaneously with other brain regions, >1,000-site laminar probes to more thoroughly investigate network oscillations across laminae, and targeted modulation through cell-type-specific optogenetic manipulations, are becoming accessible in primate research. Such tools will be critical to advancing our understanding of the computations that the EC performs intrinsically and in concert with other memory-associated machinery within the hippocampal formation.

2.8 ACKNOWLEDGMENTS

We would like to thank Jon Rueckemann and Menno Witter for insightful discussions and edits of the manuscript.

CHAPTER 3 || IMPROVING THE EFFICACY AND ACCESSIBILITY OF INTRACRANIAL VIRAL VECTOR DELIVERY IN NON-HUMAN PRIMATES

Chapter adapted from published work: **Griggs DJ & Garcia AD**, Au WY, Ojemann WKS, Johnson AG, Ting JT, Buffalo EA, Yazdan-Shahmorad A. Improving the Efficacy and Accessibility of Intracranial Viral Vector Delivery in Non-Human Primates. Pharmaceutics. 2022 Jul 8;14(7):1435. doi: 10.3390/pharmaceutics14071435. PMID: 35890331; PMCID: PMC9323200.

3.1 INTRODUCTION

The development of novel tools to genetically alter the properties of neurons has been instrumental in expanding the scope of neuroscientific questions. Perhaps one of the most popular of these genetic modification methods is optogenetics, through which cells can be made susceptible to rapid, reversible manipulations via light stimulation. This technique was first demonstrated in 2005 [1] and since then has been robustly developed and widely adopted. In particular, optogenetics has become a powerful tool for rodent neuroscience [2,3]. The high-throughput nature of experiments with these models means that researchers can pilot, experiment, and make corrections with new subjects rapidly and with minimal resources. Additionally, the rapid gestational time (~1 month for most research species) and large litter size (4–12 pups/L) of these models extends the genetic modification toolkit of rodent researchers to allow for breeding genetically altered lines and testing transgenic subjects with relative ease. However, transgenic lines are largely unavailable for highly translational non-human primate (NHP) models. In contrast to rodents, the macaque has a gestational period of ~6 months and gives birth to singular offspring, which eliminates the practical viability of transgenic approaches. This leaves viral vector transfection as the primary method of preparing NHPs for experiments requiring genetic modification. However, this experimental approach still proves to be a challenging, and potentially costly, endeavor. Here, we present novel and updated methods that eliminate several of the main dissuading factors of transduction studies in NHPs.

Convection-enhanced delivery (CED) is an infusion technique that has been developed over the past few decades to deliver medicinal agents to the brain [4,5]. Classic neural infusion techniques rely on diffusion, which is based on a concentration gradient and therefore is heavily influenced by molecular weight [6]. Large molecules such as viral vectors are inefficiently spread by diffusion. By contrast, CED capitalizes on a pressure gradient for delivery, which is much less influenced by molecular weight and comes with a number of benefits over diffusion: 1. CED can be performed at higher delivery rates (on the order of 1 µL/min or higher), which speeds up delivery [7–9], 2. CED can distribute agent over greater volumes (hundreds of mm3) [8,9], 3. CED produces a roughly uniform concentration of agent throughout the distribution volume [6,7,10–14], and 4. as previously alluded, CED is effective at transporting large molecules, such as viral vectors, throughout regions of the brain [7,11–15].

Incentivized by these desirable properties, we have used CED in recent years to deliver optogenetic viral vectors into the brains of non-human primates for neuroscientific experiments [8,9,16,17]. To complement the technique, we utilized a method of realtime infusion validation with magnetic resonance imaging (MRI) technology using a gadolinium-based contrast agent co-infused with the optogenetic viral vector [18]. We previously validated the resulting optogenetic expression with epifluorescence imaging, electrophysiology, and histology [8,9]. However, we recognize that not all institutions have access to an MRI scanner in which live validation of an injection can be visualized. Thus, a separate set of CED experiments without live MRI guidance was performed using novel optogenetic viral vectors co-infused with a manganese-based contrast agent. This allowed us to confirm infusion success the following day with MRI. With these live and next-day in vivo MRI data collected across ten animals and three different brain regions, we were uniquely positioned to develop a model to assist in planning CED procedures in the brains of NHPs. This work is important to the field because not all researchers have access to MRI scanners for next-day imaging, and fewer still are equipped to perform NHP viral infusions in an MRI scanner. We propose a CED modeling method that can assist any researcher in NHP neurosurgical CED planning.

Here, we have developed a quantitative bench-side CED model that provides the users with hands-on CED experience. Our bench-side model builds on our recent qualitative infusion modeling work [19], as well as our in vivo NHP data [8,9]. Bench-side CED models usually comprise dye infused into agar phantom, a clear gel with material properties similar to the brain [20,21]. In this work, we propose a similar model, but to our knowledge, we are the first to base a bench-side model on in vivo MRI data of CED in NHP brains. We provide the MRI data and we present a calibration method for our model using the MRI data to ensure that the reproduction of our quantitative method is practical for the field. Infusions into the primate brain are inherently coupled with surgical and experimental risks; however, the toolkit presented here mitigates the risk factors of these procedures, such as cost, surgical time, and overall subject count, by providing easily accessible ways to plan CED experiments. We also utilize a radiolabel that can be co-infused with viruses that can be imaged in MRI 24 h post-operatively, which empowers researchers without immediate access to an MRI scanner to identify issues and make any necessary surgical corrections in a timely fashion.

3.2 MATERIALS AND METHODS

3.2.1 SUBJECTS

Data from ten macaques were used for this study, as described in Table 1. The cortical and thalamic data (total n = 5) come from previously published procedures [8,9,18,22,23], and those data have been used in the present study. In contrast, data from the medial temporal lobe (MTL) group are derived from new injection procedures, which are described in detail below. The ages ranged from 5 to 11 years, and weights ranged from 5.7 to 17.5 kg. Five females and four males were rhesus macaques (Macaca mulatta) and one male was a pigtail macaque (Macaca nemestrina). MTL subjects were provided by the tissue distribution program available from the Washington National Primate Center (WaNPRC), and no observable differences were seen in our data as a function of age, sex, species, or weight.

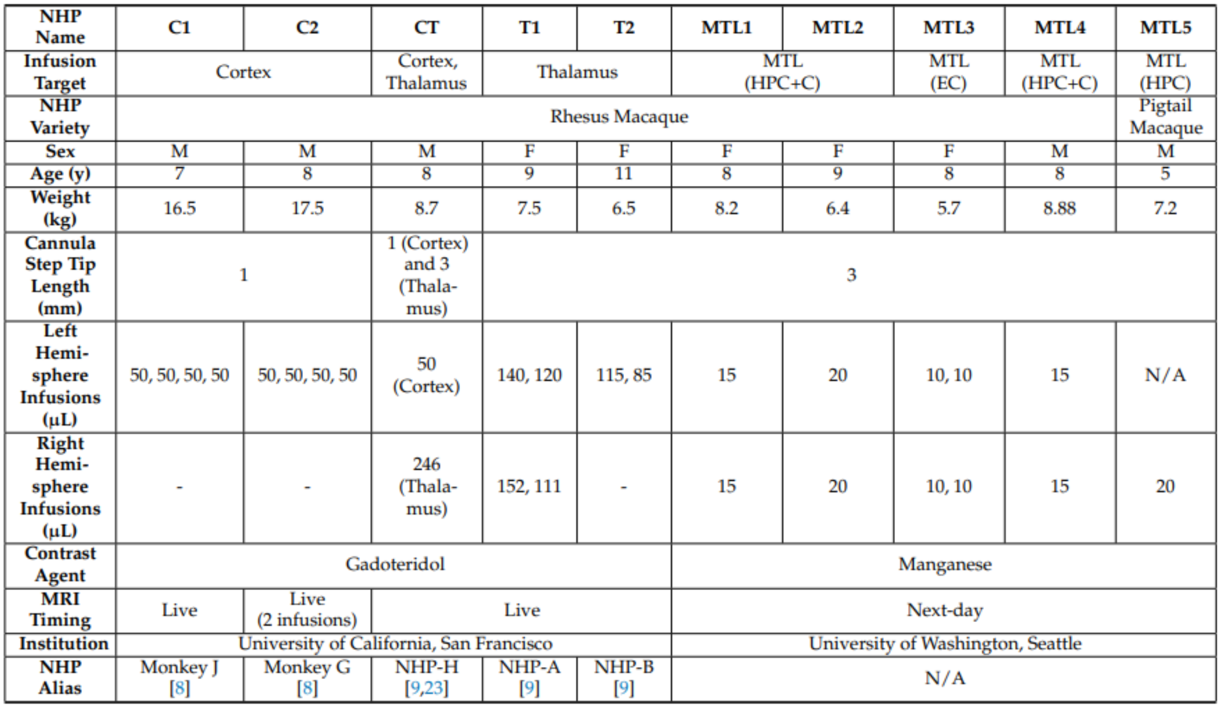

NHP Name	C1	C2	CT	T1	T2	MTL1	MTL2	MTL3	MTL4	MTL5
Infusion Target	Cortex		Cortex, Thalamus	Thalamus		MTL (HPC+C)		MTL (EC)	MTL (HPC+C)	MTL (HPC)
NHP Variety	Rhesus Macaque									Pigtail Macaque
Sex	M	M	M	F	F	F	F	F	M	M
Age (y)	7	8	8	9	11	8	9	8	8	5
Weight (kg)	16.5	17.5	8.7	7.5	6.5	8.2	6.4	5.7	8.88	7.2
Cannula Step Tip Length (mm)	1		1 (Cortex) and 3 (Thalamus)	3						
Left Hemisphere Infusions (µL)	50, 50, 50, 50	50, 50, 50, 50	50 (Cortex)	140, 120	115, 85	15	20	10, 10	15	N/A
Right Hemisphere Infusions (µL)	-	-	246 (Thalamus)	152, 111	-	15	20	10, 10	15	20
Contrast Agent	Gadoteridol					Manganese				
MRI Timing	Live	Live (2 infusions)	Live			Next-day				
Institution	University of California, San Francisco					University of Washington, Seattle				
NHP Alias	Monkey J [8]	Monkey G [8]	NHP-H [9,23]	NHP-A [9]	NHP-B [9]	N/A				

TABLE 3.1: NHP AND SURGICAL DATA

NHPS ARE NAMED FOR THEIR INFUSION LOCATION(S). MEDIAL TEMPORAL LOBE AND CAUDATE NUCLEUS (MTL). HIPPOCAMPUS (HPC). ENTORHINAL CORTEX (EC), TAIL OF CAUDATE NUCLEUS (C).

3.2.2 ANIMAL PROCEDURES AND MRI ANALYSES

Three different neuroanatomical structures were targeted for CED infusions: cortex, thalamus, and the medial temporal lobe together with the caudate nucleus (MTL). Most of the cortical and thalamic infusions were validated with live MRI, while MTL infusions were validated with MRI the day following infusion. Table 1 contains the infusion details for each subject.

Subsequent subsections describe the various methods and MRI analysis related to the cortical, thalamic, and MTL infusions. Because the procedures relating to the cortical and thalamic groups have been previously published, detailed surgical methods are omitted with references to the respective primary studies. However, aspects of the procedures germane to the present study are presented. For the MTL group, details of the surgical methods, euthanasia, and immunohistochemistry are presented in full. For all procedures, vital signs such as heart rate, respiration, and body temperature were monitored throughout.

3.2.2.1 Cortical Infusion

We have previously described the surgical methods for cortical CED procedures [8,18]. Briefly, the subjects were anesthetized under isoflurane, a craniotomy was made above the sensorimotor cortex in a sterile operating room, and an MR-compatible cannula guide was affixed to the skull with MR-compatible screws and dental acrylic. Afterwards, the subjects were transferred to an MR scanner (Siemens 3T) while remaining under isoflurane anesthesia. We inserted the tip of a stepped-tip cannula about 2 mm below the surface of the brain in the sensorimotor cortex. A syringe pump (WPI UMP3, MICRO2T SMARTouch SGE250TLL, Sarasota, FL, USA) was used to co-infuse a mixture of AAVCamKIIa-C1V1-EYFP (Table 2; 2.5 × 1012 virus molecules/milliliter (vm UPenn vector core) and a gadolinium-based contrast agent (Table 2; 2 mM Gd-DTPA, ratio of 250:1, Gadoteridol, Prohance, Bracco Diagnostic Inc., Princeton, NJ, USA) into the brain at a starting rate of 1 μL/min, which was increased every few minutes up to 5 μL/min. After the majority of the volume had been delivered, the rate was reduced in the same stair-step method to end with a rate of 1 μL/min. After infusion, we left the cannula in place for 10 min and then removed the cannula. This infusion process was repeated multiple times. During the infusion process, multiple MRI images were taken to track the progress of the infusions. We used fast (2 min) flash T1-weighted images (flip angle = 30◦ , repetition time/echo time = 3.05, matrix size = 128 × 128, slice thickness = 1 mm, 64 slices, Siemens 3T MR scanner). After recovery and optogenetic expression, Monkeys C1, C2, and CT were euthanized for immunohistochemical analysis of optogenetic expression [8,22,23].

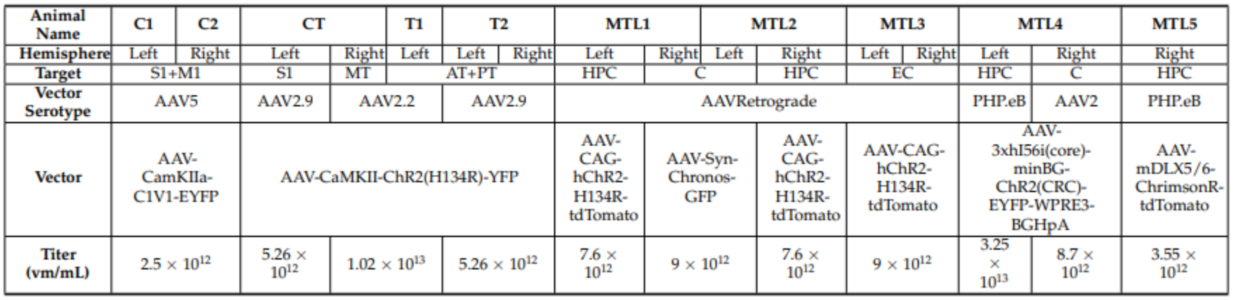

Animal Name	**C1**	**C2**	**CT**		**T1**	**T2**		**MTL1**		**MTL2**		**MTL3**		**MTL4**		**MTL5**
Hemisphere	Left	Right	Left	Right	Left	Left	Right	Left	Right	Left	Right	Left	Right	Left	Right	Right
Target	S1+M1		S1	MT	AT+PT			HPC	C		HPC	EC		HPC	C	HPC
Vector Serotype	AAV5		AAV2.9	AAV2.2		AAV2.9		AAVRetrograde						PHP.eB	AAV2	PHP.eB
Vector	AAV-CamKIIa-C1V1-EYFP		AAV-CaMKII-ChR2(H134R)-YFP					AAV-CAG-hChR2-H134R-tdTomato	AAV-Syn-Chronos-GFP		AAV-CAG-hChR2-H134R-tdTomato	AAV-CAG-hChR2-H134R-tdTomato		AAV-3xhI56i(core)-minBG-ChR2(CRC)-EYFP-WPRE3-BGHpA		AAV-mDLX5/6-ChrimsonR-tdTomato
Titer (vm/mL)	2.5×10^{12}		5.26×10^{12}	1.02×10^{13}		5.26×10^{12}		7.6×10^{12}	9×10^{12}		7.6×10^{12}	9×10^{12}		3.25×10^{13}	8.7×10^{12}	3.55×10^{12}

TABLE 3.2: VIRUS INFORMATION

S1 (PRIMARY SENSORIMOTOR CORTEX), M1 (PRIMARY MOTOR CORTEX), AT (ANTERIOR THALAMUS), MT (MEDIAL THALAMUS), PT (POSTERIOR THALAMUS), HPC (HIPPOCAMPUS), C (TAIL OF CAUDATE NUCLEUS), EC (ENTORHINAL CORTEX). VM/ML (VIRUS MOLECULES PER MILLILITER).

3.2.2.2 Thalamus Infusion

We previously described the surgical details of the thalamic CED infusions [9], which are similar to the cortical infusion procedures described above. Briefly, the subjects were anesthetized with isoflurane and craniotomies were made (15 mm diameter). We implanted cannula guides and secured them with plastic screws and dental acrylic. We allowed the subjects to recover for two weeks before performing CED. After recovery, the subjects were anesthetized, placed in a stereotax and transported to an MR scanner. We used the cannula guides to manually insert a 3 mm stepped-tip cannula (ClearPoint Neuro Inc. (formerly MRI Interventions, Solana Beach, CA, USA) to the targeted regions of the thalamus. We used a syringe pump (WPI UMP3, MICRO2T SMARTouch, SGE250TLL, Sarasota, FL, USA) to co-infuse multiple serotypes of AAV-CamKII-ChR2 (Table 2; Upenn vector core) with gadolinium-based contrast agent (Table 2; 2 mM Gadoteridol, Prohance, Bracco Diagnostic Inc., Princeton, NJ, USA) at rates between 0.5 μL/min and 3 μL/min while simultaneously performing fast (2 min) flash T1 MR scans (flip angle = 30◦ , repetition time/echo time = 3.05, matrix size = 128 × 128, slice thickness = 1 mm, 64 slices, Siemens 3T MR scanner). After all infusions were complete, the subjects were transported back to the surgical suite where the cannula guides were explanted and the incision closed. After recovery and optogenetic expression, Monkeys CT, T1, and T2 were euthanized for immunohistochemical analysis of optogenetic expression [9,23].

3.2.2.3 MTL Infusion

To pilot the efficacy of expression in the medial temporal lobe (MTL), five viral vectors were infused into the brains of five subjects. Subjects MTL1–3 were infused with two retrograde viruses (gifted from Edward Boyden and Karel Svoboda; Addgene viral preps #59170-AAVrg and #29017-AAVrg, respectively) [24,25]. Subjects MTL4 and 5 were infused with three GABA-selective viruses (Allen Institute for Brain Science and University of Washington, Seattle, WA.). See Table 2 for specific information about the vectors and target regions for all animals.

The surgical details of the MTL infusions are described in detail here. The animals were sedated with ketamine. A surgical plane was induced with propofol and maintained with 0.8–1.2% isoflurane, and the subjects were then stereotaxed. Analgesia was administered prior to (meloxicam) and during the procedure (fentanyl CRI transitioned to sustainedrelease buprenorphine). Sagittal incisions were made to expose the skull, and burr holes were drilled above our intended target. A 3 mm stepped-tip cannula (ClearPoint Neuro Inc. (formerly MRI Interventions, Solana Beach, CA, USA) was stereotactically lowered with a micro-manipulator arm through the burr hole to the targeted region of the MTL (hippocampus or entorhinal cortex), or the tail of the caudate nucleus. We used a syringe pump (WPI UMP3, MICRO2T SMARTouch, SGE250TLL, Sarasota, FL, USA) to co-infuse optogenetic viral vector with manganese-based contrast agent (Mn2+, Millipore Sigma, Burlington, MA) at rates between 1 µL/min and 5 µL/min. The final concentration of Mn2+ mixed with virus was 6.5 mM and was specifically chosen as it is well under the limit for neuronal toxicity and interference with viral efficacy, as identified by [26]. After all infusions were complete, the cannula was removed and the incision closed. In one case (MTL5), this procedure was performed using the Brainsight veterinary surgical robot (Rogue Research Inc., Montreal, QC, Canada) instead of micromanipulator arms. A final analgesic was administered in the form of a local anesthetic block (bupivacaine). The day following infusion, the subjects were again anesthetized and placed in an MR-compatible stereotax, and 3D MPRAGE sequences were taken in a 3T MRI scanner to localize the manganese signal (Scanner: Phillips GE, Boston, MA, slice thickness: 0.35 × 0.35 × 0.5 mm anisotropic and 0.5 isotropic voxels, repetition time/echo time = 2, flip angle: 9 degrees). After eight weeks, the animals were euthanized via intraperitoneal pentobarbital injection and transcardially perfused with 4% paraformaldehyde–phosphate buffer solution.

The harvested tissue was stored in sucrose and then sliced into 50 µm sections using a freezing microtome. The resulting slices were treated in a sodium borohydride bath (Millipore Sigma, Burlington, MA, USA) to reduce background fluorescence for 24 h. Afterward, the slices were incubated for 72 h at 4 ◦C in primary antibodies targeting the respective fluorescent tag of the infused virus (for case MTL4: rabbit-Anti-GFP 1:1000, Abcam #ab290). This was followed by two-hour incubation in fluorescent secondary antibodies (for case MTL4: donkey anti-rabbit 568 1:200, Invitrogen Molecular Probes #A10042) and DAPI stain (1:5000, ThermoFisher Scientific #D21490) before mounting and visualization.

3.2.2.4 MRI Volume Extraction

The following infusion volume extraction procedure was performed on the MRI scans. For cortical and thalamic trials, the MRIs were taken throughout the infusion period. For MTL infusions, the MRIs were taken the day after infusion. We imported each MRI scan into MRI viewing software (Mango, Research Imaging Institute, UTHSCSA, San Antonio, TX, USA) and identified the location of the infusion—due to the contrast agent, this area had a higher contrast than the surrounding tissue. A spherical region of interest (ROI) was created and adjusted as necessary to encompass the infused volume. We shrink-wrapped the ROI in 3D with a threshold value below the intensity of the infusion location, but above the intensity of the surrounding tissue. The threshold for the ROI was adjusted until it only contained the infusion volume and the final ROI was saved in the NIFTI file format. Next, we reloaded each ROI as its own image and generated an interpolated surface of the infusion volume. Finally, we measured the volume of the bolus using this interpolated surface in the MRI viewing software. In the case of live imaging during infusions, we mapped the infusion trajectories by applying this protocol to successive MRI scans within an infusion trial.

3.2.3 BENCH-SIDE MODELING

We developed a bench-side CED infusion technique using agar and custom-built cannulas. We also developed an image processing technique and statistical methods to analyze the agar data.

3.2.3.1 Cannula Production for Agar Infusions

We manufactured 1 mm and 3 mm stepped-tip cannulas (Supplementary Figure S1) with polyimide-coated fused silica capillary tubing (Polymicro Technologies, Phoenix, AZ, USA) for the cortical and deep infusions, respectively. These cannulas were created by sliding the smaller tubing into the larger tubing until the smaller tubing extended out of the larger tubing by 1 mm or 3 mm. This placement was then secured with cyanoacrylate (Super Glue Corporation, liquid super glue, Ontario, CA, USA). For both cannulas, the inner tubing had an inner diameter of 320 µm and an outer diameter of 435 µm (part #1068150204) and the outer tubing had an inner diameter of 450 µm and an outer diameter of 673 µm (part #1068150625). The cannulas were the same as, or similar to, the cannulas used for our NHP CED experiments above.

3.2.3.2 Agar Phantom Infusion

We prepared a solution of 1× phosphate-buffered saline (PBS) and 0.6% powder mixture, where the powder mixture comprised agar powder (Benchmark Scientific, A1700, Sayreville, NJ, USA) and locust bean gum powder (Modernist Pantry LLC, Eliot, ME, USA) in a 4:1 ratio by mass, respectively. We heated and mixed the solution in a microwave to dissolve the powder and poured it into molds to set. Setting occurred in a refrigerator for at least two hours. The molds were 3D printed with polylactic acid (PLA) filament and were designed to produce agar blocks with a 2 × 2 cm base and either 2 or 4 cm high. The agar phantoms were used shortly after setting or were refrigerated for up to one day for future use.

To prepare for CED infusion, we mounted a pump (WPI UMP3, MICRO2T SMARTouch, Sarasota, FL, USA) to a stereotactic arm (KOPF, 1460, Tujunga, CA, USA) attached to a stereotactic frame (KOPF, 1430, Tujunga, CA, USA). We filled the pump's 250 mL syringe (WPI, SGE250TLL, Sarasota, FL, USA) with deionized (DI) water and attached it to the pump. The cannula was attached to the syringe with a catheter connector (B. Braun Medical Inc., part #332283, Bethlehem, PA, USA). All of the DI water was ejected from the syringe to fill the cannula with DI water. Undiluted yellow food coloring (McCormick yellow food coloring, Hunt Valley, MD, USA) was then drawn through the cannula and into the syringe. We positioned the agar phantom under the cannula so that it was centered. The agar phantom was oriented such that the side of the block that was not in contact with the mold during the molding process (i.e., the top side, which was the smoothest side of the phantom) was facing up and would be the side to receive the cannula insertion. The cannula was then lowered until the tip touched the surface of the agar phantom. We lowered the cannula manually with the stereotactic arm to a pre-specified depth, 2 mm deep for cortical infusions and 2 cm deep for thalamic and MTL infusions. We checked that the surface of the agar sealed around the cannula above the stepped-tip before proceeding with the infusion.

To image the infusion process, we positioned a digital single-lens reflex (DSLR) camera (Nikon D5300, Minato City, Tokyo, Japan) with a 35 mm lens (Nikon, AF-S NIKKOR 1:1.8G) and adjusted the camera settings to clearly image the agar phantom edges, needle, and bolus. The ISO was set at 400, the shutter speed at 1/125, and the aperture at f/6.3. We used interval time shooting. We arranged a white backdrop to help with image processing and placed a ruler near the agar phantom and in-plane with the cannula for scale. We prepared a script in MATLAB (MathWorks Inc., Natick, MA, USA) to run the pump autonomously and in accordance with the infusion rates used in corresponding surgical infusions (Table 3). We started the script and the camera's time interval shooting simultaneously. Representative cortical and thalamic infusion models are compared with MRI data as shown in Figures 1 and 2, respectively. Refinements to infusion techniques during preliminary trials included optimizing lighting conditions, and camera angle and placement with respect to the agar phantom.

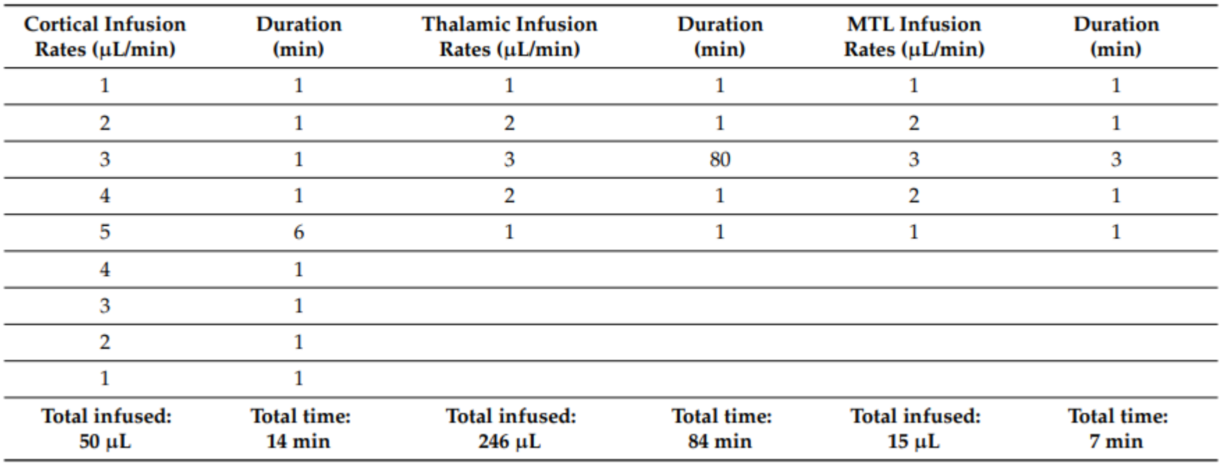

Cortical Infusion Rates (µL/min)	Duration (min)	Thalamic Infusion Rates (µL/min)	Duration (min)	MTL Infusion Rates (µL/min)	Duration (min)
1	1	1	1	1	1
2	1	2	1	2	1
3	1	3	80	3	3
4	1	2	1	2	1
5	6	1	1	1	1
4	1				
3	1				
2	1				
1	1				
Total infused: 50 µL	**Total time: 14 min**	**Total infused: 246 µL**	**Total time: 84 min**	**Total infused: 15 µL**	**Total time: 7 min**

TABLE 3.3: GEL INFUSION RATES

MEDIAL TEMPORAL LOBE (MTL).

2.3.3. AGAR PHANTOM IMAGE PROCESSING

We estimated volumes of distribution from photographs of the agar phantom infusion. A single-color component was selected from the color images. (Further description of the color component selection process is found below in Section 2.3.4.) Then, we applied a threshold value to the remaining matrix to produce a mask, being a matrix of binary values. (Specific methods for selecting this threshold value are found below in Section 2.3.5.) We manually selected the cluster of binary values representative of the infusion bolus and erased the other clusters from the mask. In some cases, this was enough to isolate the bolus, but in other cases, the mask appeared to depict the cannula together with the bolus. In these cases, the cannula was erased by masking all pixels above a manually selected point in the image such that the mask outlined the bolus alone. Representative images of the agar phantom image processing are shown in Figure 3. Finally, we converted the mask of the bolus to a volume by assuming an ellipsoidal form, where the ellipsoid was radially symmetric about the axis of the cannula. Similar to [27,28], we took the height (h) and width (w) of the bolus and calculated the volume (v) of the associated ellipsoid with the equation:

$$v = \left(\frac{\pi}{6}\right) * h * w^2 \qquad \textbf{(eq. 2.1)}$$

The volume estimation was converted to metric units based on the ruler in the original image. We performed all agar image processing with MATLAB.

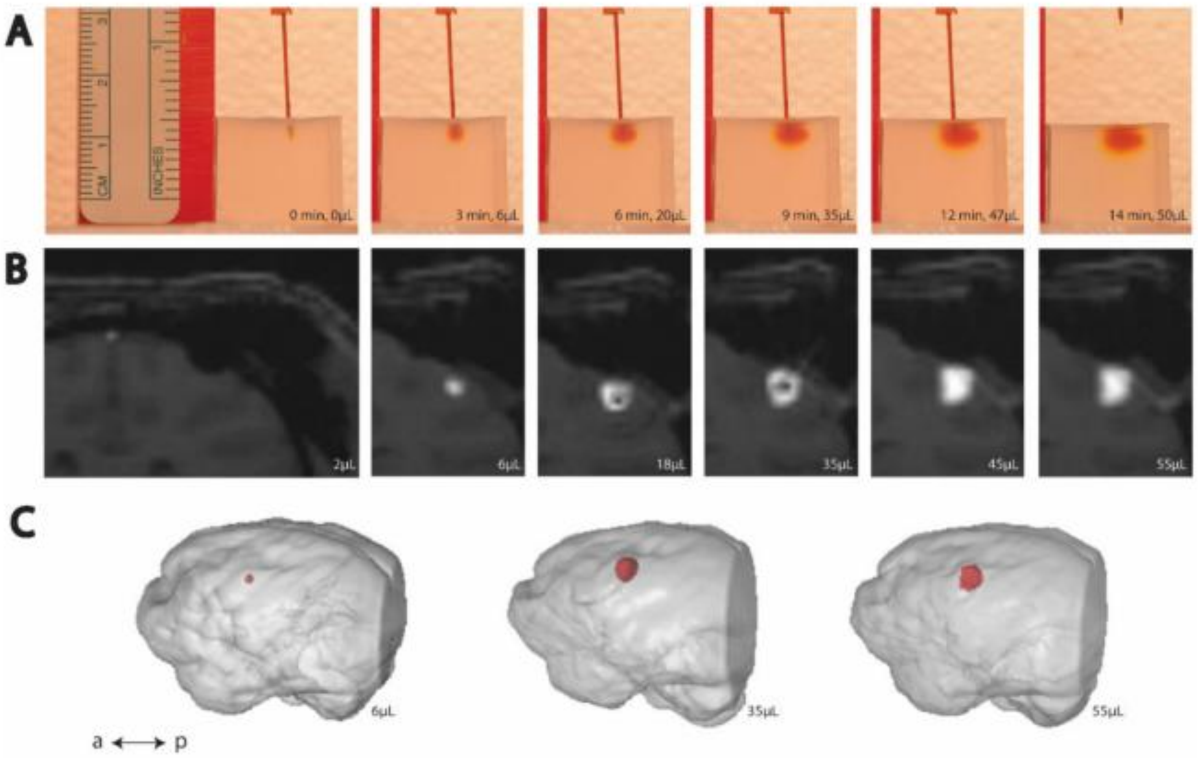

Figure 3.1: Time-lapse (left to right) of cortical CED

(A) Example trial of CED in agar phantom. (B) Example MRI visualization of CED in an NHP. (C) Post hoc reconstruction of NHP brain (gray) and infusion volume (red).

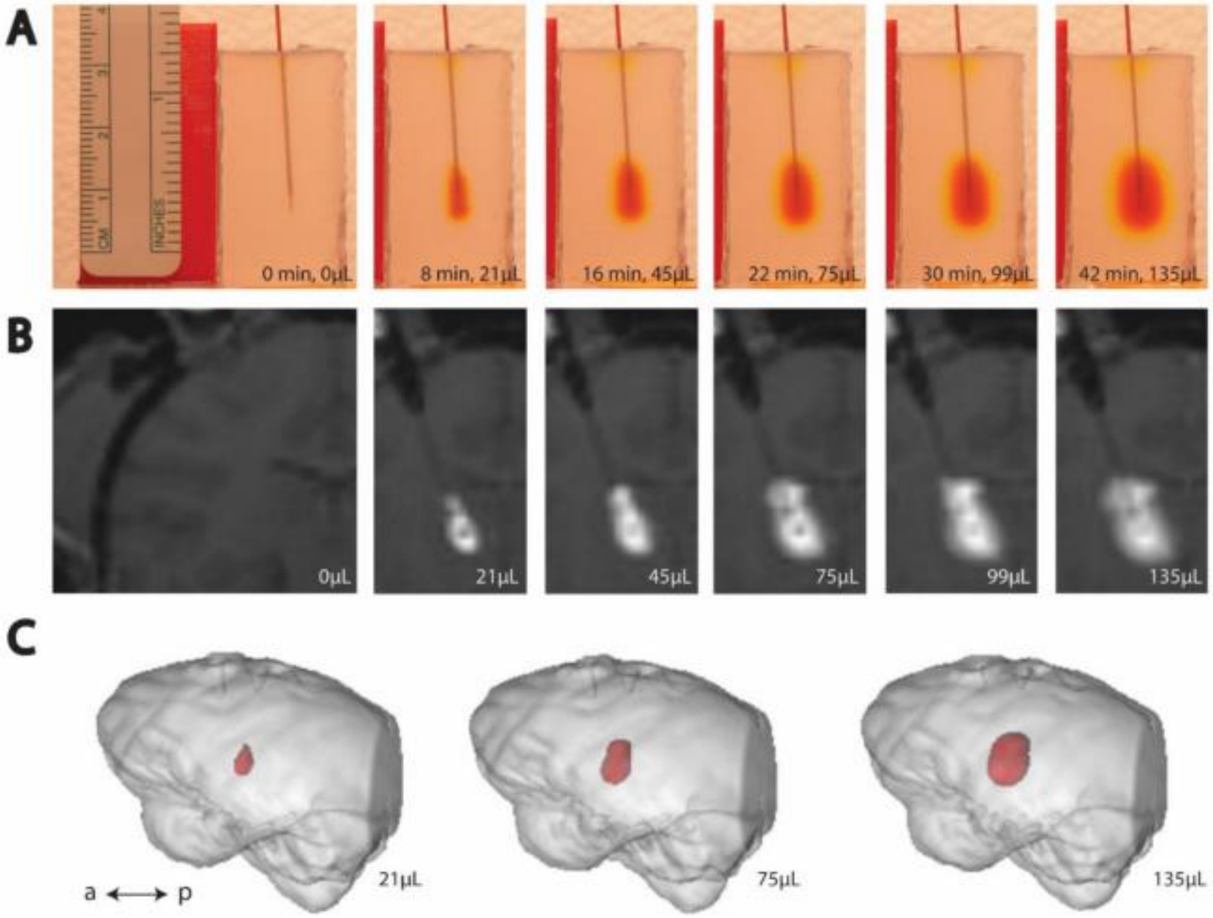

FIGURE 3.2: TIME-LAPSE (LEFT TO RIGHT) OF THALAMIC CED

(A) EXAMPLE TRIAL OF CED IN AGAR PHANTOM. (B) EXAMPLE MRI VISUALIZATION OF CED IN AN NHP. (C) POST HOC RECONSTRUCTION OF NHP BRAIN (GRAY) AND INFUSION VOLUME (RED).

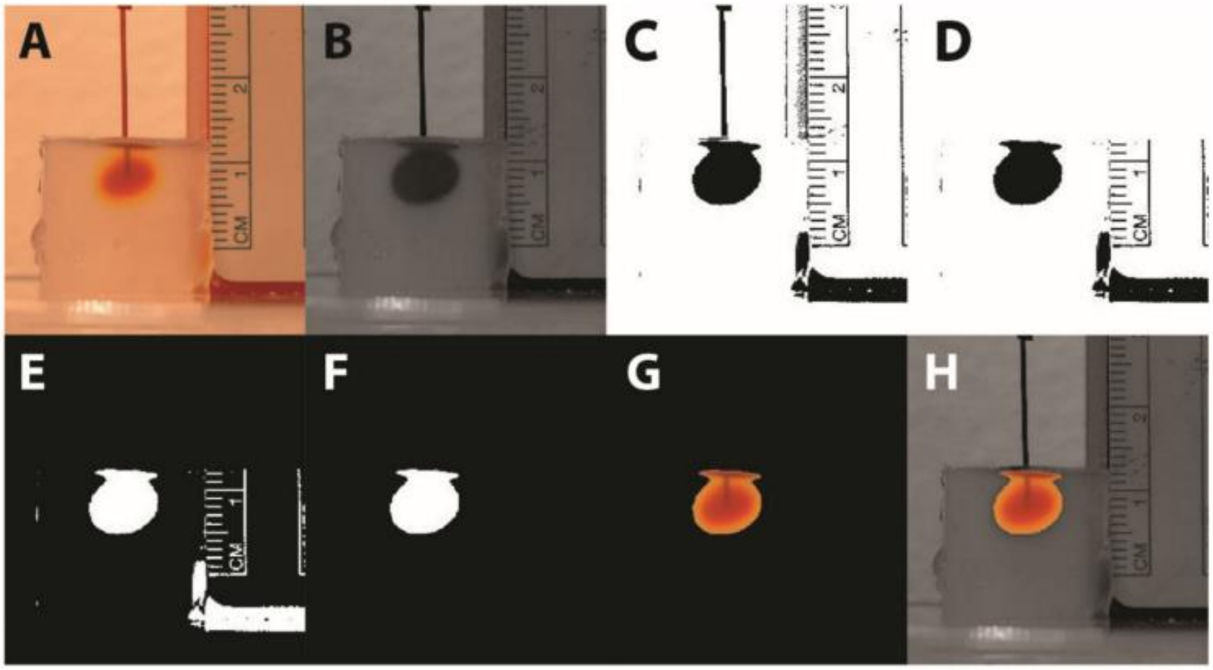

Figure 3.3 Image processing algorithm

(A) Original color image. (B) Single-color component image. (C) Thresholded image. (D) Cannula erasure. (E) Binary inversion. (F) Deletion of all non-bolus pixels. This is the final image used for volume calculation. (G) Color image of bolus overlaid on final image for user reference. (H) Color image of bolus overlaid on the single-color component image for user reference.

3.2.3.4 Color Component Selection

Our color component selection is the process by which a 24-bit RGB color image is converted to an image with one 8-bit value per pixel. We tested the three different color components to determine which aligned the agar data most closely with the MRI data. All data of the same infusion type were processed with one selected color component. While image processing software often have functions built in that will reduce images to a single value per pixel (e.g., the “rgb2gray” function in MATLAB), we found our color component selection process to be more effective.

3.2.3.5 Threshold Value Selection

After the color component selection, we used a threshold value to distinguish which pixels had strong enough values to be included as part of the bolus. To select the threshold value, we identified a region of the image where heavy coloration faded to no coloration, and then we selected a pixel from this region and used its value as the initial threshold. We performed the entire image processing procedure with this threshold value and plotted the agar data together with the MRI data to observe the quality of alignment. Based on the results, we selected a new threshold and repeated as necessary in an iterative fashion until the MRI data and the agar data were in alignment. Once aligned qualitatively, we compared the NHP volume data quantitatively with the agar volume data by using linear regression to determine the slope of each agar and NHP trial, as described in more detail in Section 2.3.6. All data of the same infusion type were processed with one selected threshold value.

3.2.3.6 Statistical Methods

To compare the agar and NHP data for the cortical and thalamic trials, we required a quantitative method that would take into account correlations between data points within a given trial, and also compare the different groups of trials. Additionally, we required a method that would not assume a fixed slope between the volume infused by the syringe and the measured bolus volume. To this end, we used a linear mixed-effects model with random slopes to fit each infusion trial, both in agar and in NHP data. All best-fit lines were restricted to passing through the origin (i.e., zero input volume and zero output volume). From this model, we calculated the interaction effect, which is an approximation of the difference in the average slope between the agar and NHP data. All linear mixed-effect model calculations were performed with MATLAB’s built-in “fitlme” function.

All other statistical calculations were performed in MATLAB except the average and percent error values of Table 4, which were performed in Excel (Microsoft Corp., Redmond, WA, USA).

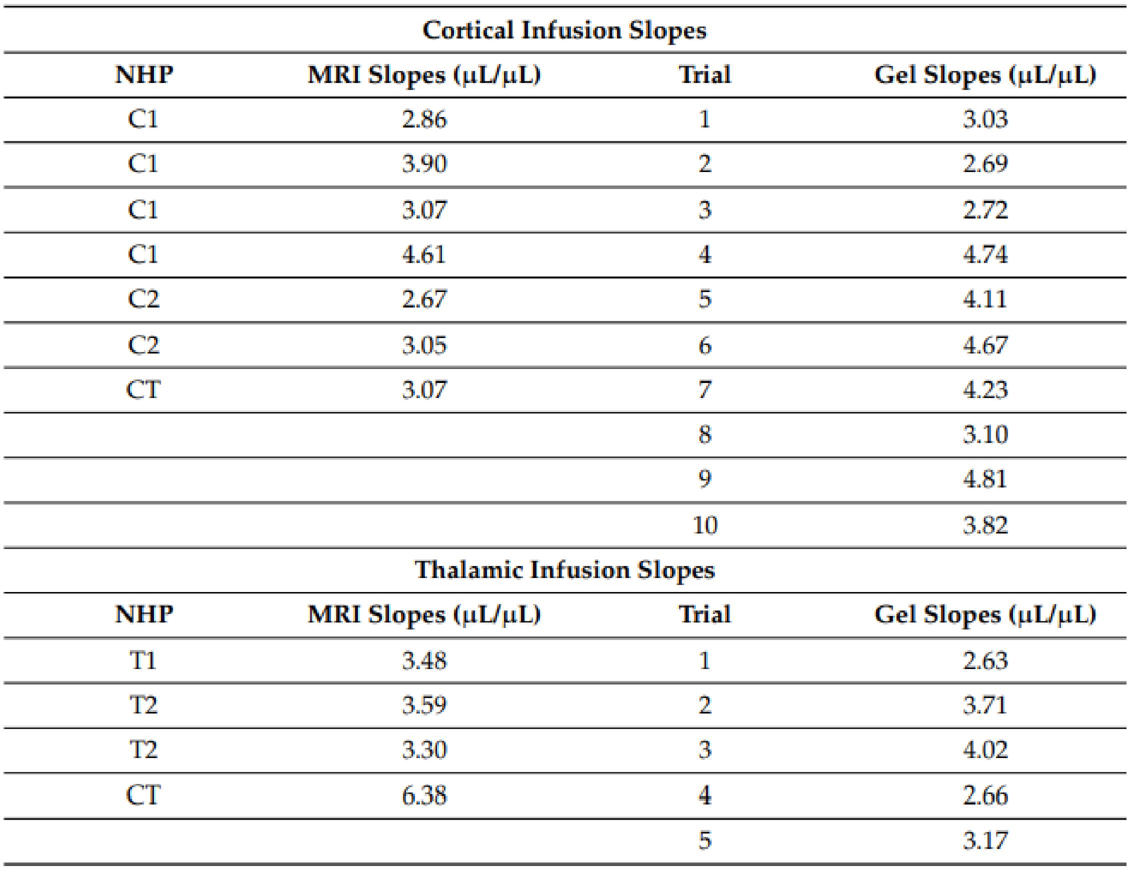

Cortical Infusion Slopes

NHP	MRI Slopes (μL/μL)	Trial	Gel Slopes (μL/μL)
C1	2.86	1	3.03
C1	3.90	2	2.69
C1	3.07	3	2.72
C1	4.61	4	4.74
C2	2.67	5	4.11
C2	3.05	6	4.67
CT	3.07	7	4.23
		8	3.10
		9	4.81
		10	3.82

Thalamic Infusion Slopes

NHP	MRI Slopes (μL/μL)	Trial	Gel Slopes (μL/μL)
T1	3.48	1	2.63
T2	3.59	2	3.71
T2	3.30	3	4.02
CT	6.38	4	2.66
		5	3.17

TABLE 3.4: CORTICAL AND THALAMIC DATA

3.3 RESULTS

Some agar infusion trials were unsuccessful, and these failed trials were omitted from statistical analyses and reattempted. Failed trials may have been produced by reasons such as dye leaking out through the catheter adapter or damaged agar phantoms.

3.3.1 CORTICAL AND THALAMIC INFUSIONS

We iteratively selected color components and threshold values to align the agar data with our previously published cortical [8] and thalamic [9] NHP data (Figures 4 and 5, respectively). The green component and threshold value of 110 (43% of green component intensity range) were best for the thalamic infusions, and the blue component and threshold value of 67 (26% of blue component intensity range) were best for the cortical infusions. When comparing the cortical agar data to the thalamic agar data, we observed that the agar and NHP best-fit slopes were similar (Figures 4 and 5). The cortical NHP data had slopes ranging from 2.9–4.6 µL/µL, and the cortical agar data had a range of 2.7–4.8 µL/µL. Meanwhile, the thalamic NHP data had a range of 3.5–6.4 µL/µL and the thalamic agar data had a range of 2.6–4.4 µL/µL (Table 4). There is significant variation in the slopes of the best-fit lines of the agar infusion data; however, this variation reflects the variation in the NHP data (Figures 4B and 5B).

We observed that a reduction of flow rate at the end of the cortical agar trials led to greater increase in bolus volume with respect to infused volume, i.e., the plots steepen near the end of the infusion protocol (Supplementary Figure S2). This is not characteristic of NHP cortical data, so we omitted the agar cortical data from 44 µL to 50 µL from statistical analysis and Figure 4 because it was not characteristic of NHP cortical data. Further descriptions may be found in the discussion (Section 4.4).

For the cortical and thalamic trials, we used a linear mixed-effects model with random slopes to fit each infusion trial, both in agar and in NHPs. This model produces an interaction effect of 1.1 and −0.5 for the cortical and thalamic infusions, respectively. These values are close to zero in comparison with the aforementioned ranges of the slopes, and these values have magnitudes less than the slope ranges, indicating that the agar and NHP data differ only mildly and that our agar phantom is a good representation of the NHP data for cortical and thalamic infusions.

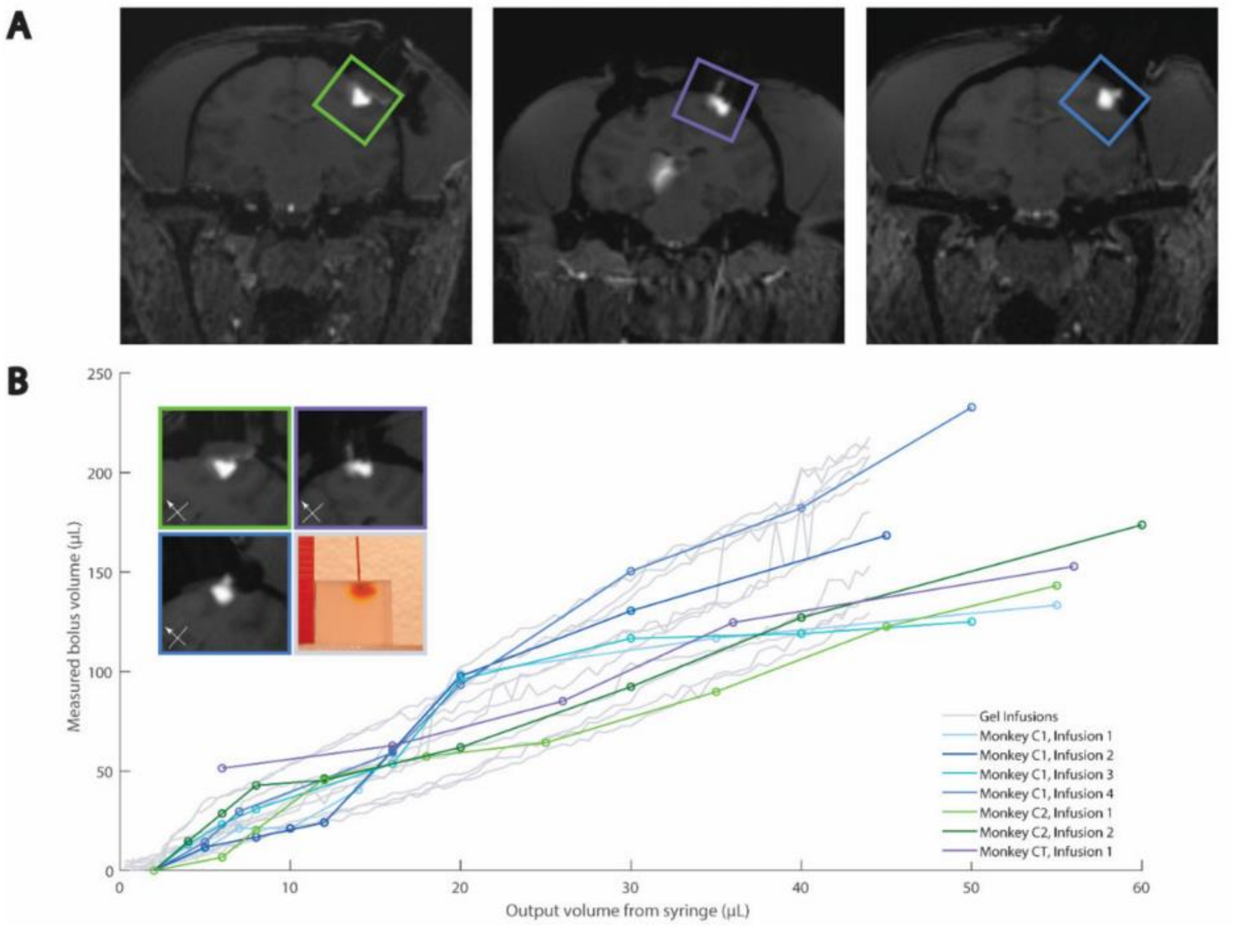

Figure 3.4: Comparison of agar and MRI cortical CED

(A) Example MRIs of cortical infusions. (B) Quantitative and example qualitative (inset) comparisons of agar and NHP data. Box colors in inset relate to images in (A) and traces in (B). Reprinted/adapted with permission from Ref. [8]. Copyright 2016, Neuron.

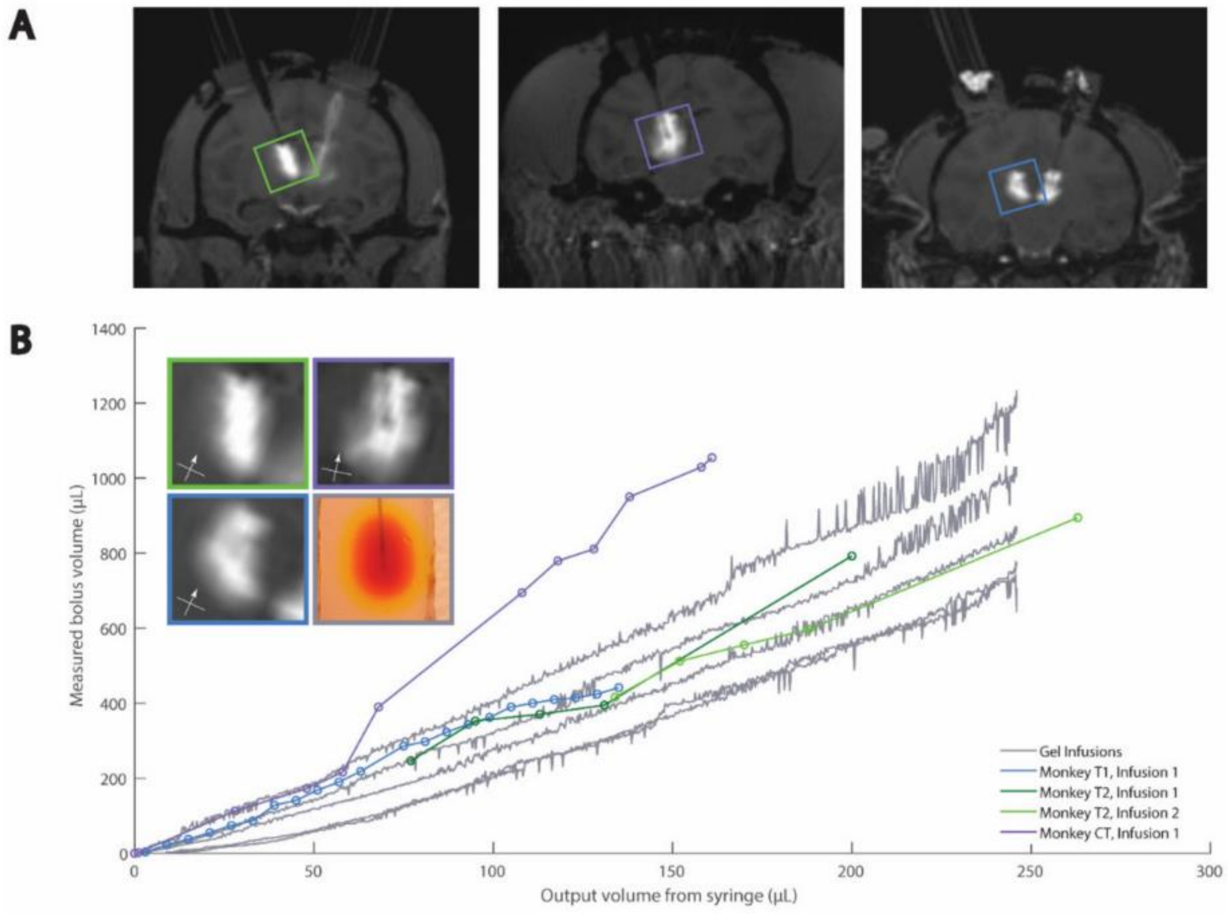

Figure 3.5: Comparison of agar and MRI thalamic CED

(A) Example MRIs of cortical infusions. (B) Quantitative and example qualitative (inset) comparisons of agar and NHP data. Box colors in inset relate to images in (A) and traces in (B). Reprinted/adapted with permission from Ref. [9]. Copyright 2018, Journal of Neuroscience Methods.

3.3.2 MTL INFUSIONS

Our MTL NHP data were highly variable, and upon analysis of the MRI scans, we observed that four of the nine infusions displayed a bolus in the MTL as expected (Figure 6A). We only modeled these four successful MTL NHP infusions and omitted the remaining five infusions, which are discussed below (Section 3.2.1).

Because the thalamic and MTL NHP infusions used similar cannulas and differed chiefly in the infused volume, we initially compared the thalamic agar bolus volumes with MTL NHP bolus volumes (Figure 6B). Counter to our expectations, the MTL NHP data did not align with either the thalamic NHP or agar data. We recognized that while the cortical and thalamic MRI scans were collected during CED infusion, the MTL MRI scans were collected the next day. Therefore, we reasoned that a CED-generated bolus may diffuse overnight and thus be displayed as a larger bolus in the NHP when MRI is performed the day after infusion. With this in mind, we proposed that the diffusion of food coloring in agar after a standard CED protocol would approximate our MTL data. We collected data following the end of 15 µL infusions into agar and observed that the agar data closely modeled the NHP data after approximately 29 min of diffusion following the completion of the infusion (Figure 7). We calculated the mean of the NHP infusion volumes and the mean of the agar infusion volumes selected approximately 29 min after infusion completion (Table 5), and report a 3.5% percent error between the two datasets. Given the biological context of our model, this error is small enough to safely conclude that 29 min of diffusion in our agar phantom, following CED, approximates the next-day MRI results of NHP MTL infusions. Because of limitations imposed by our experimental protocols, multiple sedations and post-operative MRIs were not performed. However, future studies should validate our single point observation by looking at manganese spread across multiple time points.

The green component and threshold value of 100 (39% of green component intensity range) were best to model the MTL infusions. We used a t-test to compare the two NHP data points for the 15 µL infusions and two data points for the 20 µL infusions, and because the two populations were not statistically significant (p = 0.56), we pooled the four NHP data points for comparison with the agar data. Significant noise was observed in the MTL agar data, more so than in the cortical and thalamic agar infusions. The additional noise was possibly due to the smaller infusion volumes. We addressed the noise by fitting a line with linear regression to each agar infusion trial and removing data points greater than 1.1 times the corresponding value on the best-fit line.

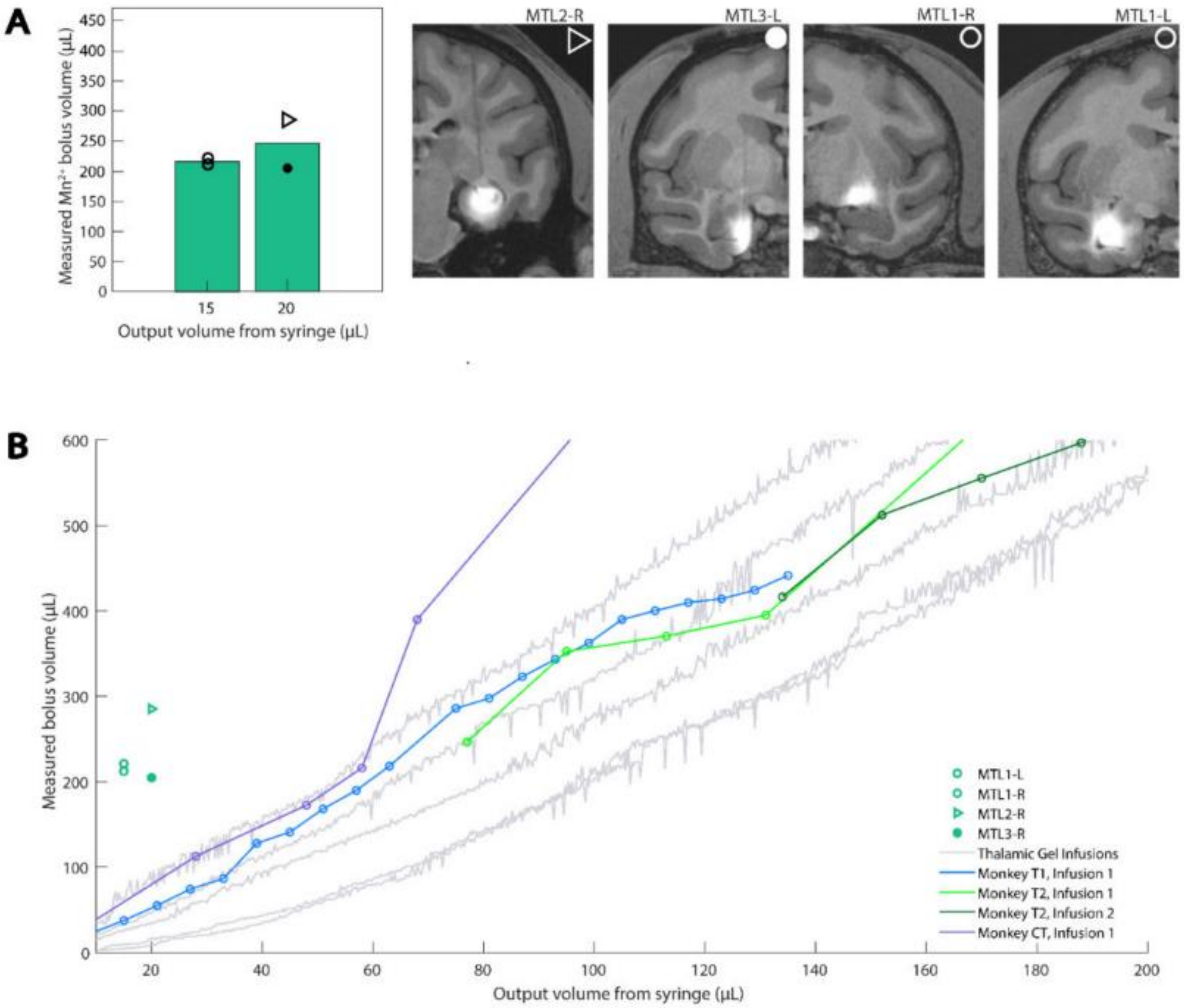

Figure 3.6: MTL MRI data compared with both agar and MRI thalamic data

(A) Deep CED infusions were made into the hippocampus, entorhinal cortex, and the tail of the caudate nucleus. Bar plots show the mean value of measured Mn2+ bolus seen in next-day, post-operative MRIs, with individual data points overlaid. Corresponding MRI slices in the coronal plane are shown for infusions into deep brain areas, which are visually similar to cortical and thalamic data. Shape labels correspond to each subject contributing to the data. (B) MTL MRI data compared with both agar and MRI thalamic data. Reprinted/adapted with permission from Ref. [9]. Copyright 2018, Journal of Neuroscience Methods.

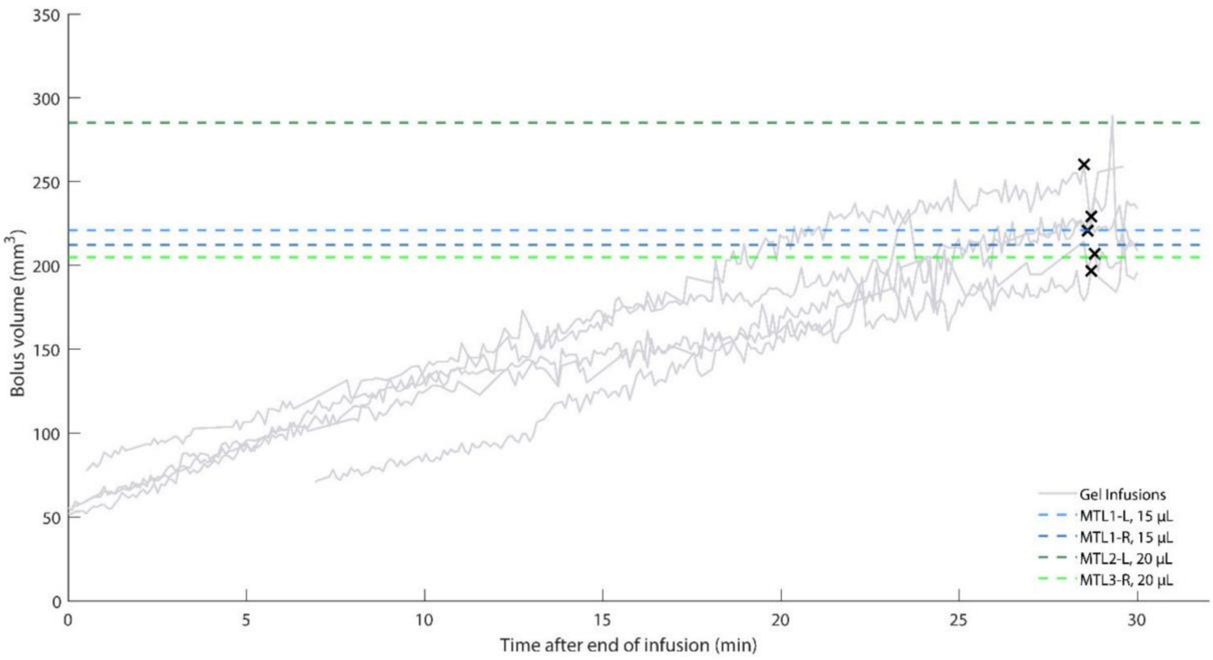

Figure 3.7 MTL MRI data compared with MTL agar data after CED completion

Some trials lack data early in the diffusion process due to the bolus being difficult to identify. Black Xs indicate the final point used for statistical analysis from each agar trial. The final chosen points may be shifted slightly to avoid noise spikes. All agar infusions were 15 µL.

NHP, Hemisphere	**Infusion Volume (μL)**	**Measured Volume (μL)**
MTL1, left	15	221.1
MTL1, right	15	212.2
MTL2, left	20	285.3
MTL3, right	20	204.7
Average:		**230.8**
Gel Trial	**Infusion Volume (μL)**	**Measured Volume (μL)**
1	15	196.7
2	15	229.2
3	15	260.2
4	15	220.7
5	15	207.0
Average:		**222.8**
% Error:		**3.5**

Table 3.5: MTL data

3.3.2.1 MTL Data Omitted from Agar Modeling

Five of the nine NHP MTL infusions were excluded from the analysis since the next-day MRI did not confirm infusion into the MTL regions (Figure 6 and Supplementary Figure S3). These failed infusions mostly likely occurred due to the complex shapes of the hippocampus and neighboring structures, which contrast with the structures of the cortex and thalamus. In three of the five unsuccessful MTL cases, the boluses were very small, which suggested either puncturing into the hippocampal fissure, or infusing deep in the dentate gyrus, depending on the injection depth (Supplementary Figure S3). Penetration of the fissure resulted in contrast agent and virus partially escaping our injection target, indicative of unsuccessful CED. By contrast, deep dentate gyrus infusions were limited to a small portion of the hippocampus, limiting the amount of diffusion observed when compared to our gel model. In the remaining unsuccessful case, the bolus was very large and extended well outside of the volume of the hippocampus, indicating that the contrast agent refluxed along the track of the cannula (Supplementary Figure S3). We excluded these five unsuccessful MTL CED data points from our models, but these negative results are presented to highlight the value of in vivo verification of deep injection surgeries.

3.3.3 HISTOLOGICAL ANALYSIS

For cortical and thalamic infusions, the spread of the MR contrast agent modeled the volume of expression of the optogenetic viral vector, as previously analyzed and reported [8,9]. We used different constructs, including retrograde viruses, for our MTL infusions. Because of the variability of the resulting expression, further experiments using a single virus known to express well in these regions is necessary to confirm whether the next-day, Mn2+ MRI signal mirrors expression. Nevertheless, the Mn2+ MRI confirmed our targeting in vivo. Additionally, preliminary evidence from the successful local infection in case MTL4-L suggests a close match between Mn2+ signal and immunofluorescence (Figure 8).

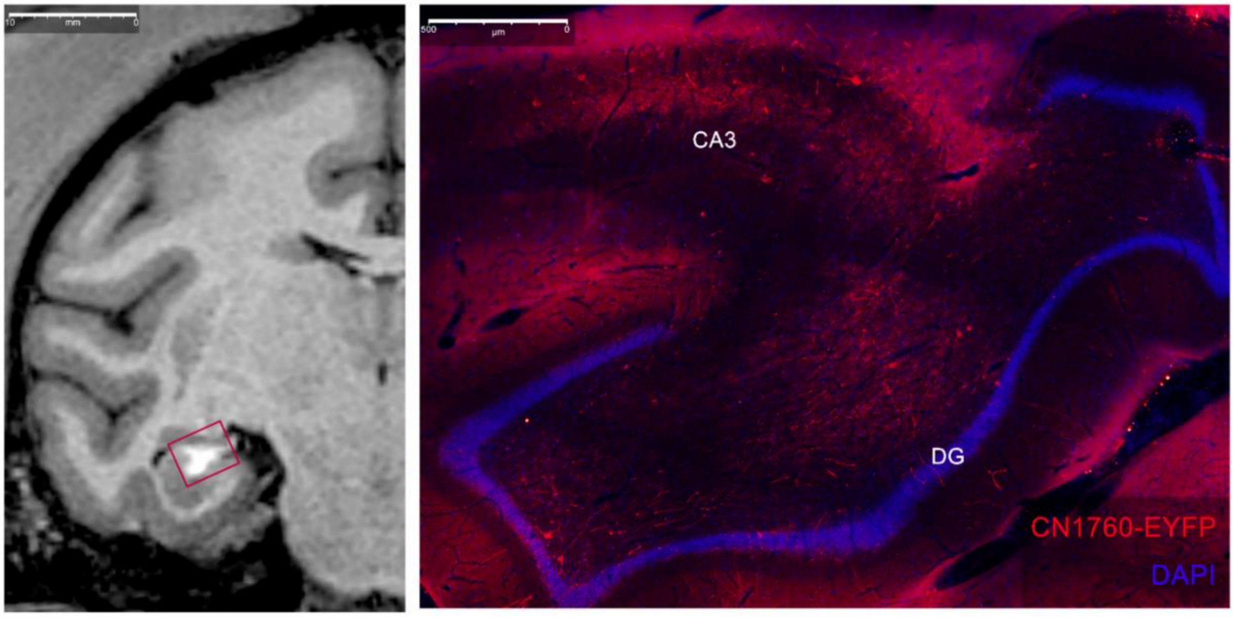

Figure 3.8: Relationship between manganese signal and viral infection

Comparison of Mn2+ MRI signal (left) and local expression of virus (right) after a hippocampal injection in case MTL4-L. Right-imaged region highlighted with red square in MRI (left). Our virus used a GABA-specific enhancer to selectively target interneurons, as evidenced by a lack of red pyramidal cell body labeling in CA3 and granule cell body labeling in the dentate gyrus (DG). We tagged infected interneurons and associated fibers with red-shifted fluorophores (anti-EYFP, ThermoFisher, Waltham, MA, USA) and cell bodies were non-selectively labeled using a DAPI stain (ThermoFisher, Waltham, MA, USA). (Viral construct CN1760: trAAV-3xhI56i(core)- minBG-ChR2(CRC)-EYFP-WPRE3-BGHpA (Paul Allen Institute, Seattle, WA., USA)).

3.4 DISCUSSION

Targeted neural manipulations, such as those achieved via optogenetics, are revolutionary techniques for investigating circuit-level communication in the brain and have the potential to influence novel neurotherapeutic technologies in humans. NHPs are the keystone model for validating these techniques because of their similarity to humans, but they are a scarce resource that does not allow for experiments with many unknowns. As such, the risks associated with the viral infusions necessary for most genetic manipulations have led to a lack of uniformity in experimental design and much trepidation in engaging this type of research [29]. In this work, we developed a simple and efficient pipeline to ameliorate a number of these concerns. Our method improves upon past models [7,20,21] by quantitatively matching agar data with in vivo infusions of viral particles co-infused with MRI contrast agents, which serve as a proxy of the effective infusion volume. Further, we observe that certain contrast agents can signal the location of infusions up to 24 h post-infusion, which is a greater time delay for bolus localization than previously demonstrated [26]. Taken together, the methods presented here serve as an accessible and inexpensive protocol to plan the optimized spread of infusions bench-side and validate the spread and accuracy in vivo, significantly reducing the number of unknowns that hinder confidence during circuit-manipulation experiments. Our presented methods contribute to a body of work supporting large-scale optogenetics in NHPs [8,9,16–19,22,23,30–39].

Agar has been previously established as a model of intraparenchymal neural tissue and is now commonly used as a medium for simulating infusion procedures [7,20,21]. Our work builds on prior studies by presenting a data-driven method developed from in vivo results. To our knowledge, the model proposed here is the first to provide a quantitative method of fitting agar infusion data with NHP CED data collected with live MRI. Because of this, our model serves as a more accurate guide for selecting infusion parameters for future in vivo infusions targeting a wide array of brain areas when compared to other simulations.

Our work lends itself well to case-by-case methodological refinements: for example, researchers may consider alternative cannulas, infusion protocols, etc., to cater to their goals. Additionally, our method is designed to facilitate replication by other labs with its simplicity in both materials and methods. We also recognize that labs replicating our work are unlikely to implement agar infusion imaging setups identical to our own. With this in mind, we designed our image processing technique to be easily adaptable to different imaging setups. We provide NHP MRI bolus volume data (see Supplementary Materials) to which other labs may align their own agar infusion data, using our presented method. We have also made our custom code freely available (see Data Availability Statement), and the code is written in MATLAB, which is widely used by researchers and is straightforward to adapt for applications akin to ours.

3.4.1 DIVERSITY OF MODELED STRUCTURES

To maximize the flexibility in accurately predicting spread of CED infusions in a variety of brain areas, we used in vivo data from cortical, thalamic, and MTL infusions of viruses co-infused with MRI contrast agent. Our cortical and thalamic procedures, which represented shallow and deep infusions into large brain structures, utilized live MRI taken during surgery. In addition to the qualitative agreement between these infusion types, the ranges of MRI data best-fit slopes were similar (2.9–4.6 µL/µL for cortical and 3.5–6.4 µL/µL for thalamic), which suggested that the agar models for cortical and thalamic infusions may be similar as well. This proved to be the case. Despite differences in the cannula design, depth of insertion, and infusion protocol, the models for both cortical and thalamic CED were generated with our same presented method and aligned well with the in vivo data (agar model best-fit slopes were 2.7–4.8 µL for cortical and 2.6–4.4 µL/µL for thalamic). The cortical and thalamic models did differ in the parameters used during image processing (cortical: blue component, threshold = 67; thalamic: green component, threshold = 110), but this demonstrates that our method is robust to variations in agar infusion processes. Our successful MTL cases differed from the previous two conditions and represented infusions into more limited and more difficult to access deep structures. Additionally, they differed in their post-operative MRIs in that scans were taken ~20 h after infusion. We found that our initial hypothesis of these data aligning to the thalamic cases was invalidated. However, after accounting for diffusion expected from the delay in imaging, our model successfully aligned to all three conditions.

3.4.2 INSIGHTS FROM MTL INFUSIONS

Because of its unfurled shape in primates compared to rodents [40], standard injections into the NHP hippocampus are laborious and often require either multiple craniotomies and penetrations [41], or penetrating through the long-axis of the structure and periodically injecting while retracting [42] to try and maximize coverage. To inject into this structure more efficiently, we leveraged the unique ability of CED to deliver a large bolus with a single infusion in our MTL CED group, which, to our knowledge, is the first set of CED infusions delivered to this area in NHPs. Because of the exploratory nature of these experiments, we experienced challenges that made delivery into this structure and subsequent imaging of our contrast agents more difficult. Infusion MTL2-L was a case of mass reflux due to an error made during the infusion delivery. MTL3-R and MTL4-R represent issues in targeting. Because much of the hippocampus is separated from the rest of the brain by ventricular spaces except laterally, targets made too shallow or too deep will leak into those spaces and either dissipate away or reflux upwards. For similar reasons, posterior–medial injections—for example, targeting the intermediate dentate gyrus—produced more isolated boluses (cases MTL4-L, MTL5-R). Our successful cases were qualitatively similar to our cortical and thalamic data because they were delivered to larger, more anterior regions in the genu of the hippocampus, or to large neighboring regions such as the entorhinal cortex or tail of the caudate nucleus. For areas such as MTL, where targeting needs to be very precise, we strongly recommend the use of MRI validation of injection either during infusion or the next day.

3.4.3 MRI SCAN PARAMETERS FOR SUCCESSFUL CONTRAST LABEL VISUALIZATION

Our novel MTL infusions were also the first to utilize co-infused manganese to localize viral infusions in MRI scans acquired ~20 h post-operatively. Despite the differences in the employed contrast agent, scan acquisition timing, and even the scanner used between this group and our cortical and thalamic infusions, we observed a few similar parameters for successful contrast imaging in all MRI scans for all groups. Specifically, all scans were T1-weighted scans with a repetition time/echo time ratio around 2 to 3 and flip angles from 9 to 30 degrees. Analysis of other studies employing similar manganese-enhanced MRI protocols either to image viral injections delivered at shorter delays [26] or at much longer delays for in vivo tract tracing [43] also closely mirrored the majority of the parameters used in these experiments, suggesting a range of optimized parameters for imaging T1-weighted MRI contrast agents.

3.4.4 DIFFUSION VERSUS CONVECTION USING AGAR

It is important to note that while agar is a good model of CED, agar's rate of diffusion differs from the rate of diffusion in the brain. This factor became apparent when we observed that a reduction of flow rate at the end of the cortical agar trials led to a greater increase in the bolus volume with respect to the infused volume, i.e., the plots steepen near the end of the infusion protocol (Supplementary Figure S2). This is consistent with our observation that diffusion will continue to cause the bolus to grow in agar after the end of our infusion trials. With this in mind, we concluded that diffusion and convection both contribute to bolus size in agar to varying degrees during CED. However, we propose the relative contributions of diffusion and convection were skewed when the flow rate was reduced at the end of the protocol, thus allowing diffusion to contribute more heavily to the bolus size in the agar. To prevent the best-fit lines of the cortical agar data from being skewed due to this effect, we omitted the data from 44 µL to 50 µL from the statistical analysis and Figure 4. This effect was not observed in the thalamic agar infusions, likely due to the lower maximum rate of infusion (3 µL for the thalamic agar protocol, as contrasted with 5 µL for the cortical agar protocol) in conjunction with the short duration of infusion at the lower rates and small amount of volume infused during the flow rate reduction at the end of the protocol. This effect was not observed in the in vivo cortical or thalamic injections collected with live MRI. We observed diffusion in our in vivo MTL data, but the data were collected with our next-day imaging technique, thus allowing sufficient time for diffusion. We show that MTL next-day imaging data aligns well with our agar phantom when we allow 29 min of diffusion following the end of the infusion protocol. However, future imaging at multiple time points should be performed to validate this initial finding. This highlights that the speed of diffusion in agar differs from that of the brain. This is also in agreement with our observation that the cortical and thalamic

NHP data collected with live MRI did not exhibit high levels of diffusion at the end of the protocols, in contrast to the cortical agar data.

3.4.5 TECHNICAL CONSIDERATIONS

We encountered some issues during the agar infusions. The most common issues faced when refining the infusion techniques were damaging the agar during its extraction from the mold, such that no smooth surface was available for imaging, and reflux of the dye during the infusion. While the agar preparation became more efficient with practice, we suggest that custom, flexible silicone molds be considered in lieu of our 3D-printed molds to more easily produce undamaged agar phantoms. Reflux issues can arise in agar, neural tissue, and other media and are less easily mitigated because the cause of reflux is not always obvious. In some cases, the reflux may be related to the quality of the seal between the media and cannula, which is difficult to assess visually even in transparent media such as agar. Additionally, we hypothesize that, in some cases, the cannula becomes clogged with the media during insertion. To address this potential issue, we suggest a low flow rate during insertion to avoid clogging.

As previously mentioned, the agar data are aligned with the in vivo MRI data with an iterative process of parameter selection. The iterative alignment process allows researchers to fine tune their image processing parameters to overcome potential differences in lighting, camera placement, etc. While our agar image processing techniques are effective, we acknowledge that software refinements may be attained. Our process is currently semiautomated, yet we expect it could be more fully automated in future work. Improvement opportunities may also exist in the refinement of our volume estimation formula, and the characterization of the bolus shape.

3.4.6 ETHICAL CONSIDERATIONS

Despite the limitations presented, our methods will allow for the development of more efficient and effective CED procedures. We can inexpensively plan the expected spread of our infusions with our data-driven model and validate our surgical targeting rapidly without the need to perform infusions in an MRI scanner. Critically, our method is not only quantitative and data-based, but also designed to aid surgical planning with its visual, hands-on nature. Our bench-side modeling technique serves to increase the likelihood of success in NHP CED experiments, thus refining animal research processes and reducing the number of animals required for experimentation, both of which are key ethical considerations in animal research and included in the 3Rs [44]. Our model was capable of simulating both cortical and deep infusions (limitations discussed above). Because of this, our method provides a generalized surgical preparation technique to all researchers regardless of region of interest, and particularly to research groups that do not have the facilities or resources required to perform live MRI during CED infusions. Our novel next-day MRI data additionally serve to showcase a post hoc infusion confirmation method that improves upon previous work [26] to highlight the verification of infusion placement ~20 h post-operatively. This method supplements our proposed modeling technique and is a welcome alternative to live MRI, which requires specialized equipment and facilities often unavailable to researchers. In sum, we propose our method as an additional way of applying the principles of replacement, reduction, and refinement (3Rs) to injections in NHPs [44,45]. We recommend NHP CED infusions be modeled in advance of surgery with our proposed method to reduce the number of animals, replace an excess of pilot procedures with artificial simulations, and refine the overall technique to reduce harm. We also suggest the results be confirmed after surgery with MRI if live MRI is not feasible during infusion. Finally, our work is designed to be highly flexible. While our methods are specifically prepared for NHP experiments involving optogenetic actuators, we expect that our method would also be generally effective for modeling the CED of optogenetic sensors, pharmaceutical compounds, and other therapeutic agents in large brains.

3.5 SUPPLEMENTARY MATERIALS:

FIGURE S 3.1: 3-MM (LEFT) AND 1-MM (RIGHT) STEPPED-TIP CANNULAS.

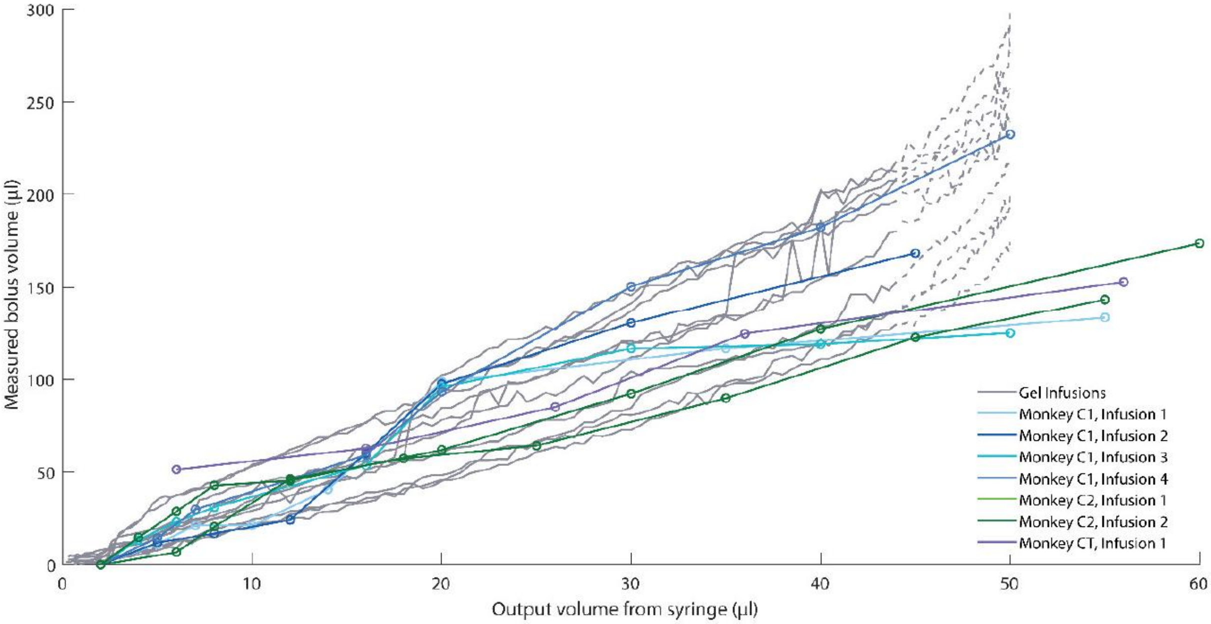

FIGURE S 3.2: COMPARISON OF AGAR AND CORTICAL CED.

THIS FIGURE IS THE SAME AS FIGURE 2.4B WITH THE ADDITION OF DATA (DASHED LINES) FROM 44UL TO 50UL, WHICH WERE OMITTED FROM STATISTICAL ANALYSIS DUE TO THEIR

progressively steep upward trend that did not align with the MRI data. MRI data has been previously published [8].

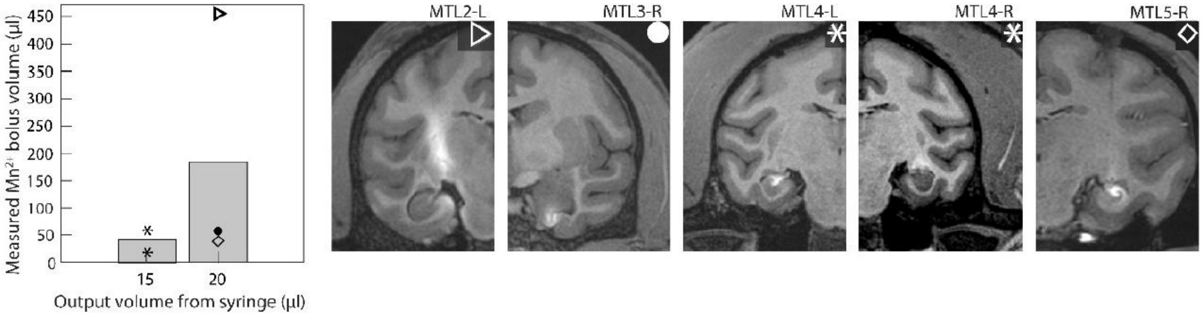

Figure S 3.3: Maligned MTL Data.

In addition to the deep infusions presented in figure 6A, some infusions were not visually similar to cortical and thalamic data. These deep CED infusions were also made to the hippocampus, entorhinal cortex, and the tail of the caudate nucleus. Bar plots show the mean value of measured manganese signal observed the next-day, post-operative MRIs, with individual data points overlaid. Corresponding MRI slices in the coronal plane are shown. Shape labels and correspond to each subject contributing to the data.

3.6 ACKNOWLEDGMENTS

We would like to thank all of the staff from the University of Washington, Seattle, and University of California, San Francisco, who provided animal care and surgical support. We thank Sabes lab for use of their previously published data. We thank Spencer Hansen, Serge AleshinGuendel, and Tianyu Zhang for their help with statistical analyses. We thank the Viral Technology team at the Allen Institute for Brain Science, Ximena Opitz Araya, Shane Gibson, and Greg Horwitz for assistance with virus production. Finally, we thank Toni Haun, Karam Khateeb, and Megan L. Jutras for their technical help.

CHAPTER 4 || CO-OCCURRENCE OF SHARP WAVE-RIPPLES ACROSS THE LONGITUDINAL AXIS OF THE PRIMATE HIPPOCAMPUS

4.1 INTRODUCTION

Hippocampal sharp wave-ripples (SPW-R) are some of the most synchronous phenomena observed within the entire brain of all mammalian species (1). They are a two-part, complex signal observed in local field potential (LFP) recordings that consists of a burst of high-frequency (100-250Hz) activity nested within a large-amplitude sharp wave lasting ~100ms (1, 2, 3, 4). These complexes are first generated when spontaneous, synchronous potentiation of CA3 pyramidal cells induce large transmembrane currents at the nearby apical dendrites of CA1 pyramidal cells (1,2,4). These currents are identified in the LFP as the sharp wave. The depolarization induced by the sharp wave is sufficiently large to recruit both CA1 pyramidal cells and CA1 inhibitory interneurons, and this interplay between excitation and inhibition both induces and limits the high-frequency ripple event (1,2,4). Although sharp waves and ripples are dissociable phenomena (17,18), SPW-Rs as a complex are highly coupled and are typically present during quiescent periods and slow wave sleep (1,8). They can also be identified in LFP recordings while animals are immobile (1,2,6) and during consummatory behaviors such as eating or grooming (1,7). Single unit activity during SPW-Rs unfolds in sequences that mimic the sequential firing patterns observed as animals perform memory-associated behaviors and navigation, albeit at a compressed time scale (1, 3, 8). Manipulating SPW-R generation has profound effects on memory performance and highlights the strong link between this hippocampal phenomenon and memory consolidation and working memory performance (9, 10).

Most of our understanding regarding SPW-Rs comes from studies in rodents, but SPW-Rs in monkeys have also been identified with similar phenotypes as rodent SPW-Rs (11, 12). Yet, studies of primate SPW-Rs are scarce, and many unanswered questions remain- such as if the generation of sharp waves and ripples in the monkey mirrors the rodent ontogeny. Additionally, it has been discovered that ripple activity recorded across the rodent hippocampus co-occurs in two unique motifs along the longitudinal axis (13). Specifically, ripples generated in the dorsal two-thirds of hippocampus spread to other aspects of the dorsal hippocampus and occur independently from ripples observed in the ventral third of the structure in rodents. This segregation of ripple co-occurrence reflects both the intrinsic connectivity patterns across the hippocampus and exogenous afferents from the hippocampus' main cortical input, the entorhinal cortex (19). Thus, identifying whether ripple propagation occurs as a result of changing exogenous or intrinsic is non-trivial to understand from rodent LFP recordings.

In contrast to rodent, the primate hippocampus has different intrinsic and extrinsic connectivity schemes. Tracing experiments from David Amaral's lab reveal that intrinsic connections from CA3 to CA1 in primates reach multiple lengths and can span the entire longitudinal extent of the primate hippocampus (20). Conversely, inputs from entorhinal cortex maintain a topographic organization to the hippocampal long axis (14, Chapter 1). As a result, if exogenous input from entorhinal is driving ripple activity, then in primates we should observe hippocampal ripples that have limited spatial spread. On the other hand, ripples are likely to co-occur across the entire hippocampal long axis in primates if these phenomena are sustained by intrinsic drive. Previously, this has been impossible to study because of limitations with recording technologies, and differences in ripple detection between rodent studies and primate studies make identifying true ripple events non-trivial. However, in the wake of new consensus on SPW-R identification methods (1) and chronic recordings that span the entirety of the hippocampal A-P axis, we now stand ready to ask what motifs for co-occurring SPW-Rs exist in the primate hippocampus.

In this chapter, I share findings from three monkeys with 124-channel, chronically implanted hyperdrives centered over the hippocampal formation (Gray Matters, Inc.). During restful periods we detected a plethora of SPW-Rs across the entire primate hippocampus with similar phenotypes to previous monkey and rodent studies. Detection of these SPW-Rs was not limited to any region of the hippocampal long axis. Furthermore, some events were shown to co-occur in multidirectional patterns that included uni-directional, simultaneously multi-directional, and even rebounding phenotypes. Importantly, the co-occurrence of ripples was not strictly spatially limited or biased for a particular direction of travel. These findings suggest that the primate hippocampus engages in organ-wide network communication with cortex during non-exploratory periods that is predominantly driven by intrinsic excitability. These findings have strong implications for the mechanisms of communication between the hippocampus and recurrently connected cortical areas during memory consolidation events.

4.2 METHODS

4.2.1 SUBJECTS, BEHAVIORAL PROCEDURES, AND IMPLANTATION METHODS

Data from three young monkeys (2 male, 1 female) weighing between 7 and 13kg was utilized for this study. Monkeys were housed in singular cages but were paired when possible, and all animals had constant visual access to other conspecifics in their housing room. All animals received a wide array of enrichment in the form of various food and toys. Monkeys were trained using appetitive reinforcement to sit in a custom-made primate chair (WaNPRC Machine Shop) and engage with either a large projector for various virtual reality tasks (MK1-2, male subjects) or a computer screen and electro-receptive touch bar (MK3, female subject) (Fig. 4.1a). During task engagement, monkeys were rewarded with a custom-made slurry consisting of recipes tailored to each animal's preferences that included their standard monkey "chow", bananas, and other rewarding sweets. After acclimation to the primate chair and testing environment, animals were implanted with a titanium rod (Gray Matters, Inc) for head-fixing procedures. Following a six-week recovery period, animals were trained to sit upright in the chair, let a neck plate come through the chair to maintain that position, and allow themselves to be headposted to the primate chair. All training was again performed only using appetitive, positive reinforcement.

Once animals were reliably headposted without issue, implantation of the 124-channel hyperdrive occurred over the course of two procedures (Fig 4.1b). First, a custom-built chamber (Gray Matters, Inc) whose base was custom-shaped to the skull of each monkey using pre-operative MRIs was cemented to the animals' skulls over predetermined coordinates that would ensure sufficient hippocampal targeting by the wires in the drive (also identified with pre-op MRI). Subsequently, a transcranial window was created by removing the skull within the bounds of the chamber, and the drive was slowly lowered into the chamber—

hovering just above the now exposed brain. Wires, spaced 1.5mm apart in an 8x16 grid (except the first and 16th column which only had six wires instead of eight) and loaded in the drive by spring-loaded screws, were meticulously lowered incrementally in surgery and over the course of the animals' recordings using precise turn estimates detailed in section 4.2.2 (Fig 4.1c). Final testing procedures consisted of the implanted monkeys getting headposted and alternating between their respective computer-based tasks (~60mins) and sitting in ambient lighting as an inter-session rest period (~10mins).

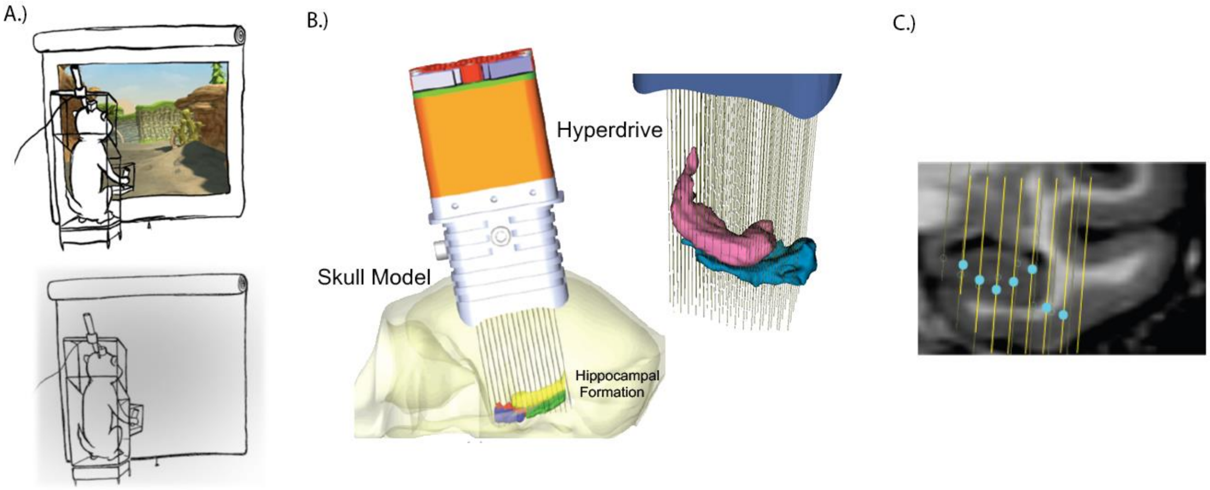

Figure 4.1 Behavior Paradigms, Electrophysiological, and Electrode Position Estimates

(A) Illustration of behavioral setup. Monkeys were headfixed and sat in front of a projector screen, alternating between various virtual-reality behaviors and sitting in darkness. (B) 3-D models of the hyperdrive placement on the skull, as well as the grid of electrodes spanning hippocampus. (C) Example estimates of recording electrode alignment and daily estimates of position based off co-registered estimates.

4.2.2 ANATOMICAL LOCALIZATION

As mentioned, monkeys underwent a pre-operative MRI for drive placement estimates, and a second scan was performed after initial hyperdrive chamber placement. The post-operative MRI included a set of fiducial markers mounted on the animals' heads to estimate the angle and placement of the drive. However, because of distortion induced by the chamber, final models of alignment were generated (.STL) using a combination of post-operative measurements, stereotactic X-rays, and 3D laser scans of the animals' heads and drives.

The starting positions for each electrode were estimated from the drive alignment models. Electrodes were manually turned down into desired recording locations using precise turns of screws at the drive base. Turns were manually logged, and electrode distance across all recording sessions was estimated using the measured distance correlation from one full turn during non-implanted practice turns. These distances were transformed into 3-D coordinates using the alignment models as a starting reference. X-ray images were used to confirm that electrode trajectories did not deviate, and any electrodes not progressing in a straight line stopped being turned. Models of the hippocampal formation (.STL) were made in an MRI processing suite (3D Slicer), and scripts for estimating 3D position of each electrode were made in MATLAB that incorporated information from turn count estimates and drive placement estimates. Subregion determination was performed automatically by comparing an electrode's 3D position estimate and the 3D coordinates of manually identified hippocampal subregions from the MRI, and these determinations were manually verified by comparing positions in the MRI. Data was analyzed from sessions where the majority of electrodes were optimized for experimenter-identified SPW-R presence.

In primates, the hippocampus unfurls relative to that of rodent such that it largely extends anterior-posterior rather than dorso-ventral. Additionally, the primate hippocampus is impacted by the temporal pole, resulting in the most anterior elements of the hippocampus folding over themselves medially. To parcellate the hippocampal long axis, we first divided the hippocampus into equally spaced subsections approximating 1.5mm moving from the most posterior row of the recording drive to the genu of the hippocampus. However, because the primate hippocampus folds over on itself anteriorly, we rotated the axis twice. First, for channels located in the genu anterior to the fundus of the uncus, we advanced the long axis in the medial-lateral direction. Then we rotated and reversed the axis going posterior-anterior for wires located in the uncus of the hippocampus. An illustration of the long axis and our parcellation of electrodes along it can be observed in Fig 4.2a, and individual assignments for all three subjects can be seen in Fig 4.2b.

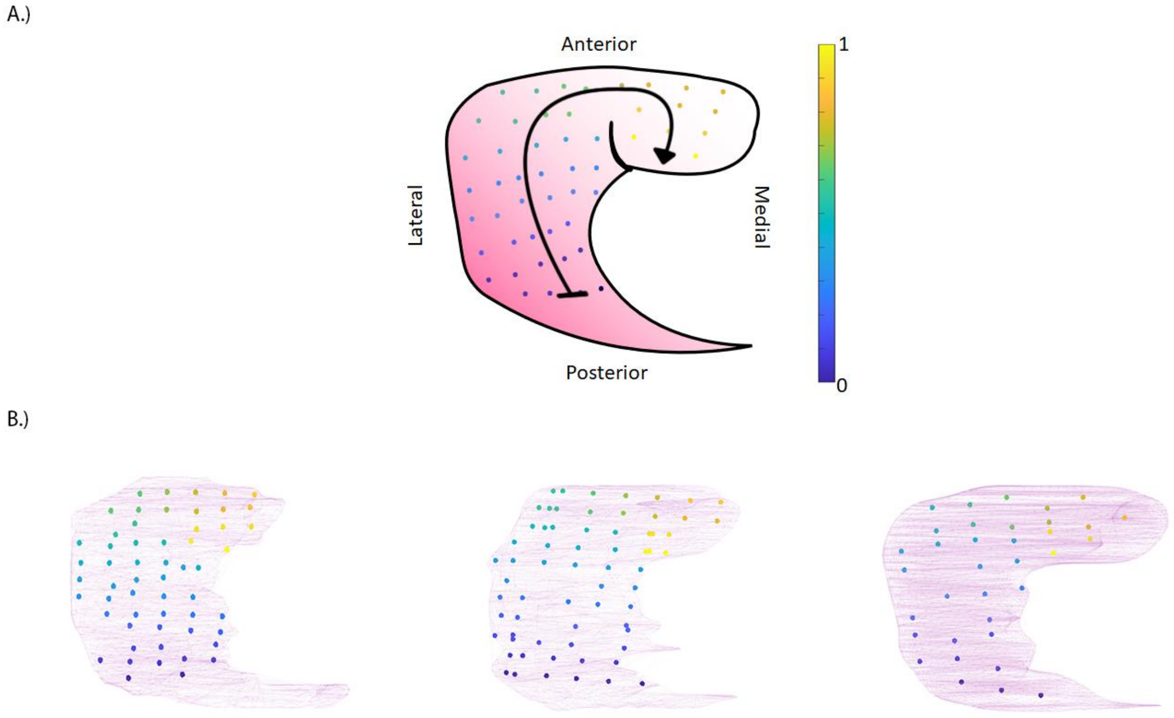

Figure 4.2 Manual Subdivision of the Hippocampal Long Axis

(A) Axial-view Illustration of the primate hippocampus, as well as an idealized parcellation of electrodes across the longitudinal axis (expressed as a black line). (B) Individual 3-D models of our subjects’ hippocampi and assignment of hippocampal electrodes (MK1: Left, MK2: Middle, MK3: Right).

4.2.3 DATA ACQUISITION AND LFP PRE-PROCESSING

Data from each wire/channel was collected using a Neuralynx Cheetah system (v6.0). Neural signals were collected at 32kHz and collected in wideband format (0.1-8000Hz). For LFP collection, data was first low-pass filtered (0.1-1000Hz) to avoid aliasing and then downsampled to 1KHz. During collection, data was referenced to the animals' headpost implant to mitigate contamination of collected signals by volume conducted noise. Data from each channel was manually inspected to identify strong contamination by 60Hz line noise, and in cases where line noise obfuscated the underlying recordings, data was notch-filtered using a spectrum interpolation technique presented Mewett et al. (18). Signals were then mean centered and normalized (z score) prior to further analysis.

Because of heavy contamination by extrinsic noise, the data required additional offline artifact removal using either independent components analysis (ICA) artifact removal, or a novel approach using the singular value decomposition (SVD). The novel artifact removal is discussed in detail in chapter 5, however it is worth noting that prior comparisons between principle components analysis (PCA), which SVD is a generalized version of, and ICA have found the two methods similar in quality as artifact rejection methods (15, 16).

4.2.4 SINGLE CHANNEL SHARP WAVE-RIPPLE DETECTION

Existing methods for SPW-R detection have recently been criticized for using improper descriptive statistics on amplitude distributions and setting arbitrary detection thresholds that change wildly across labs (1). In a recent consensus statement put out by researchers across many labs, including our own, and working with various species, the authors propose forgoing parametric statistics (i.e. z-score, mean, and standard deviation), and using alternative means of thresholding and identifying ripple events (1). Thus, our ripple detection method employs novel methodology to identify SPW-R events. The entire pipeline can be observed in Figure 4.3. First, we filtered our recorded LFP into the ripple band (95-180Hz). Two 25ms moving averages (one prospective and the other retrospective) were taken and then subtracted one another in complex space and subsequently absolute valued to identify smooth changes in ripple band amplitude during candidate events. A significance threshold was generated using the cumulative distribution function (ECDF) of the binned deviations and identifying the value corresponding to the 99.5th percentile of the distribution function. This value corresponds to data in the top 99.5th percentile of ripple band amplitude changes for each individual channel. The starts and ends of candidate events were identified by detecting when the differences in amplitude exceeded our deviation threshold, and timestamps bridging the two events were cross validated using the threshold value for amplitude. Adjacent events occurring <20ms apart were concatenated into a single event. Similarly, candidate events lasting less than 50ms were excluded as candidate ripples. To preclude the possibility of false detection of high-frequency oscillations (HFO; 180Hz-250Hz), candidate ripples with a higher power in the HFO band than the ripple band were excluded from further analysis.

Descriptive features collected for each identified ripple included the starts and ends of the event, center of mass/midpoint, duration, the max, mean, and median amplitudes, the cumulative raw amplitude, and mean and instantaneous frequency. All analyses were performed in MATLAB (Mathworks).

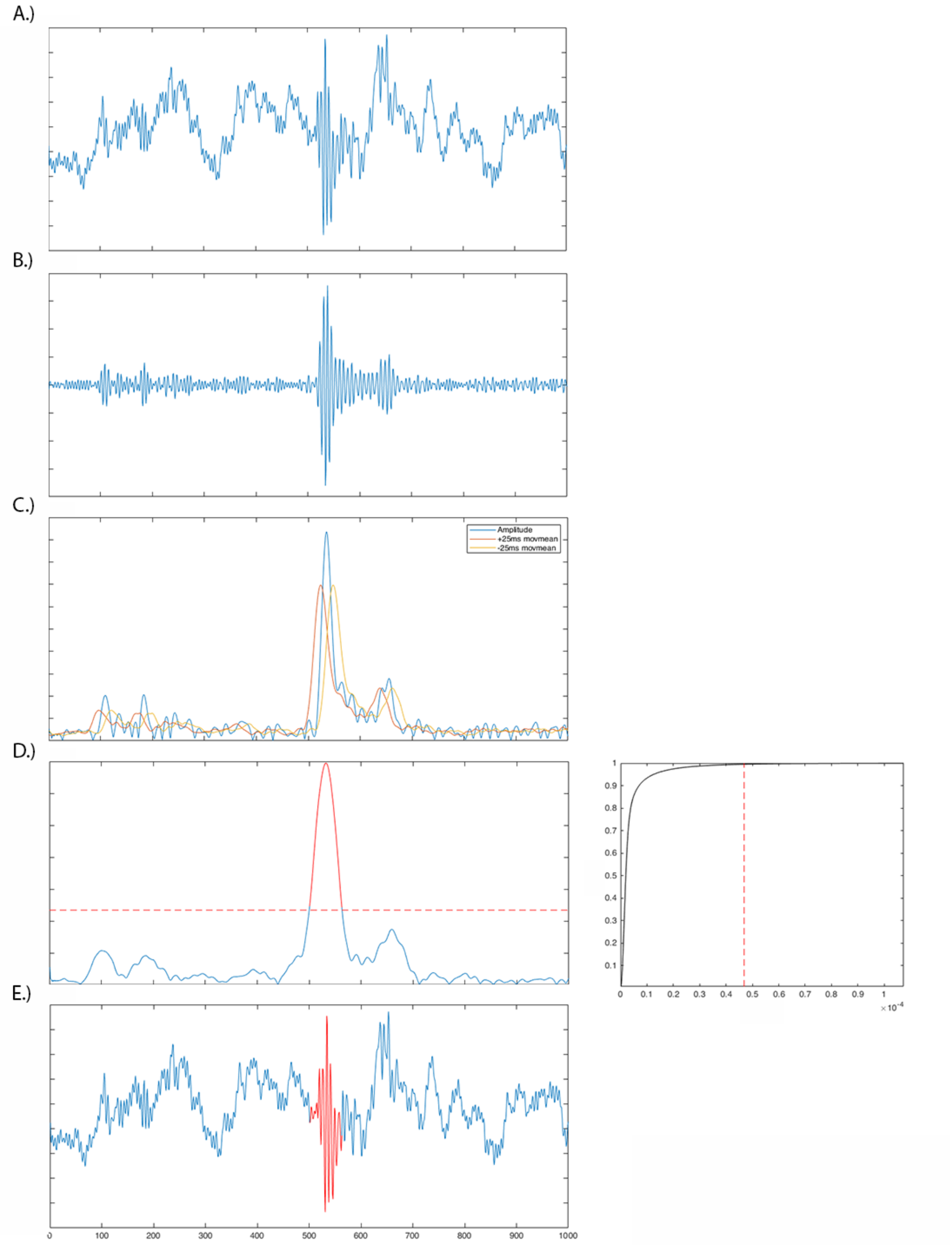

Figure 4.3 Ripple Detection Method

(A). RAW LFP SNIPPET. (B). RIPPLE-BAND (95-180HZ) FILTERED SIGNAL. (C). AMPLITUDE OF RIPPLE BAND DATA, ALONGSIDE PROSPECTIVE AND RETROSPECTIVE 25MS MOVING AMPLITUDE AVERAGES (ONLY REAL VALUES SHOWN). (D). ABSOLUTE VALUE OF THE COMPLEX DIFFERENCE OF THE 25MS MOVING AVERAGES AND AMPLITUDE-CHANGE THRESHOLD DERIVED FROM AN ECDF OF THE DIFFERENCE TIME SERIES. (E) RESULTING RIPPLE IDENTIFIED FROM THE ABOVE PIPELINE.

4.2.5 MULTI-CHANNEL EVENT DETECTION AND ANALYSIS

Once ripples on all individual channels were identified, events across channels with nearby timestamps were concatenated. First, timestamps from each channel were concatenated into a large array sorted by each wire, and corresponding wire indices were placed into a second array of similar size. The timestamp array was then sorted by ascending time, which shuffled the corresponding wire indices. Data was a single, multichannel event if the gap between adjacent timestamps was less than or equal to 30ms. Events pertaining to each multi-channel ripple were amassed into a single structure and ordered by center of mass. To ensure that high-frequency noise was not accidentally collected as a cross-channel ripple, we employed a custom-built GUI in MATLAB (partially shown in Fig 4.5) to manually flag any multi-channel event with unusually high coherence across channels. Coherence was identified using pairwise mean resultant length vectors of ripple-band phase amassed into a confusion matrix.

Although we identify traveling events in section 4.3, because of uneven sampling of ripples across our electrodes, we focused predominantly on assessing the spatial distribution of starts and ends of our multi-channel events, which per the detection described above were the first and last ripple of every identified event.

4.2.5 STATISTICAL ANALYSES

For individual ripples, Pearson correlation coefficients (r) were used to assess whether amplitude, duration, and mean frequency changed as a function of long axis position. Kolmogorov-Smirnov (KS) tests were used to test for significant biases of spatial distribution of starts and end locations of multichannel events, as well as for biases of the distribution of distance offsets by ripples at a given long axis location. A Mann-Whitney U Test (U) was used to quantify significance of ripple spread direction biases for the entire hippocampus.

4.3 RESULTS

4.3.1 SHARP-WAVE RIPPLES ARE GENERATED ACROSS THE ENTIRE PRIMATE HIPPOCAMPUS

LFP recordings were analyzed from 219 recording days (**MK1 = 77 days, MK2 = 79 days, MK3 = 63 days**) spanning three years of data collection (2019-2021 all subjects). In total, I detected 71,373 hippocampal ripple events (**MK1 = 20690, MK2 = 25366, MK3 = 25317**). Ripples had an average frequency of 122.9Hz (SD: +/- 10.37Hz) and average duration of 92.1ms (SD: +/- 41.94ms). Individual events were manually screened and condensed by the time of occurrence of their amplitude center of mass timestamp into a grand total of 11,502 multi-channel ripple events (**MK1 = 3449, MK2 = 3991, MK3 = 4062**). Hippocampal channels were grouped by their manually identified long-axis subdivisions and, as in the rodent, individual ripple events could be identified across all subdivisions of the established long axis (Fig 4.4a-c). While I did observe substantially fewer ripples in the most posterior 30% of the long axis in my recordings, I attribute this to more shallow/improper electrode placement in these locations (Fig 4.4c). Because our detection algorithm necessitated a minimum increase in contiguous amplitude at the sampled timestamp relative to the timestamps that preceded it, for low amplitude LFP signals we likely only sampled the highest-amplitude ripple events at that location. Despite fewer sampled ripples in the posterior third of the long axis, I observed that amplitude remained relatively static as a function of position across the longitudinal axis (Pearson's R = 0.0386, p<0.0001). Similarly, ripple duration (R = 0.0024, p = 0.5237) and frequency (R = 0.1421, p <0.0001) remained relatively constant across the longitudinal axis (Fig 4.4d).

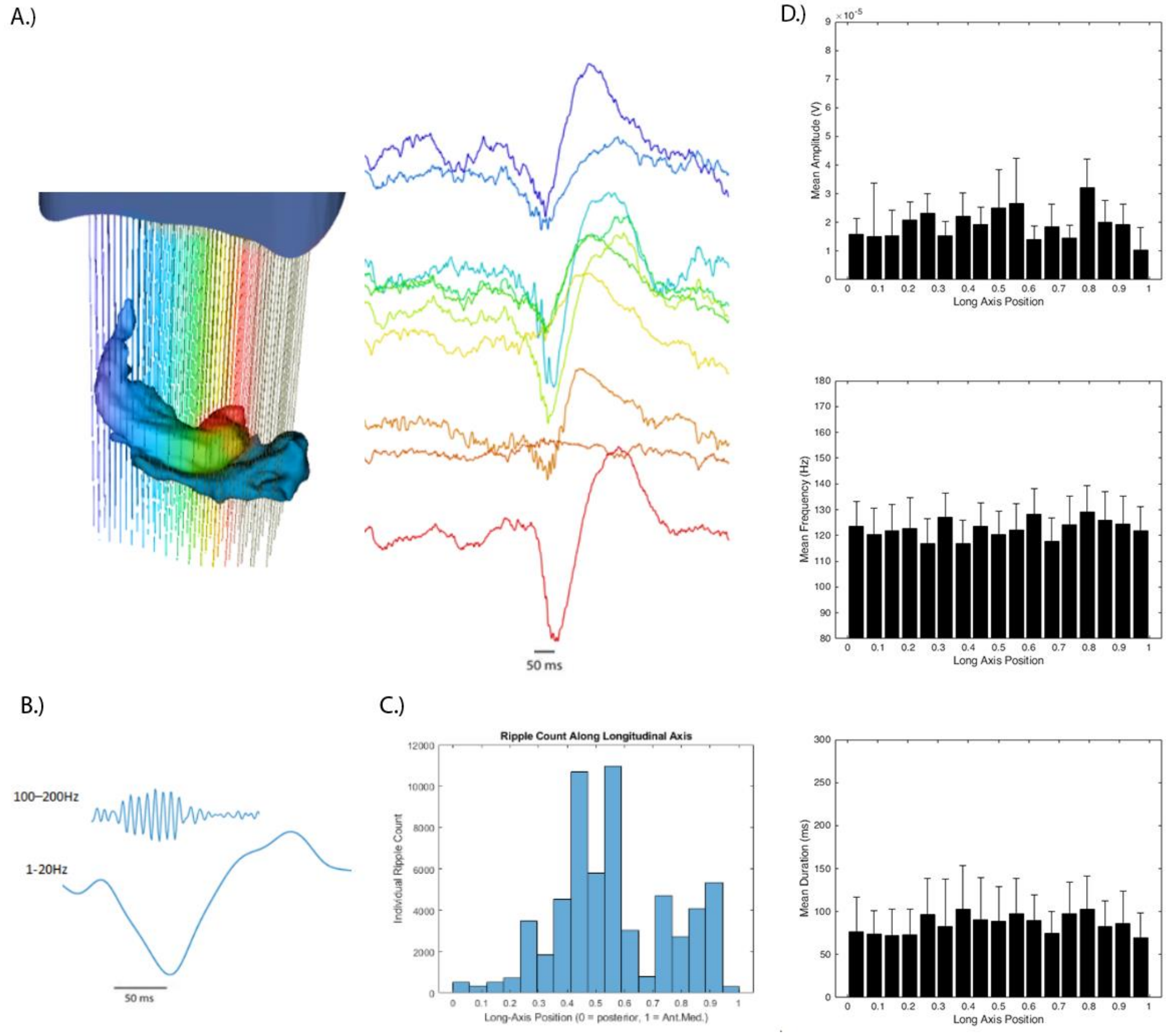

Figure 4.4 Individual Ripples Across the Primate Hippocampus

(A) Color-coded electrode locations along primate hippocampal long axis and example of multi-channel event, color-coded by position. (B) Decomposition of a sharp wave-ripple complex into its high frequency and low frequency component. (C) Identified ripples across the primate hippocampal long axis. (D) Mean amplitude, center of mass frequency, and duration of ripples recorded at each long axis subdivision.

4.3.2 SHARP-WAVE RIPPLES CO-OCCUR ACROSS THE LONGITUDINAL EXTENT OF THE HIPPOCAMPUS

Ripples co-occur in multiple phenotypes across the rodent hippocampus (13). Looking across our multi-channel events, we identified numerous phenotypes of ripple co-occurrence that spanned the entire extent of our sampled primate hippocampal long axis (Fig 4.5). Multichannel events had an average duration of 120ms (+/-SD) These patterns included, but were not limited to, forward-traveling and backwards-traveling events across the long axis (Fig 4.6). However, because we did not homogenously sample across the entirety of the long axis, and because the positioning of our electrodes was not perfectly optimized for ripple identification for every recording session, we focused on addressing whether multi-channel ripple events generated in a particular subdivision of the long axis were spatially biased by their termination locations (i.e. were the locations of the first and last ripple of each multi-channel event spatially biased). As Figure 4.8a shows, we were able to identify multichannel ripple events that spanned nearly all other subdivisions of the hippocampal long axis, regardless of the site of origin. A one-way Kruskal Wallis Test did significant differences between sampled starting locations of multichannel events and their corresponding end locations (df = 16, X^2 =224.09, $p<10^{-38}$). However, a subsequent test for multiple comparisons (MATLAB multcompare.mat, Fig 4.7c) revealed that the identified significant differences largely stemmed from two subdivisions, a posterior subdivision ~3mm/20% along the longitudinal axis with fewer than 100 observations sampled, and an anterior, uncal subdivision roughly 17.6mm/~88%. Further investigation revealed a strong bias in this location to only projections in the proximal 1mm, which is supported by anatomical reports of increased local connectivity in the uncus of the primate hippocampus (20). For the rest of our observations, no significant interactions were observed, suggesting that the patterns of co-occurrence across the primate hippocampal long axis were not independent across our defined subdivisions.

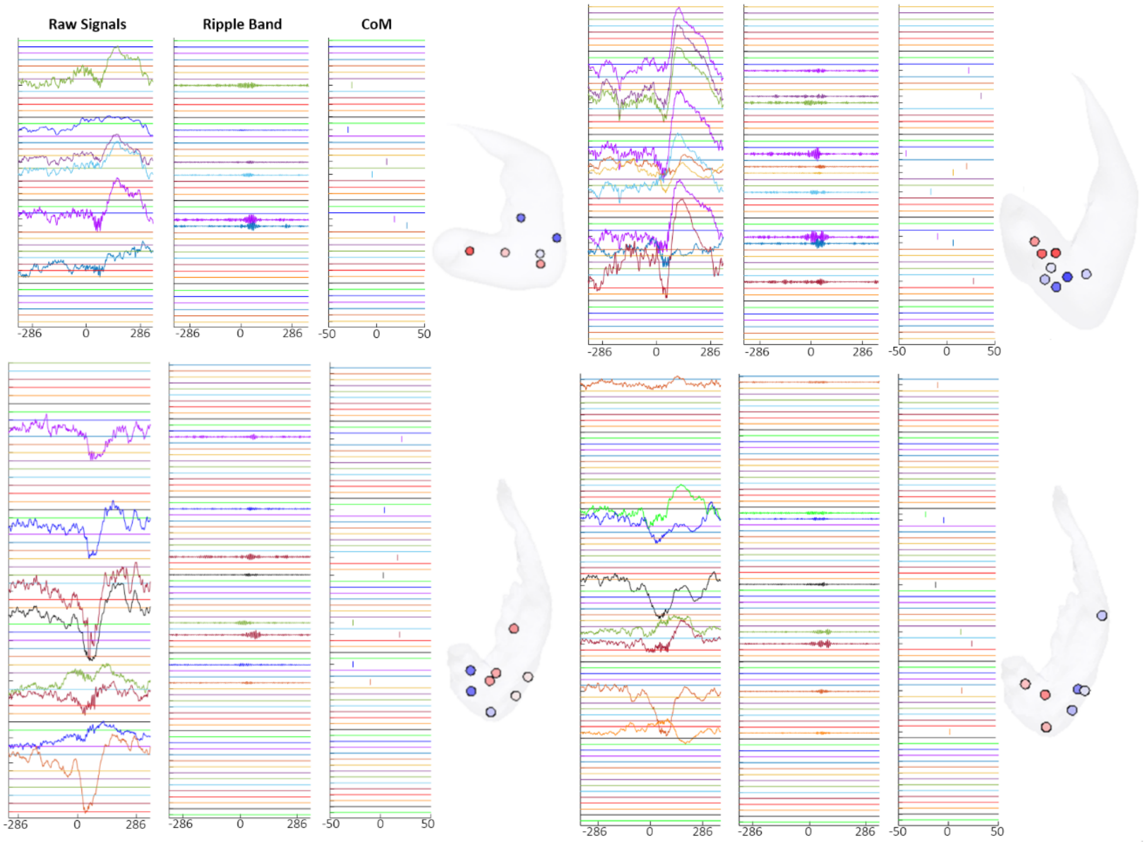

FIGURE 4.5 VARIABILITY OF RIPPLE CO-OCCURRENCE ACROSS THE PRIMATE HIPPOCAMPUS

FOUR EXAMPLES OF MULTICHANNEL RIPPLE EVENTS FROM TWO DIFFERENT ANIMALS. FROM LEFT TO RIGHT, PLOTS SHOW THE RAW LFP SIGNAL OF INDIVIDUAL RIPPLES, RIPPLE BAND-FILTERED TRACES, POINT PROCESSES CORRESPONDING TO THE CENTER OF MASS (COM) OF EACH RIPPLE, AND THEIR TEMPORAL RELATIONSHIP COMBINED WITH THEIR ANATOMICAL LOCATION ON EACH ANIMAL'S HIPPOCAMPUS (GRADIENT: BLUE = -50MS, WHITE = 0MS, RED = +50MS) .

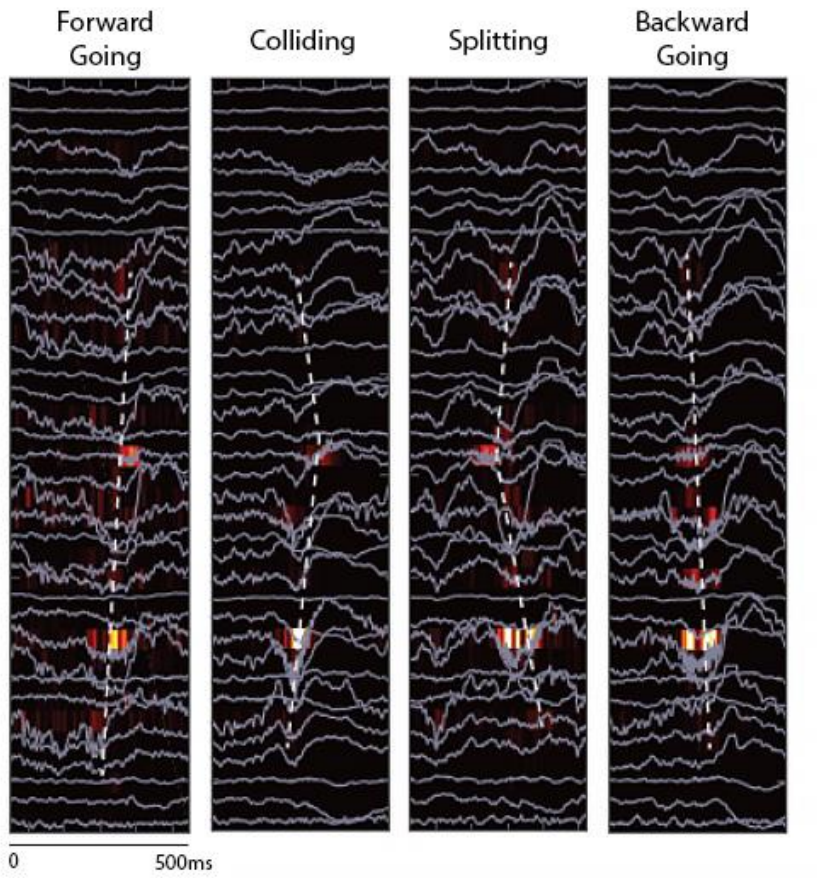

FIGURE 4.6 TRAVELING SHARP WAVE-RIPPLES

TRACES OF LFP SIGNALS ACROSS THE RECORDING ARRAY OF ONE ANIMAL SHOWING THE PRESENCE OF MULTI-DIRECTIONAL TRAVELING WAVES.

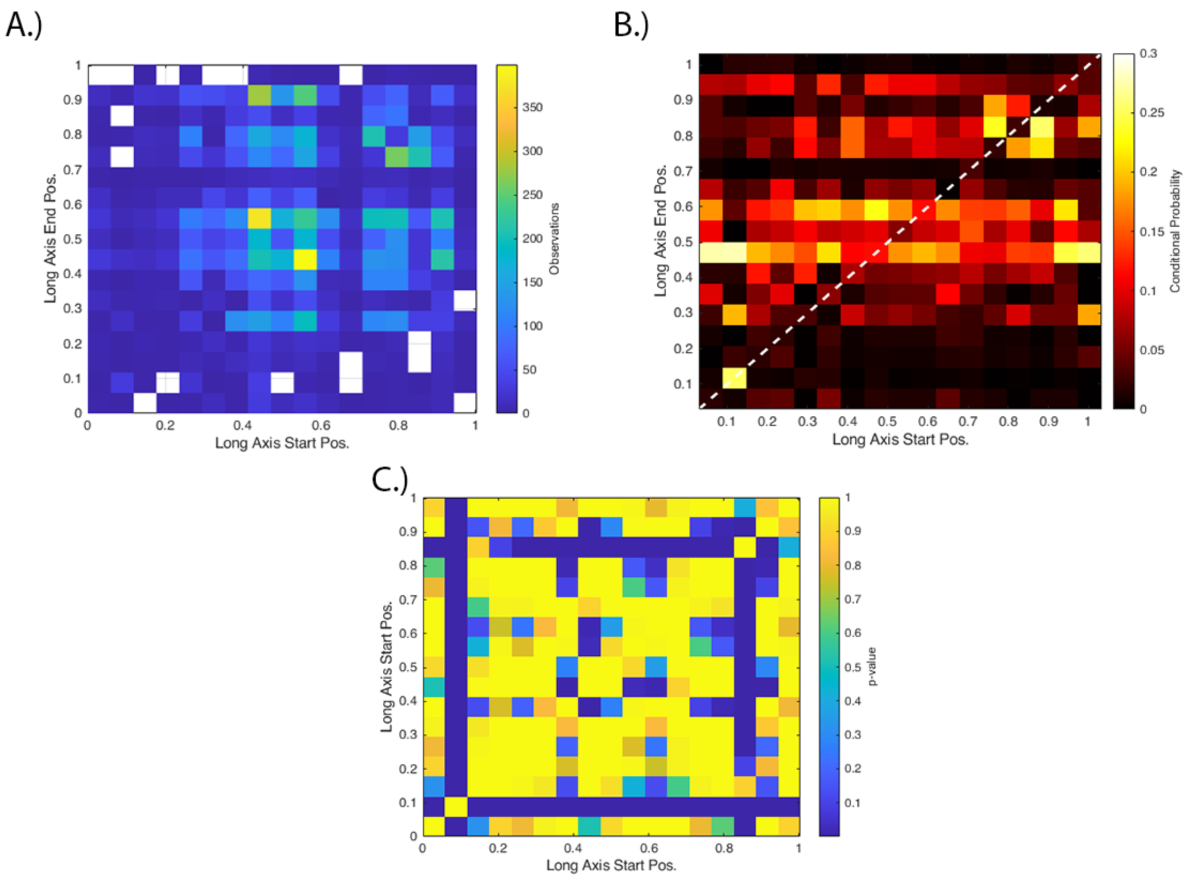

Figure 4.7 Relationships Between Ripple Generation and Termination Sites

(A) Two-dimensional histogram of identified generation and termination sites across the hippocampal long axis. (B) Conditional probability matrix showing the likelihood of terminating at distinct points across the hippocampal long axis independently for each starting position. (C) P-values of pairwise comparisons of multichannel event starting locations' distribution of respective termination locations.

4.3.3 DIRECTIONALITY OF SHARP WAVE RIPPLE TRAVEL

Our observations that multichannel event termination sites largely overlapped regardless of their origin location suggest that, because there is no topography of origin and termination sites, all hippocampal subdivisions can communicate amongst each other. As such, posterior elements can communicate to anterior subdivisions, and vice versa. Thus, the direction of information flow during co-occurring ripple events must flip somewhere across the longitudinal axis. Investigation of our raw data sorted by multichannel event start location (Fig 4.8) revealed that posterior hippocampus predominantly sends information anteriorly, the anterior/uncal hippocampus sends information in the backward direction relative to the longitudinal axis, and the intermediate portion (beginning of the genu, lateral to the fundus of the uncus) engages in bidirectional communication (Fig 4.9b-d). Figures 4.9b & 4.9c emphasize the bidirectional span of multichannel event distances. Importantly, Figure 4.9 reveals that for any particular long axis position, multichannel ripple events elicited from that location are not biased in their travel distances. Despite the overt differences in multichannel ripple event travel direction across the hippocampal long axis, when collapsed across long axis sub-divisions, we observed that 49.2% of our identified multi-channel events traveled in the backward/posterior direction, 43.9% of events traveled forward/anterior/uncal, and only 6.9% of events terminated in the same subdivision as their site of origin (Fig. 4.9a), suggesting no overall bias of the hippocampus in its communication scheme.

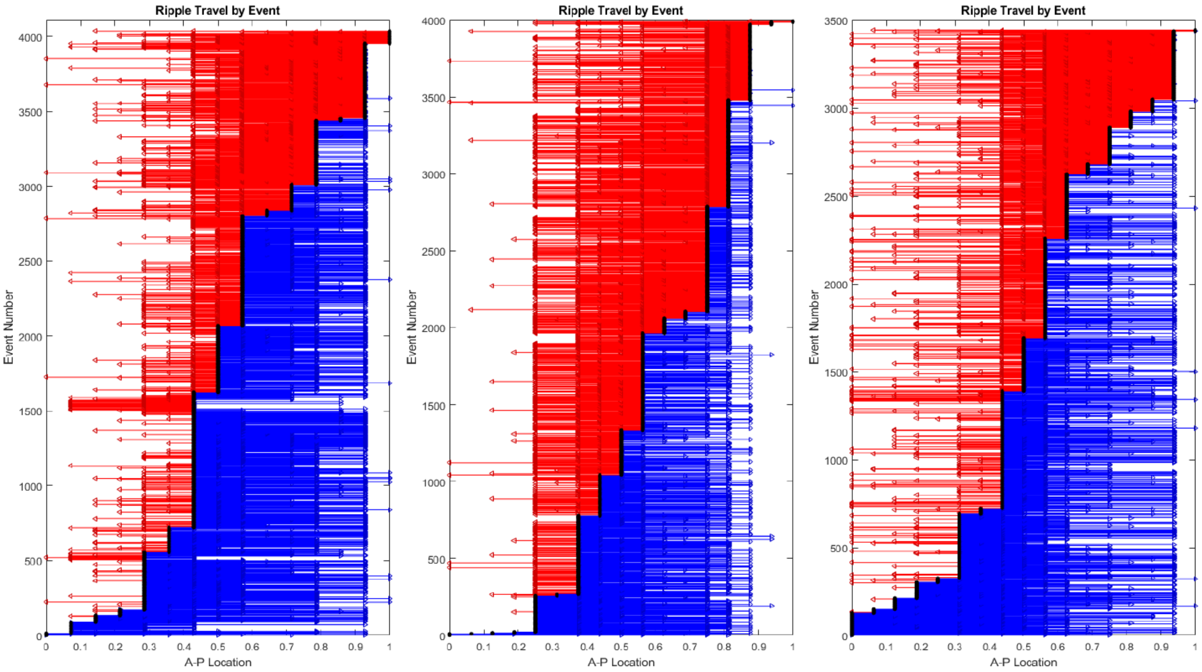

FIGURE 4.8 RIPPLE DIRECTIONALITY PREFERENCES

RAW DIRECTION DATA TAKEN FROM ALL MULTICHANNEL EVENTS FOR ALL THREE SUBJECTS (MK1: LEFT, MK2: MIDDLE, MK3: RIGHT). X-AXIS REPRESENTS THE LONG AXIS START LOCATION FOR EACH MULTI-CHANNEL EVENT, AND Y-AXIS IS EVENT NUMBER. PLOTS ARE SORTED BY THEIR ONSET LOCATION, AND LINES AND ARROWS REFLECT FORWARD TRAVEL (EMPHASIZED BY RED COLORING) OR BACKWARD TRAVEL (EMPHASIZED BY BLUE).

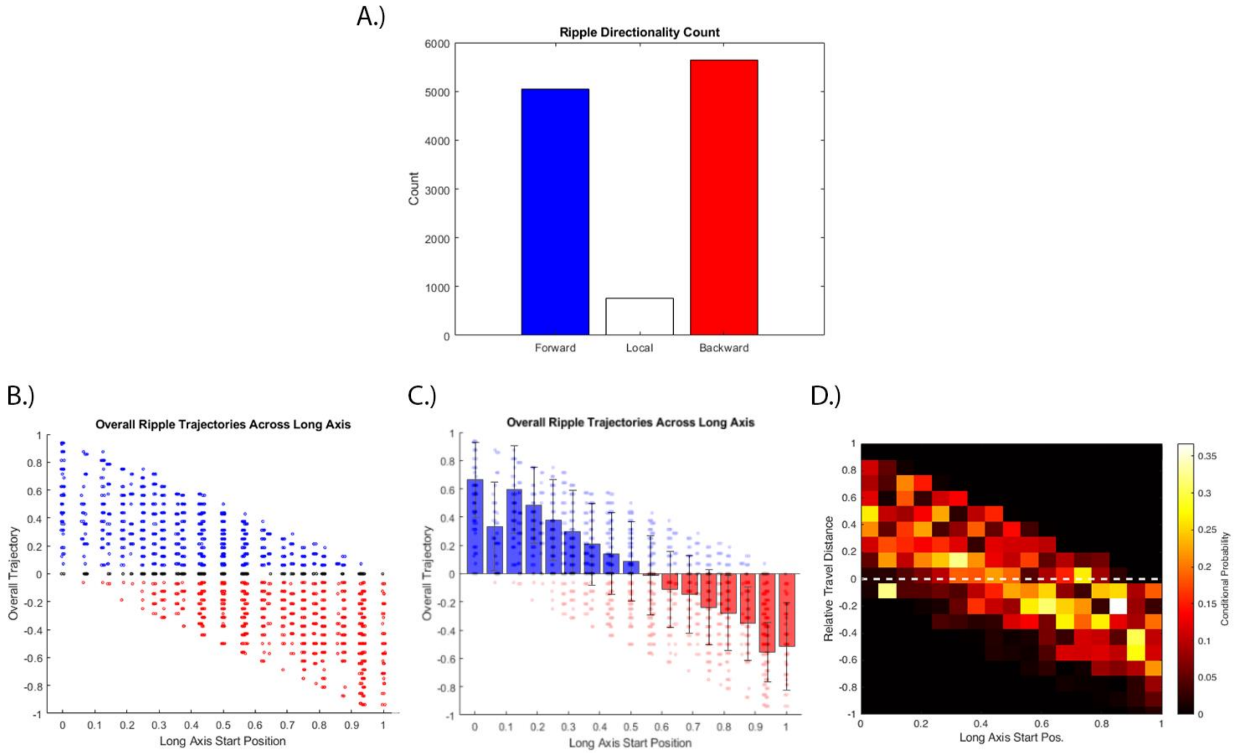

Figure 4.9 Ripple Direction Summaries and Biases

(A) Overall proportions of multichannel events aggregated across all subdivisions and subjects, expressed as total observations (Forward: 5048 events, Local: 792 events, Backward: 5662 events). (B) Scatterplot of individual trajectory lengths across the hippocampal long axis for all subjects. Data artificially jittered for visibility. (C) Mean summaries of (B). (D) Binned Conditional probability highlighting the lack of specific distance traveled for any given long axis start position.

4.4 DISCUSSION

In this chapter, I provide the first evidence suggesting that the primate hippocampus engages in organ-wide communication during quiescent periods. Using putatively detected sharp wave-ripples (SPW-Rs), I show that there is no significant difference in the properties of individual ripples recorded from different locations across the primate hippocampal long axis. Although more ripples were identified in the anterior half of the hippocampus, I did not observe significant differences in the patterns of ripple co-occurrence across our segmented long axis subdivisions. When coupled with the surprising identification of multichannel events in distinct sites within the uncus that were spatially limited, this finding supports the hypothesis that changing drive from intrinsic circuitry induces ripple co-occurrence. The intrinsic connectivity of the primate has previously been shown to be a diffuse gradient of termination patterns that spans multiple distances and can even reach from one end of the hippocampus to the other in both directions (20). By contrast, afferents from entorhinal cortex are limited both by their topographic reach to the hippocampal long axis as well as entorhinal's own limited intrinsic circuitry (See Chapter 2). This is in stark contrast to the rodent, whose intrinsic hippocampal connectivity and input from entorhinal both elicit much more punctate termination sites that separate along the intermediate boundaries of dorsal and ventral hippocampus (14). Nevertheless, when we combine our novel results from previous studies in the rodent, our data strongly suggest that ripple events are generated by exogenous drive from both subiculum (20) and entorhinal cortex (21) but sustained predominantly by intrinsic connectivity before being sent back out to cortex through the above structures via recurrent connectivity.

4.4.1 IMPLICATIONS OF BI-DIRECTIONAL RIPPLE CO-OCCURRENCE ON BROADER COMMUNICATION AND CONSOLIDATION

In addition to co-occurrence spanning all putatively defined subdivisions of the monkey hippocampal long axis, we observed the presence of traveling waves across and an overall drift in direction flow moving across the structure, which we describe as a natural consequence of bidirectional span of co-occurrence. However, these results have strong implications for how we as a field think about the association between hippocampal-cortical communication during consolidation periods. SPW-Rs are strongly correlated with cortical slow waves (recorded predominantly from cortex) (22-24), and our models of memory consolidation link ripple activity and the replay of temporally linked neuronal firing to subsequent cortical activations (25). However, these models do not consider how ripples as a hippocampus-wide event may recruit large and distinct portions of cortex, which can in turn excite and inhibit adjacent regions via lateral connections (26). Given our findings and the topographic afferent and efferent connectivity of entorhinal cortex in primates (Ch. 2), we can theorize that the primate hippocampus is able to activate multiple, distinct portions of cortex in a species-specific way that changes as a function of the spatial distribution of ripple co-occurrence. Taken to its logical extreme, our finding of traveling ripple waves in the primate hippocampus during quiescent rest periods provides a potential mechanism by which propagating SPW-R activity can induce cortex-wide traveling activity. However, this is purely speculative, and future experiments should focus on disrupting or artificially inducing ripples in the primate hippocampus to determine the effects on both intrinsic travel and subsequent cortical activity.

4.4.2 LIMITATIONS OF THIS STUDY AND FUTURE DIRECTIONS

A major innovation in this chapter is the deployment of a novel ripple detection algorithm that utilizes changes in amplitude over time, as opposed to normalized and binned amplitude, to detect ripples on channels with low overall amplitude. This algorithm was partly designed to overcome the limitation that our independently movable electrodes were not always at the optimal depth for prominent SPW-R detection. We were ultimately pleased by the performance of the algorithm's threshold on ripple detection across our recordings. However, it cannot be dismissed that the hard threshold value of the 99.5th percentile of amplitude change may inadvertently lead to excluding low-magnitude ripples in signals with a wide variety of ripple amplitudes. This may partially explain the post-hoc observation that we detected far fewer ripples in the posterior hippocampus. However, to remain consistent with ripple detection on other channels and to avoid the introduction of spurious single-channel noise in our multi-channel events, this threshold was not adjusted independently. Future modifications of this algorithm can employ template matching across identified candidate ripples to help define an appropriate feature space for single-channel inclusion and exclusion.

In addition to co-occurring with cortical slow waves, one of the hallmarks of sharp wave-ripples is their relationship to hippocampal single-unit activity (SUA). Specifically, SUA has been shown to co-occur during ripple events in both rodents (8) and monkeys (12, 27). Moreover, in rodents the pattern of simultaneously active neurons mimics the temporal firing patterns observed during active exploration (8). Although our recordings and hyperdrive were optimized for spatial coverage, the single electrodes that we recorded from makes isolating putative single units from broader multi-unit activity and noise non-trivial and impossible to perform confidently. Future work using tetrode recordings (12, 27) or high-density multi-contact probes, such as the Neuropixels probes, in a spatially distributed hyperdrive will allow for triangulation of individual units and more dense simultaneous collection.

Ultimately, the findings presented in this chapter provide the first evidence for a hallmark of organ-wide communication within the primate hippocampus. I show that ripples can occur anywhere across the full extent of the structure, which is distinct from the dual patterns of independent ripple generation in rodents. Furthermore, the bidirectional co-occurrence of ripples across the primate longitudinal axis provides support for a mechanism of temporal organization of cortical activity by propagating hippocampal SPW-Rs. These findings have strong implications for global mechanisms of memory consolidation, and they specifically provide evidence for why non-human primates make a better translational model to understanding biophysical mechanisms of memory in humans. Future work should leverage manipulations of the hippocampus during dual hippocampal-cortical recordings, as well as dense, multi-contact recordings, to identify the influence of various traveling patterns (or lack thereof) on local single unit firing patterns and broader cortical slow waves.

4.5 ACKNOWLEDGMENTS:

Aaron D. Garcia, Jon W. Rueckemann, Autumn J. Mallory, Yoni I. Browning, Elizabeth A. Buffalo

CHAPTER 5 || NOVEL TECHNIQUES FOR IMPROVING DETECTION AND CHARACTERIZATION OF NON-STATIONARY NETWORK OSCILLATIONS

5.1 INTRODUCTION

In depth EEG recordings, the local field potential (LFP) is a continuous measure of mesoscopic neural synchrony. This signal represents changes in the extracellular milieu that arise from fluctuations in ion concentrations caused by post-synaptic potentials (PSPs) received from brain areas upstream of the recording location. When PSPs are received by a large population simultaneously, these fluctuations produce highly synchronous network states that can provide transient periods of disinhibition, excitation, and inhibition depending on the types of neurons in the stimulated population (1). These transient states are often seen in the LFP record as oscillations. Thus, oscillatory activity in the LFP reflects circuit level dynamics of communication between brain areas. Moreover, the LFP provides a clear and accessible readout of the potential range of coherent dynamics a neural network may fall into because of changing cognitive (2), behavioral (3), or conscious states (4).

In the field of rodent hippocampal physiology, LFP recordings have critically informed our understanding of how the hippocampus functions in service of proper learning and memory function. For example, seminal investigations by Case Vanderwolf and colleagues identified a prominent oscillation in the ~6-12Hz band that dominated the recorded signals as animals engaged in active, goal-oriented behaviors (reviewed in detail in 6). This oscillation was found to be highly stationary (i.e., sinusoidal and at a consistent frequency), was sustained for the duration of observed behaviors, and had a strong co-occurrence with faster gamma oscillations (~30-90Hz) (6,8). These oscillations correlated with olfactory exploratory behaviors and the rate at which rats explored their environment (9). In subsequent studies, both oscillations were shown to organize the sequential firing of hippocampal neurons during acquisition and retrieval of memories (6, 7, 8). Moreover, disrupting the upstream generators of the theta rhythm was discovered to severely impair memory performance and influence the information content of the individual hippocampal neurons, thus showing a causal link between LFP phenomena and proper memory processing (10).

LFP features in the primate hippocampus are largely homogenous with those identified in rodent. Theta-range oscillations (3-12Hz) are observed in the hippocampus as monkeys perform various behaviors, and the presence and frequency of these oscillations correlates with the monkeys' visual exploratory behaviors (11,12). However, rather than spanning the entirety of a particular behavioral epoch, oscillations in this band are brief and occur in sporadic bouts (11,12). These observed differences might be explained by more elaborate cognitive capacity in primates. Recent studies of single unit activity from our lab (13) and others (14) suggest the presence of cells that map complex task phases and task rules rather than simple place or time information. It warrants consideration that the organizing LFP states may also change in a way that reflects these more diverse neuronal dynamics elicited by increased cognitive demands. This could potentially be reflected in oscillatory phenomena that change dramatically in frequency and structure, which unfortunately would make these signals unsuitable for many of the traditional methods of frequency-based analyses. Additionally, sparse sampling in acute recordings means that disambiguating neurogenic signal from volume conducted noise becomes non-trivial. Volume conducted artifacts are obstructive epiphenomenon that obfuscate neuronal LFP signals and arise from many sources include chewing, breathing, animal movement, large potentials from distant brain regions, etc (17). Online filtering of data might mitigate some of the sources of noise, but reliable offline methods of artifact removal are needed to confirm that observed phenomena are generated by the brain area of interest rather than external sources.

In this chapter, we present two novel and easily accessible methods to mitigate volume conducted noise and characterize sporadic features of neural time series data, respectively. We demonstrate with simulated data and LFP recordings recording chronically implanted hyperdrives (Chapter 4) that using the singular value decomposition (SVD) of the signals allows for computing a common-source average (CSA) that scales with the magnitude of each electrode. We illuminate the degree of contamination caused by volume conducted artifact and improved detection of neurogenic signals after removal. Additionally, we implement a novel method of summarizing time-frequency power information termed the spectral "landscape", which can visualize the frequency-specific variance of energy in LFP signal across a recording session. We apply these spectral landscapes to our simulations and high-density recordings, and in conjunction with anatomical localization of our chronically placed electrodes, provide some of the first preliminary depictions of task-specific LFP signatures in various subregions of the monkey hippocampal formation.

5.2 COMMON SOURCE ARTIFACT REMOVAL WITH SINGULAR VALUE DECOMPOSITION

5.2.1 SINGULAR VALUE DECOMPOSITION EXPLAINED

The SVD is a matrix factorization method that can be applied to any real or complex matrix, regardless of size. This generalizes from the canonical eigendecomposition, which can only function on a square (*m-by-m*) matrix. In the case of a given *m-by-n* data matrix **M**, the SVD can be represented as:

$$\boldsymbol{M} = \boldsymbol{U}\sum\boldsymbol{V'} \qquad \textbf{(eq. 5.1)}$$

where **U** and **V** are orthonormal unitary matrices in the m and n dimensions, respectively, and $\sum$ is an *m-by-n* diagonal matrix whose diagonal, non-negative elements are ordered by descending value (Illustrated in Figure 5.1) (18). These diagonal elements are called singular values. Whereas U and V can be seen as rotations, the singular values in $\sum$ can be interpreted as stretch factors along each of the rotation directions. The total value of non-zero singular values is equal to min(m,n). Thinking about the SVD as a generalized method of eigendecomposition, we can interpret the columns of U and V as two ortho-normal sets of eigenvectors such that columns of U are eigenvectors of the m-by-m matrix MM* and columns of V represent eigenvectors for the n-by-n matrix A*A. Singular values can be explained as eigenvalues for both series of eigenvectors (specifically in form $\sum^2$).

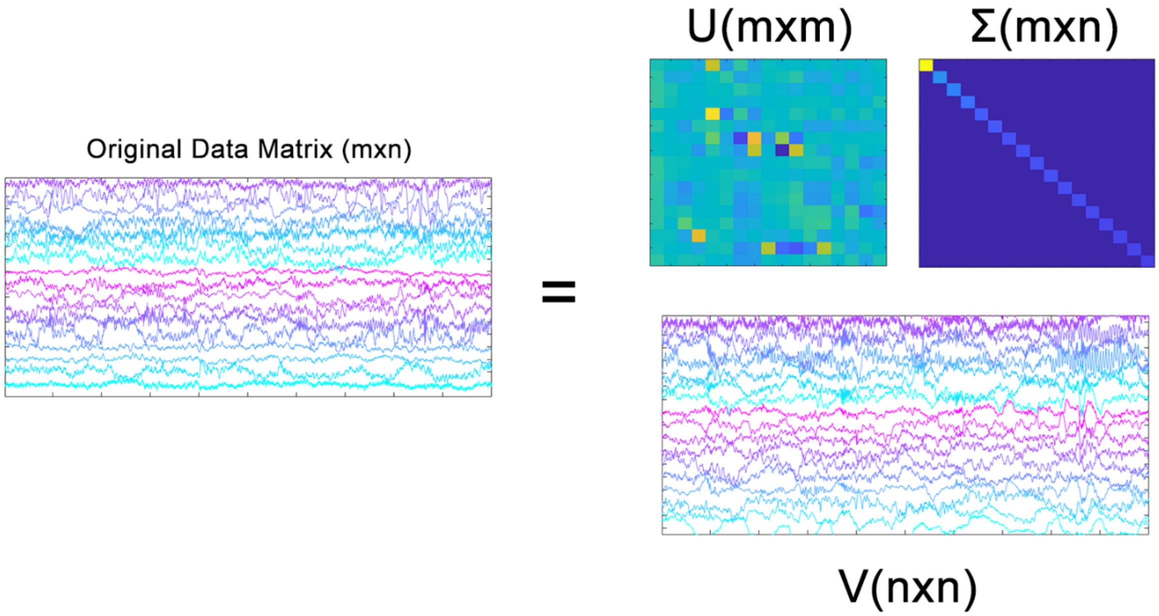

Figure 5.1: Singular Value Decomposition Illustration

The original data matrix of size MxN can be decomposed into the three matrices, U (size: MxM), ∑ (size:MxN), and V(size:NxN). These three matrices can be combined using equation 5.1 to reproduce the original matrix. (Note: Only the first M modes are shown in ∑ and V for clarity.)

5.2.2 EXTRACTING SHARED SIGNALS FROM SVD

Because the SVD provides orthogonal basis sets ordered by explained variance and generated by the original data matrices, this method is especially useful for directly identifying trends in multivariate data sets. For instance, let the m-by-n matrix M be a neural recording of length m across a grid of electrodes with n contacts. In this case, columns of U provide the dominant patterns of co-variability across the recording array (or shared signal across the electrodes), and corresponding columns of V represent the amplitude scaling or loading of these patterns along each electrode. To generate various modes of activity scaled by their presence across electrodes, we thus simplified equation 5.1 into the following format for any mode *k*:

$$\boldsymbol{M_k = u_k \sigma_k v_k} \qquad \textbf{(eq. 5.2)}.$$

The resulting mode M_k is a matrix of identical signals (u_k) that are scaled by explained system variance by mode k (σ_k) and individual loadings from amplitude variation across electrodes (v_k). The individual SVD modes can reflect the underlying dimensionality of a particular dataset. For example, in the hypothetical dataset shown in Figure 5.2, we have three different oscillatory patterns built upon low amplitude noise and spread across an array of 64 channels. Identifying the three dominant trends may not readily apparent by just visual observation of the signals. However, performing SVD and investigating the singular value spectrum ($\sum$) of the dataset reveals that ~100% of the variance can be explained by the first three modes. Because ($m<n$) in this case, the first three columns of U tell us the relative magnitude of the presence of each identified mode on each channel, and the first three columns of V highlight the dynamics over time for each mode. If our data matrix was transposed, the applicable interpretations of U and V would be reversed such that U would explain the amplitude loadings and V would explain the temporal dynamics. Backprojecting each of the first three modes into our data space using equation 5.2 shows which patterns are prominently expressed on different electrodes for express classification. Moreover, we can add our 3

modes together to produce a denoised matrix that keeps only the variance-explaining signals or combine only a subset of the modes if we wanted to ignore one (or more) of the dynamics in the dataset.

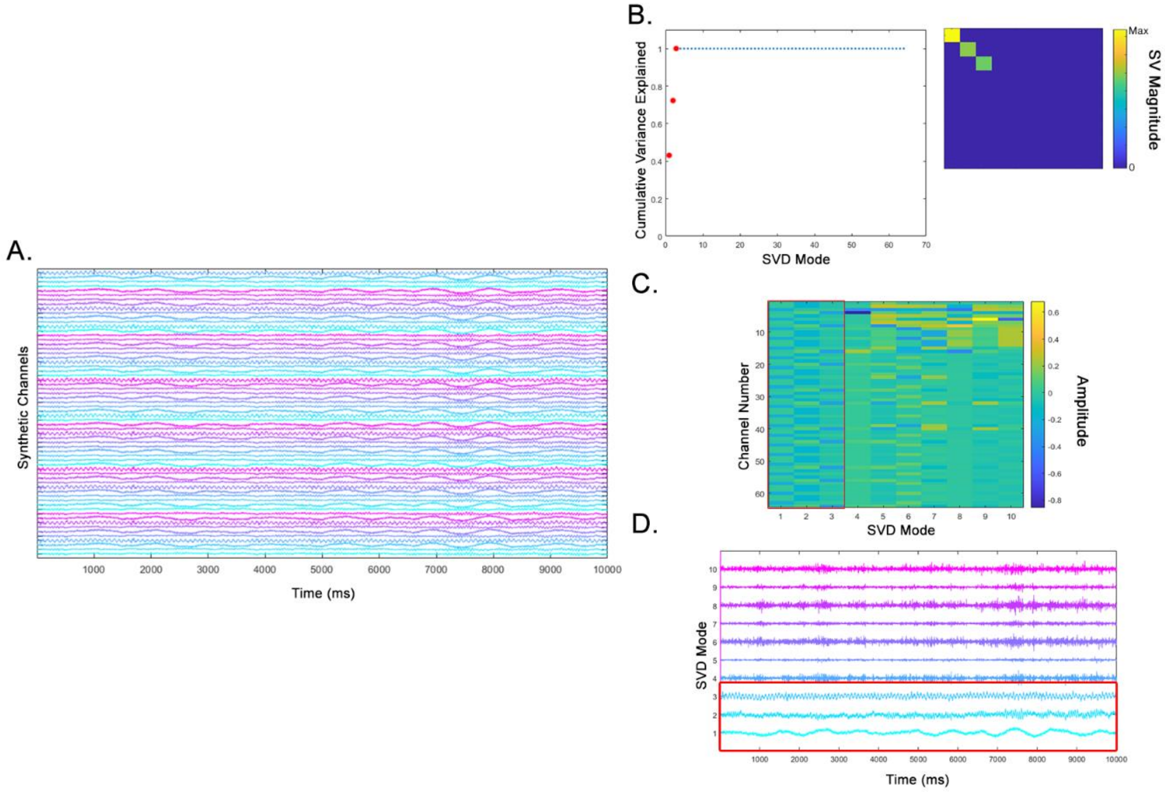

Figure 5.2 SVD of Synthetic 3-Mode Dataset

(A) Synthetic signal array (64 channel-by-10000ms). (B) Variance explained by singular values and singular value spectrum of (A). (C) V matrix showing relative loadings across channels from (A). (D) U Matrix showing temporal dynamics of SVD modes. Red bounding boxes outline the three modes which explain ~100% of the variance

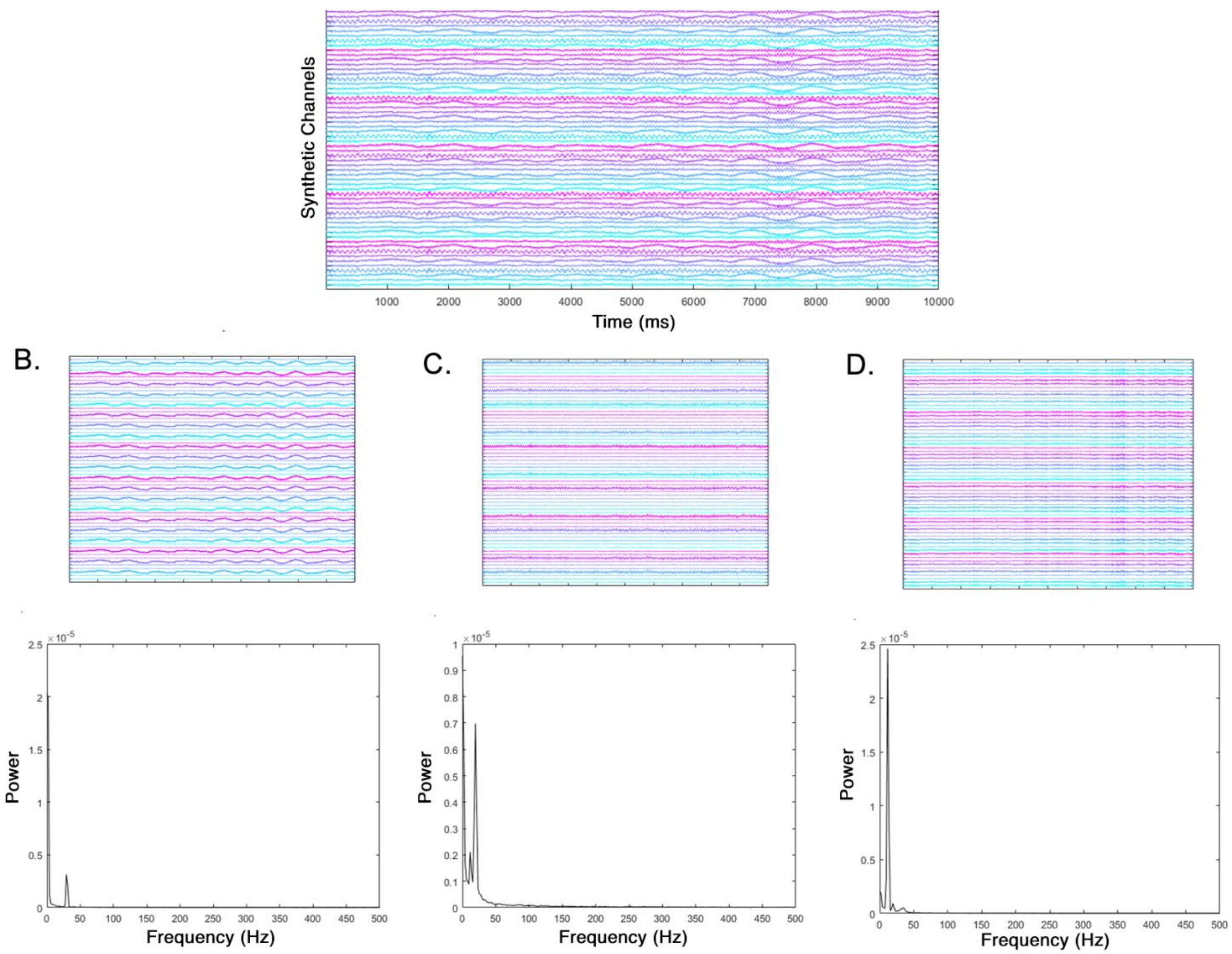

Figure 5.3 Reconstruction of underlying signal phenotypes with SVD

(A) Original Signal Matrix. (B) Reconstruction of first mode (1Hz constant oscillation + 35Hz Bursts). (C) Reconstruction of Second Mode (12Hz + 25Hz constant oscillations). (D) Reconstruction of third mode (12Hz Constant Oscillation + 35Hz Bursts).

5.2.3 REMOVING VOLUME CONDUCTION FROM SYNTHETIC SIGNALS

While SVD is useful for identifying inherent patterns of a given dataset, there are cases—as we will show in subsequent sections with our data— in which synchronous noise across a recording array prevents the singular value spectrum from accurately reflecting the true dimensionality of a given system. This is especially true when the scale of the noise is significantly larger than that of the underlying signals. For example, adding synchronous large amplitude, low-frequency noise to the three-mode set of signals described in section 5.2.2 and investigating the singular value spectrum reveals that one mode dominates the explained variance. In this case, the various modes produced by SVD no longer resemble those from figure 5.2. Because SVD is biased towards the largest trends across the data, this may seem like a limitation of the decomposition to capture all meaningful dynamics when one dominates. However, we can utilize the SVD output and the first SVD mode to eliminate this synchronous noise, which we designed to be analogous to volume conducted noise observed in our neural signals. As described in the previous section, we can reconstruct the first SVD mode (Figure 5.4). Subtracting this mode from our initial data matrix now leaves us with our original set of signals from section 5.2.2. Further investigation of the first SVD mode highlights a striking resemblance to the common-source average taken across all our signals (Mean Squared Error (MSE): $7.8e^{-11}$) (Figure 5.5).

For low-dimensional datasets, noise must be drastically larger compared to the underlying signals for the SVD to accurately capture the noise without producing multiple, contaminated modes. In our simulations, the amplitude of the noise injected into our data had to be ~11-fold larger than the signal amplitude for a single mode to explain >99% of the system variance (Figure 5.6). However, a strong resemblance to the common-source average (Mean squared error: ~0) was observed when the amplitude of noise was only twice as large as the underlying signal and the first SVD mode contained ~70% of the explained variance. As dimensionality/asynchrony within the data set increases, the magnitude of synchronous noise becomes less of an influence on overall SVD output. In the simple case of a synthetic, 64-channel dataset with a traveling 20 Hz wave, synchronous wideband pink noise present on all channels is easily detectable by SVD, even though its amplitude scaling is 1:1 with our traveling wave (Figure 5.7A). As Figure 5.7 shows, reconstructing the first mode and subtracting it from our data leaves us with a faithful reproduction of the non-noised traveling wave matrix (cross-channel mean MSE: $2.27e^{-5}$). Thus, SVD is an efficient method of identifying patterns of synchrony across all datasets, and this method becomes increasingly better at identifying coherent artifacts at lower amplitudes as the inherent dimensionality of the data under study increases.

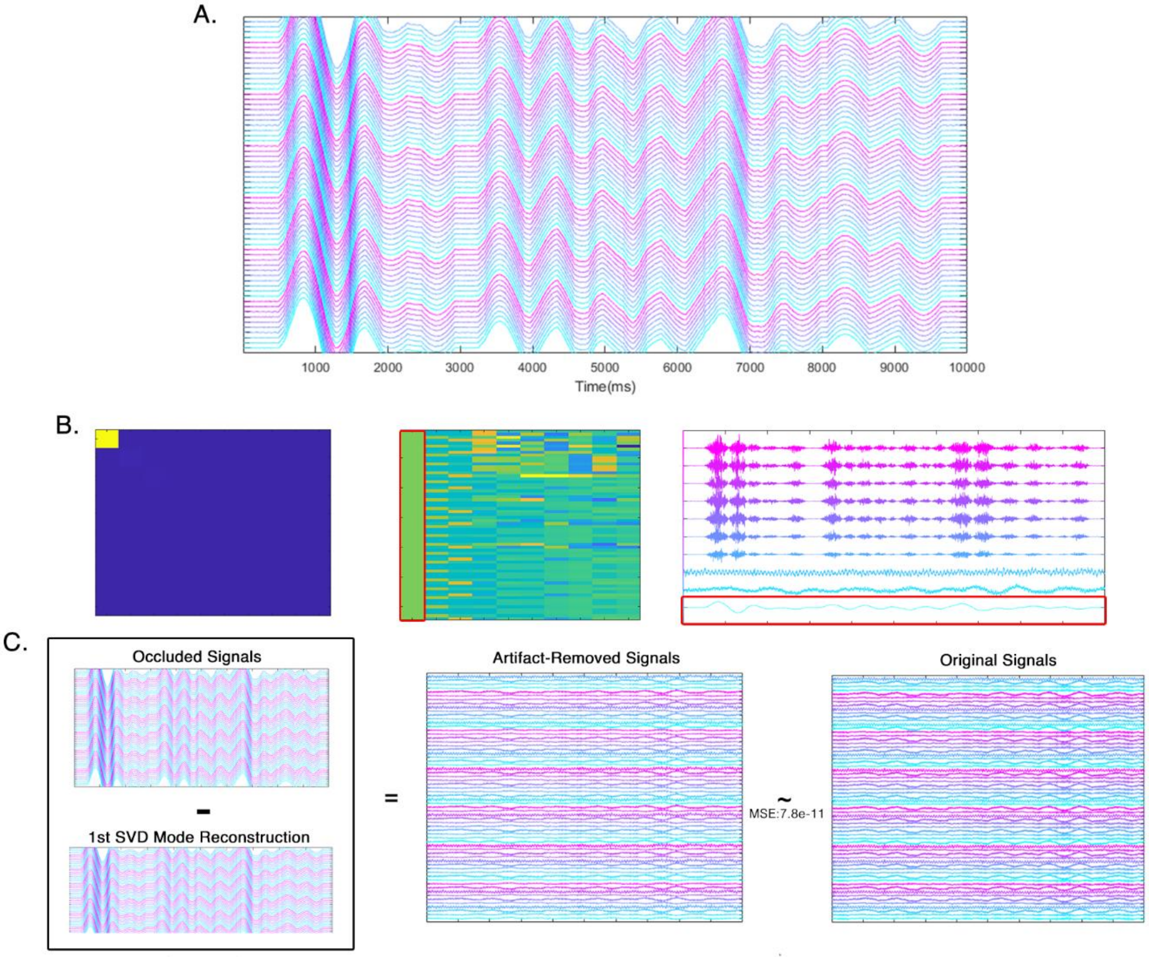

Figure 5.4 Removal of artifact with SVD

(A) The same data shown in Figure 5.3 Occluded by large, low-frequency artifact. (B). The SVD output from (A) reveals a singular dominant trend across all channels. (C) Subtracting the first mode from all electrodes produces a faithful reproduction of the original dataset from Figure 5.3.

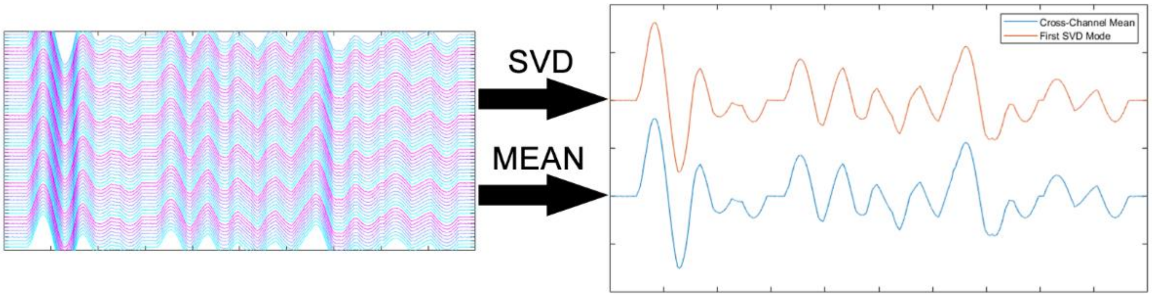

Figure 5.5: Comparison of Common-Source average and first SVD mode.

(Mean Squared Error: 7.8e^{-11})

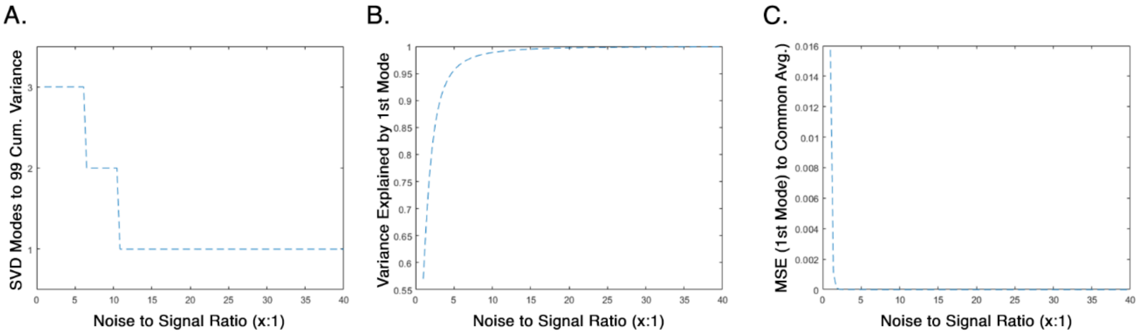

Figure 5.6 Influence of relative noise magnitude on dimensionality

(A) Number of SVD modes needed to explain 99% data variance at various amplitude scalings of low frequency noise. (B) Fraction of total variance explained by first SVD mode at various amplitude scalings of noise. (C) Mean Squared Error of common-source average to the first SVD mode at different amplitude scalings.

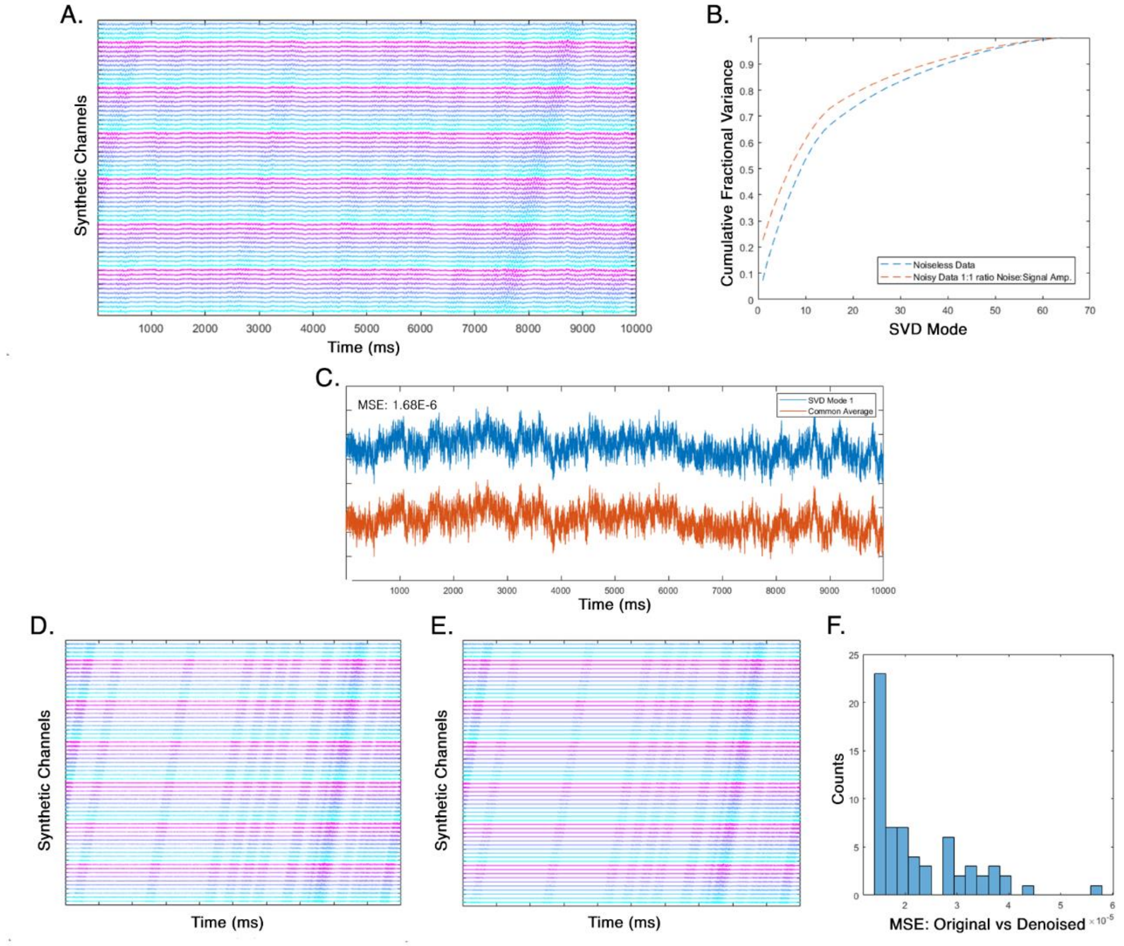

Figure 5.7: SVD-CSA Removal on high-dimensional data

(A) An intermittent traveling 20Hz wave spread across 64 channels with pink noise underneath (Amplitude scaling = 1:1 Noise:Signal). (B) Variance explained by singular values in noiseless data and data in (A). (C) Comparison of first SVD mode and common-source average (MSE: 1.68E^{-6}). (D) Reconstruction of signals after artifact subtraction. (E) Original noiseless data. (F) MSE comparison of noiseless data and artifact removed data (mean MSE: 2.27E^{-5}).

5.2.4 SVD REVEALS AND MITIGATES VOLUME CONDUCTED NOISE IN HIGH-DENSITY NEURAL RECORDINGS

To assess the efficacy of SVD-CSA removal on real neural signals, we analyzed neural recordings from primates that were collected from chronically implanted, 124-channel microdrives (Gray Matter Research, Inc). Manual inspection and cross-correlation of the signals revealed high amplitude, low frequency, synchronous potentials across most channels in the array (Figure 5.8A&B). Investigating the singular value spectrum for these recordings revealed a dominant trend by which many sessions had >70% variance explainable by one mode (Figure 5.8 C). Because these data are several hours long and the electrodes are in various brain regions, we expected the inherent dimensionality of the recording matrix to be higher. We generated the first mode of the SVD and subtracted it from our signals as described in section 5.2.3 (Figure 5.9A). This subtraction led to much less coherence across the entire recording array and increased dimensionality on the LFP signal matrix after re-running and examining the singular values after artifact removal (Figure 5.9B).

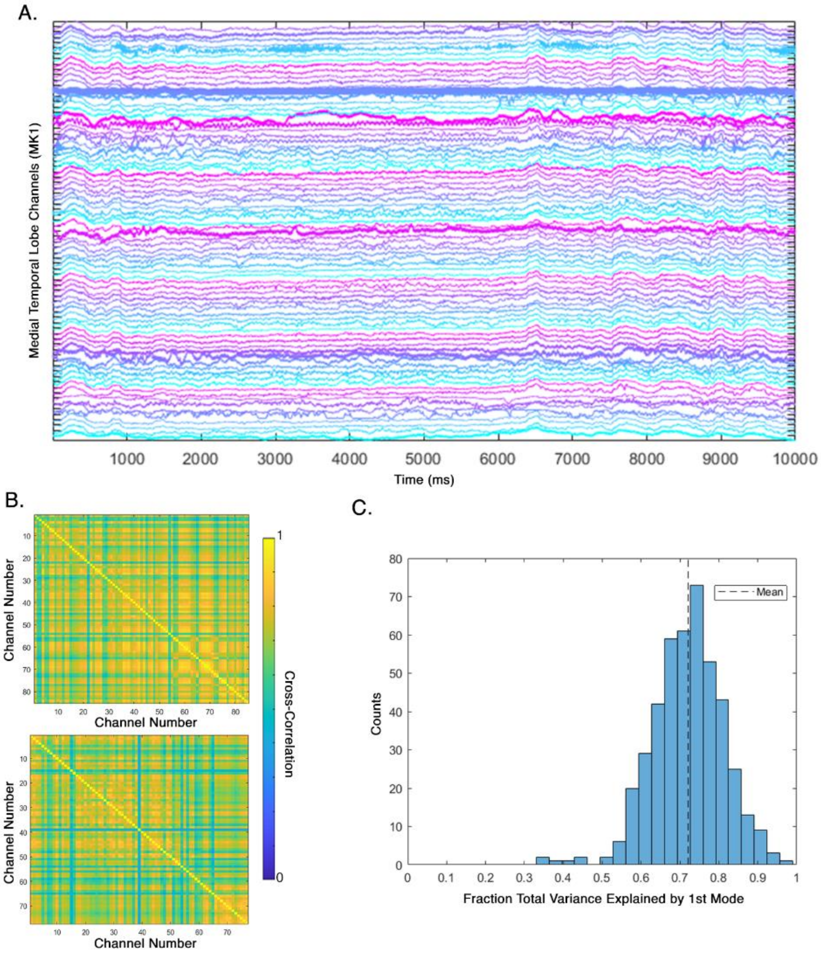

Figure 5.8 Neural recordings occluded by noise

(A) Ten second example from one animal (MK1) of recorded signals targeting the medial temporal lobe (MTL) in which large, low frequency artifacts are present across all channels. (B) Average Correlation matrices of MTL channels for MK2 (Top; n = 195 recordings) and MK1 (Bottom; N = 250 recordings). (C) Histogram of fraction of total variance explained by the first mode for many sessions across both animals (mean = 0.7208; n=445 recordings).

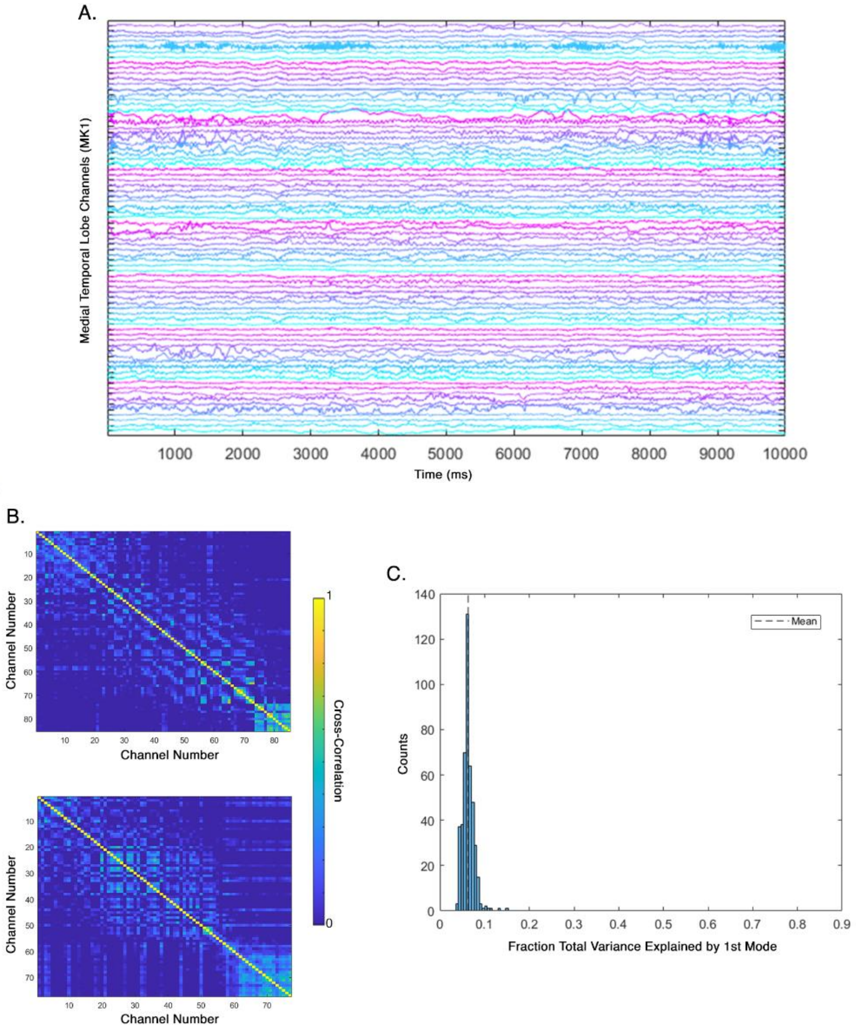

Figure 5.9 Neural Recordings After Cleaning

(A) Example neural signals from MK1 after SVD-CSA removal. (B) Average Correlation matrices of MTL channels after denoising for MK2 (Top; n = 195 recordings) and MK1 (Bottom; N = 250 recordings). (C) Histogram of fraction of total variance explained by the first mode for many sessions across both animals after cleaning (mean = 0.0629; n=445 recordings).

5.3 TRACKING OSCILLATORY VARIABILITY OVER TIME WITH SPECTRAL LANDSCAPES

5.3.1 SPECTRAL LANDSCAPE CONSTRUCTION

"Spectral landscapes" of time-series data are a dimension-reduced version of wavelet spectrograms, which are created by convolving signals with a series of complex Morlet wavelets (CMW). From (19), these wavelets take the form:

$$\boldsymbol{CMW = e^{g}e^{i2\pi ft}} \qquad \textbf{(eq. 5.3)}$$

$$\boldsymbol{g = -t^{2}/2s^{2}} \qquad \textbf{(eq.5.4)}$$

In eq. 2.3, e^{g} represents a gaussian window of length s. This window is multiplied by $e^{i2\pi ft}$, which is a complex sine wave with band-specific peak frequency (f). The number of cycles in the wavelet is determined by s. For subsequent analysis, we created a family of 60 logarithmically spaced CMWs with peak frequencies ranging from 1Hz-100Hz and cycle length also logarithmically increasing from 3-10 cycles. The band-specific increase in number of cycles was included to avoid spurious power in higher frequency bands. Bandlimited amplitude for each frequency was calculated by convolving signals with each CMW and taking the absolute value of the resulting complex time series. Bandlimited power was calculated as the square of the absolute value. Wavelet spectrograms are the resulting frequency-by-time matrix (size: 60-by-t). We calculated power spectral density (PSD) estimates from the spectrogram by obtaining the median power for each frequency across all time points (60-by-1). To get a sense of power variation across time, we then calculated the 5th, 25th, 75th, and 95th percentiles across time for each frequency. Each of these four percentile lines, in addition to the median PSD, defines the basis for our spectral landscapes (Figure 5.10).

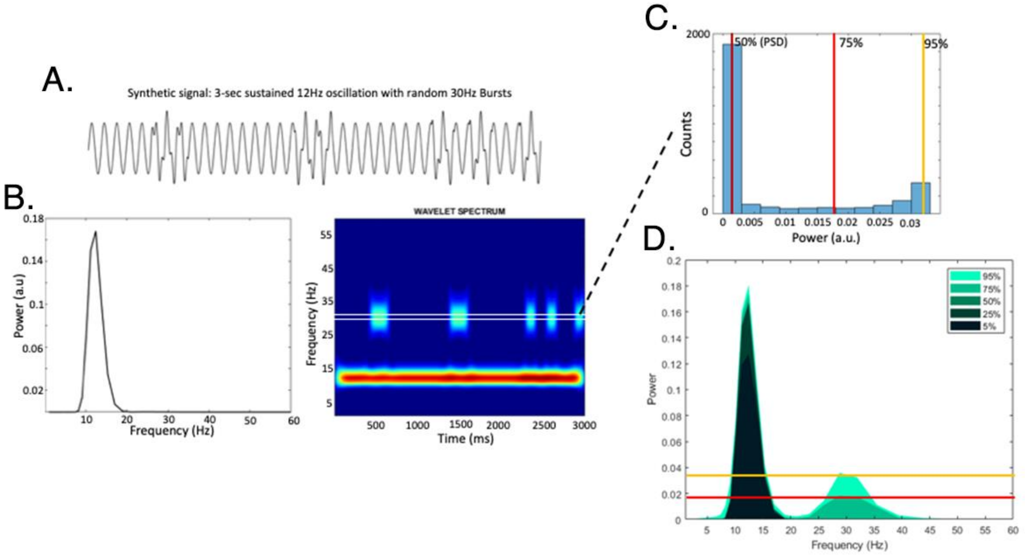

FIGURE 5.10 CONSTRUCTION OF SPECTRAL LANDSCAPES

(A) A 3-SECOND SIGNAL CONTAINING A 12 HZ SUSTAINED OSCILLATION AND SPURIOUS BURSTS OF 30HZ SIGNAL. (B) BOTH THE WAVELET PSD AND WAVELET SPECTROGRAM IDENTIFY POWER IN THE 12HZ BAND, HOWEVER THE PSD FAILS TO RECOGNIZE SUFFICIENT POWER IN THE 30HZ BAND. (C) AGGREGATING DATA OVER TIME IN HISTOGRAM FORMAT ALLOWS FOR COLLECTION OF QUANTILES FOR DESCRIPTIVE COLLECTION OF POWER VARIANCE ACROSS THE RECORDING WINDOW(5%, 25%, 50%, 75%, 90%). (D) PERFORMING THE PROCESS IN C FOR EVERY FREQUENCY IN THE SPECTROGRAM ALLOWS FOR THE CREATION OF FIVE PSD-LIKE LINES THAT CONSTITUTE THE LANDSCAPE.

5.3.2 SPECTRAL LANDSCAPES CAPTURE ARHYTHMIC COMPONENTS NESTED WITHIN RHYTHMIC SIGNALS

Fourier-based density estimates, such as the Fourier Transform, Multi-taper Spectrum, Welch's PSD estimate, and even our CMW PSDs are designed to provide information about the constellation of band-specific energies that constitute a given time-series signal. However, they require the data to conform to many assumptions. Chief among those is the assumption that oscillatory contents within a signal are stationary, which means that statistical properties (i.e. mean and variance) of signals at the frequency band being analyzed to not change. For consistent oscillations with mild fluctuations over an analyzed epoch, such as the hippocampal theta rhythm in rodents (5,6,9), these Fourier analyses are often sufficient for capturing the dynamics over time. However, standard PSD estimates taken across long periods of time will fail to reliably capture dynamics for more sporadic rhythms, such as the intermittent gamma-band activity that co-occurs in the troughs of hippocampal theta (1,5,6). To demonstrate this, we simulated a consistent 12Hz oscillation with 35Hz signals occurring in random 250ms bouts. As Figure 5.11 shows, despite the 35Hz activity being clearly visible by eye and in wavelet spectrograms, the wavelet PSD (displayed as the 50% shaded line in 5.11(c)) only captures the consistent 12Hz oscillation in the signal. By contrast, applying our spectral landscapes to these data highlight the 35Hz band in the upper percentiles. When 35Hz occurs only once within the analyzed epoch, landscapes detect the activity only in the highest percentile. As expected, in the case where more bouts occur, we identify 35Hz activity at lower percentiles (75% in 5.11(c), Right).

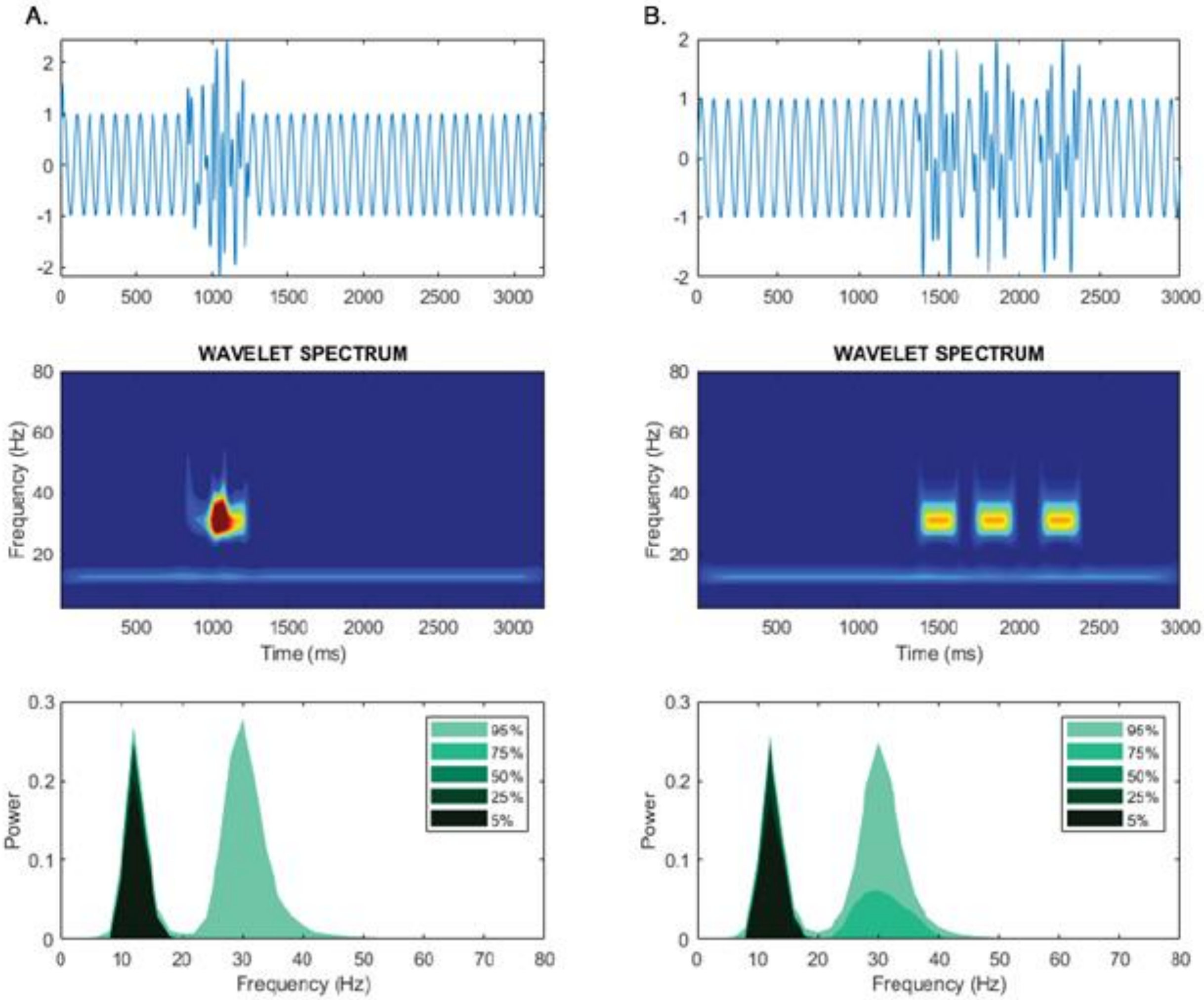

FIGURE 5.11 DIFFERENT LANDSCAPE CHARACTERIZATION PATTERNS

(A) THE LANDSCAPE FOR A SUSTAINED 12HZ SIGNAL AND A SINGLE 30HZ BURST CAPTURES CONSTANT 12HZ POWER ACROSS ALL QUANTILE LINES AND 30HZ POWER ONLY IN THE 90TH PERCENTILE. (B) THE LANDSCAPE FOR A SUSTAINED 12HZ SIGNAL AND MULTIPLE 30HZ BURSTS NOW CAPTURES HIGH FREQUENCY CONTENT ACROSS MORE QUANTILE LINES. NOTE: IN BOTH SCENARIOS THE 50TH PERCENTILE (REPRESENTING THE PSD) FAILS TO CAPTURE HIGH FREQUENCY POWER.

5.3.3 SPECTRAL LANDSCAPES CAPTURE RHYTHMIC BOUTS IN NOISY DATA

Considering the bouts of theta that have been observed in the primate hippocampus (11,12), we asked how spectral landscapes would characterize bouts of sporadic oscillatory activity that occur in the presence of otherwise noisy signals. We assessed this by investigating how sporadic bouts of 12Hz activity would appear in signals otherwise dominated by pink (1/f) noise. Immediately, we can observe a limitation of the landscapes, which is that noise produces elevated power across all frequency bands despite us only manually injecting signal at 12Hz. This might preclude landscapes from revealing the desired signal, however we observed that this was not the case. Our simulations revealed that despite the presence of noise in all percentiles of the landscape, we could still identify putative increases in 12Hz activity (Figure 5.12). This became especially prevalent at higher percentiles, where the changes in activity were much more dramatic than at lower quantile lines.

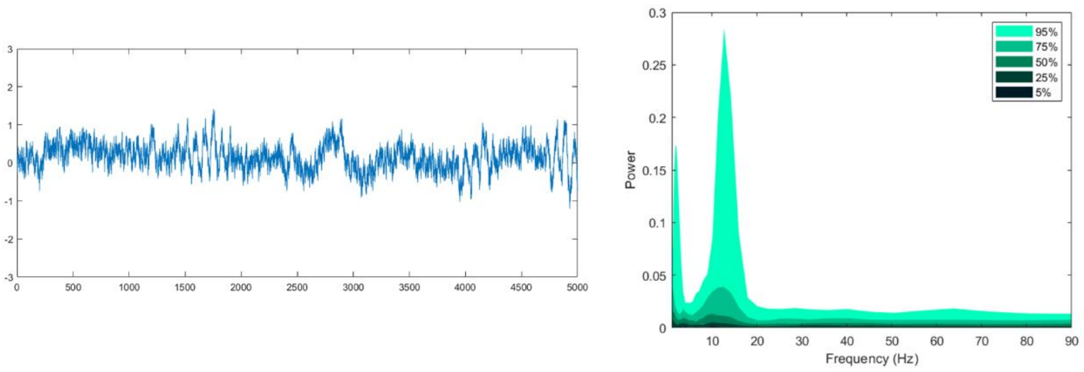

FIGURE 5.12 SPECTRAL LANDSCAPE OF SPORADIC 12HZ BURSTS EMBEDDED IN NOISE.

5.3.4 SPECTRAL LANDSCAPES FROM NEURAL SIGNALS IN THE PRIMATE HIPPOCAMPAL FORMATION

From previous reports (11,12,20), we expected that signals from our chronic, primate hippocampal recordings would lack any oscillations that were stationary for a considerable period. Thus, we applied spectral landscapes to these recordings to assess how signals in different regions within the primate hippocampal formation (HF) change over time as subjects alternate between active engagement in a virtual reality task and quiescence in minimal lighting. Landscapes were created from data recorded from two monkeys with channels located along the extent of the longitudinal axis of the hippocampal formation. We were able to make estimates about anatomical localization of each electrode using a custom co-registration method (Section 5.5). Many days of recordings from each region within the HF were obtained to ensure adequate sampling (min: 132 days, max: 264 days). Landscapes reveal immediate differences across different regions of the hippocampal formation. As Figure 5.13 highlights, when animals engage in virtual reality exploration, the CA3 subfield of the hippocampus proper, the dentate gyrus (DG), and Entorhinal Cortex (EC) elicited increased 10-30Hz activity. During quiescent rest periods, CA1, DG, and Subiculum showed increased variability in the 10-15Hz range. In both these cases, the massive spread between quantiles across all landscapes suggests a sporadic, bout-like nature of activity in the primate hippocampus. Moreover, applying a weighted distribution mean (Tukey’s Trimean) to the landscapes reveals a global trend of network states in the HF to being paced by faster oscillations (20-50Hz) during active exploration and switching to a slower state (3-15Hz) during quiescence (Figure 5.14). This corroborates previous findings in primates (20), although future work will have to assess whether these network states employ the same circuitry of theta generation in rodents.

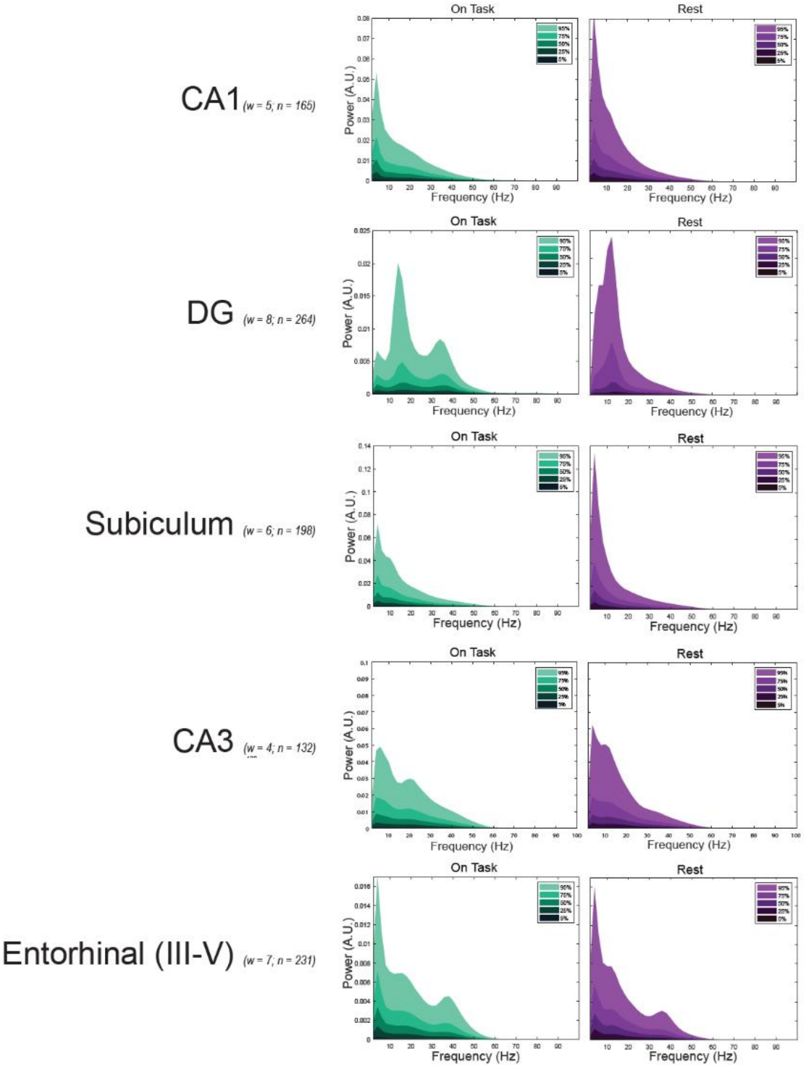

FIGURE 5.13 LANDSCAPES FROM NEURAL RECORDINGS ALONG THE HIPPOCAMPAL FORMATION

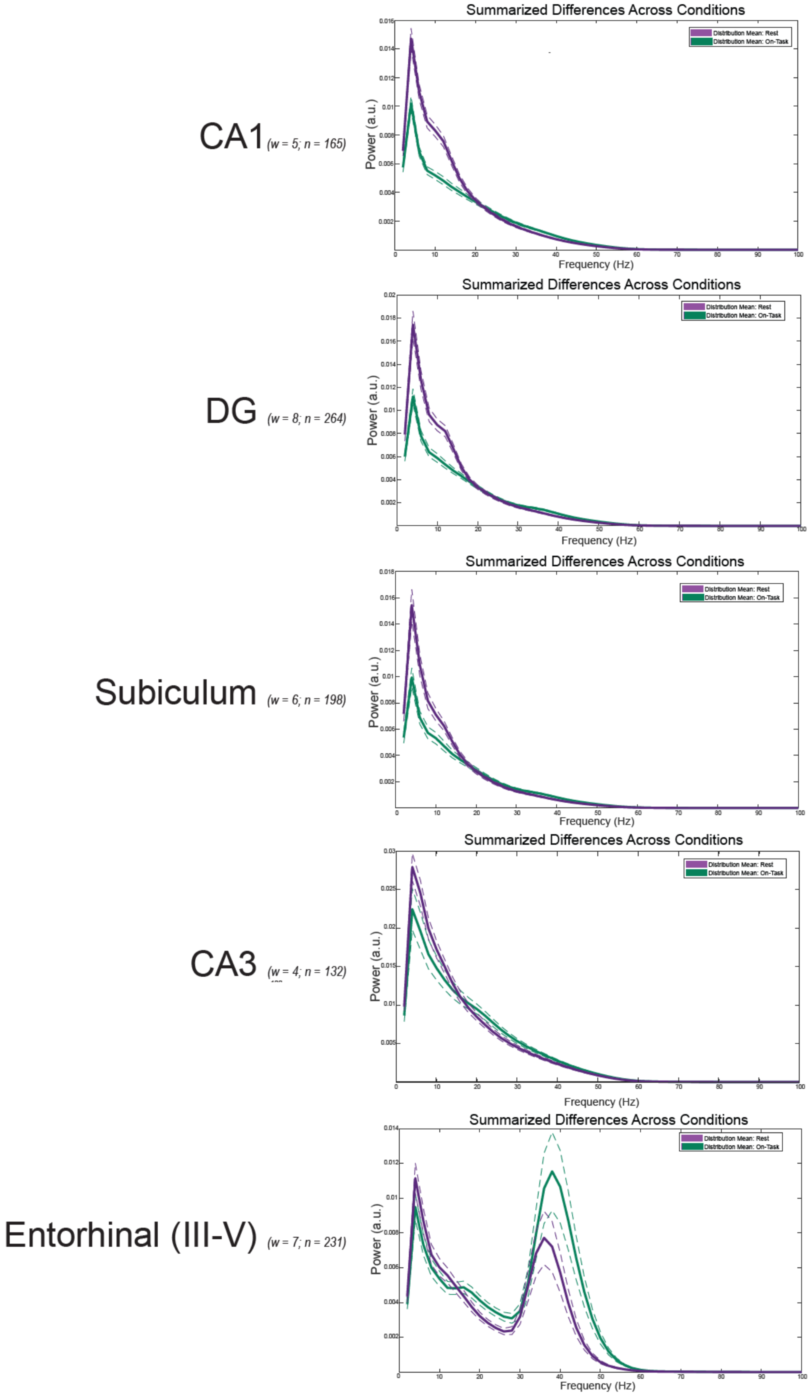

FIGURE 5.14 SUMMARIZED DIFFERENCES OF LANDSCAPES BETWEEN COGNITIVE STATES

5.4 DISCUSSION

In this chapter, we highlighted the capacity of our novel techniques, the SVD-CSA removal and spectral landscapes, to mitigate volume conducted artifact from time series data and capture the variability over time of sporadic oscillatory features, respectively. Data from two animals confirms simulated findings that even strong contaminating signal can be deleted without significant detriment to underlying signals of interest. Moreover, characterizing spectral variability using landscapes reveals a global shift of network states in the hippocampal formation such that the system operates at faster frequencies during active task engagement and switches to slower frequency states during rest. While it is possible that some of these observations may still be occluded by residual artifacts from SVD-CSA removal, the diversity of spectral landscapes across hippocampal sub-regions suggests unique, neurogenic, oscillatory activity during task engagement.

The main motivation for designing these methods stems from two major practical issues experienced during my graduate career while investigating primate neural recordings. My first challenge was being able to eliminate artifact while preserving the underlying signal, rather than tossing many hours and even days of data because of obstructive artifacts. Second, I wanted to be able to better describe how the frequency-specific content of LFP recordings changed for given brain areas in a way that compromised between the data-intensive time-frequency information obtained from a spectrogram, and the overly vague summaries offered by traditional PSD estimates. As our data suggests, SVD-CSA removal and spectral landscapes are helpful tools to tackle these problems.

As with any method, there are some limitations with these techniques. While SVD-CSA removal is oblivious to the frequency information of the data, it is bound by the constraints that artifacts must be phase-aligned across most electrodes in an array. SVD will fail to reliably identify phenomena present on only a scarce number of channels. Additionally, because the method described here operates on broadband data, the subtraction of artifact may induce phase shifts that will have detrimental effects on phase relationships of higher-frequency oscillations. To subvert this, one may low-pass filter the subtraction matrix prior to the operation. It warrants notice that SVD is not a blind source separation method like independent components analysis (ICA), which attempts to reconstruct statistically independent signals from a matrix of time series data assumed to be a constellation of data arising from multiple sources. ICA prevails over SVD-CSA removal when artifacts exist on a subset of channels, and ICA can be used in a similar fashion as SVD for artifact removal (21,22). However, the advantage of SVD-CSA removal over ICA for large artifact removal is that SVD does not estimate signals. In contrast to ICA, every iteration of SVD on a given data set will consistently produce the same variables, in the same order, without changing magnitudes or information content. This is because SVD is deconstructing that matrix as opposed to trying to identify coefficients to estimate the original data. This ultimately leads to faster processing time and better reliability from SVD-CSA removal compared to ICA.

Our spectral landscapes successfully captured variability in different subregions of the primate HF. However, determining the underlying features of the sporadic oscillatory phenotypes is beyond the scope of the landscapes. We provide evidence for participation of different percentiles in the landscape to suggest more frequent occurrences of a given oscillation in the data. However, increased participation could arise from spurious, massive-amplitude noise because the various features of our landscapes stem from a distribution of the data. Outliers placed well beyond the median of our distribution may bias the landscapes artificially. However, I do not mean to sell the landscapes as a complete replacement for the spectrogram. Spectral landscapes should be thought of as an improvement upon traditional Fourier-based energy estimates like the PSD. Subsequent analyses to characterize waveform properties, relationships to spikes, and coherence with other brain areas should always be used as confirmatory measures to ensure identified power (or power variability) observed in landscapes is genuine.

The complex nature of primate hippocampal LFP is reflective of the increased behavioral and cognitive range that the species has over rodents. That said, the lack of sustained theta rhythmicity observed in the monkey hippocampal LFP may also stem from morphological changes in the primate hippocampus. The packing of pyramidal neurons in the primate hippocampus is much more diffuse than that of the rodent

(15). In rodent CA1, the tightly packed row of pyramidal neurons produces a nice electric dipole in the extracellular space, which leads to easily detectible mesoscopic electrical changes recorded by the LFP (1). In primates, all hippocampal subfields have staggered pyramidal layers that cause an inconsistent gradient of ion flow and makes accurate detection of neurogenic events much more difficult (15). Changes in intrinsic and extrinsic connectivity also have a large influence on the degree of synchrony (See Chapter 2). In rodents, the theta rhythms observed in area CA3 are much noisier than those observed in CA1 (16), and as such the latter is typically targeted for clean theta signals. Given the sporadic nature of our findings, directly manipulating the microcircuitry using methods described in Chapter 3 would be instrumental for deducing frequency-specific network states within the macaque hippocampus. Nevertheless, our findings provide a first step towards demystifying the subregions in the primate HF.

5.5 EXPERIMENTAL METHODS

5.5.1 CHRONIC HIGH-DENSITY EXPERIMENTS

The methods utilized for the chronic high-density recordings used for the analyses in this chapter are the same as those described in Chapter 4. Briefly, two animals trained via positive reinforcement to sit and become head-fixed in a custom-made primate chair were implanted with a 124-channel hyperdrive (Gray Matter Research) centered on the skull above the hippocampus. Each channel consisted of a 100-micron tungsten wire (FHC), and all 124 channels were spaced 1.25 mm apart from each other. During recording sessions, animals alternated between active exploration in a virtual environment (Unity 2017.f) and periods of quiescence in minimal ambient light.

5.5.2 DATA COLLECTION AND PRE-PROCESSING

Data collection occurred in the same manner as described in Chapter 4. Data from each wire/channel was collected using a Neuralynx Cheetah system (v6.0). Neural signals were collected at 32kHz and collected in wideband format (0.1-8000Hz). For LFP collection, data was first low-pass filtered (0.1-1000Hz) to avoid aliasing and then downsampled to 1KHz. During collection, data was referenced to the animals' headpost implant to mitigate contamination of collected signals by volume conducted noise. Data from each channel was manually inspected to identify strong contamination by 60Hz line noise, and in cases where line noise obfuscated the underlying recordings, data was notch-filtered using a spectrum interpolation technique presented Mewett et al. (18). Signals were then mean centered and normalized (z score) prior to further analysis.

5.5.3 MRI CO-REGISTRATION AND ANATOMICAL LOCALIZATION

Anatomical localization estimates of our chronic recordings was the same MRI-based procedure as detailed in Chapter 4. Monkeys underwent a pre-operative MRI, and an MRI after initial hyperdrive chamber placement. The post-operative MRI included a set of fiducial markers mounted on the animals' heads to estimate the angle and placement of the drive. However, because of distortion induced by the chamber, final models of alignment were generated (.STL) using a combination of post-operative measurements, stereotactic X-rays, and 3D scans of the animals' heads and drives.

The starting positions for each electrode were estimated from the drive alignment models. Electrodes were manually turned down into desired recording locations using precise turns of screws at the drive base. Turns were manually logged, and electrode distance across all recording sessions was estimated using the measured distance correlation from one full turn during non-implanted practice turns. These distances were transformed into 3-D coordinates using the alignment models as a starting reference. X-ray images were used to confirm that electrode trajectories did not deviate, and any electrodes not progressing in a straight line stopped being turned. Models of the hippocampal formation (.STL) were made in an MRI processing suite (3D Slicer), and scripts for estimating 3D position of each electrode were made in MATLAB that incorporated information from turn count estimates and drive placement estimates. Subregion determination was performed automatically by comparing an electrode's 3D position estimate and the 3D coordinates of manually identified hippocampal subregions from the MRI, and these determinations were manually verified by comparing positions in the MRI.

CHAPTER 6 || CONCLUDING REMARKS AND FUTURE DIRECTIONS

6.1 WHAT DID WE ACCOMPLISH HERE?

The findings and theories presented in this thesis reflect a portion of six and a half challenging years of work dedicated towards better understanding how synchrony within the hippocampus facilitates its role in learning and memory. I performed the first comprehensive meta-analysis of the literature surrounding the entorhinal cortex and have provided a basis to study this structure as more than a passive relay to the hippocampus. I have successfully shown that motifs of sharp-wave ripple travel during quiescence are like the patterns observed in rats. Specifically, I found that many events only persist near the site of generation. However, I also observed that many ripples travel along the longitudinal extent of the hippocampus in multi-directional ways. This shows that at a systems level, the hippocampus engages in unique mechanisms of communication with extrinsic brain regions during memory consolidation epochs. I also elucidate different network states at slower frequencies that the hippocampus shifts between as animals alternate between active engagement in memory-dependent behaviors and quiescence. From these same findings, I also provide the first evidence that the primate hippocampus, like that of rodents, exhibits sub-region-specific hallmarks of physiology observed via recorded local field potentials (LFP). These data serve to bolster the burgeoning field of hippocampal physiology and highlight global phenotypes of neural dynamics that can help future researchers disambiguate between subfields when attempting to record from the hippocampus. Moreover, the results presented here provide key preliminary insight into the circuit mechanisms elicited by various subregions of primate hippocampal formation during different cognitive states (active exploration vs. rest).

The scientific findings in this body of work were accompanied by the development of multiple novel techniques, some of which were integral to the discoveries themselves. To efficiently mitigate large, obfuscating artifacts seen in my lab's neural recordings, I designed a filter using singular value decomposition (SVD) that identifies large, synchronous potentials in our data in the first SVD mode. The first mode had a striking resemblance to the cross-channel average (common source average; CSA). Thus, subtracting the first SVD mode from the signals (SVD-CSA removal) eliminated that mean and illuminated the true dimensionality of the neural data. However, because the neural data was still noisy in nature, using gross power spectral density estimates was insufficient to explain the various dynamics contained in the data. Yet, taking spectrograms was too memory-intensive and time consuming for the sheer size of the data from our high-density recordings. I struck a compromise between the lackluster PSD estimates and overly detailed spectrograms by creating the spectral landscape, which applies a five-point summary method to each frequency of the spectrogram to ask how frequency-specific power varies over a given epoch. These landscapes, together with denoising with SVD-CSA removal, allowed for more nuanced insight into hallmarks of state-specific neurophysiology in the primate hippocampus.

Any findings with LFP observations should be validated with manipulation experiments to ask the relevant purpose the identified mesoscopic signal plays with the microcircuits that generate it. However, in primates use of manipulation techniques, especially novel genetic technologies such as optogenetics, are risky and come at great cost to pilot methods. To circumvent this, I helped develop a pipeline for intracranial viral deliveries alongside close collaborators from multiple institutions to help plan and validate injection surgeries while reducing the number of animals needed to pilot these procedures.

6.2 WHERE DO WE GO FROM HERE?

The field of primate hippocampal physiology has made great strides in disambiguating the hippocampal formation’s structure and function from that of rodents. Many advancements have been made from neural recordings about how both spatial and contextual information may coalesce in the regions within this area to enable learning, memory, planning, and even navigation in both real and virtual environments. While this thesis certainly contributes findings that help further illuminate our knowledge of hippocampal function, I believe that the methods contained within this work can bring studies of the primate hippocampus to further prominence. Use of spectral landscapes should be applied to data from acute hippocampal recordings, and chronic recordings from more animals, to make define more concrete phenotypes of sub-regions within the hippocampus. Additionally, future chronic recordings should investigate previous findings from acute studies after volume conduction is removed to validate the observations made are not artifactual. Of course, future studies need to address the potential functional role of subregions within the primate entorhinal cortex. Chronic arrays like our Gray Matter hyperdrives should be implanted that target the entorhinal cortex in animals engaged in various behaviors. Specific investigations should focus on sub-region-specific physiology and the potential for modality-specific contributions of different entorhinal subregions to the information processed and sent to the hippocampus proper. Recent work in rodents suggests that more neurons in the entorhinal cortex integrate conjunctive information than previously reported (1). Considering the reduced reciprocal connectivity within the primate entorhinal cortex relative to that of rodents, it stands to reason that the entorhinal cortex of primates would elicit a remarkable myriad of neural dynamics.

I am personally most excited to see how genetic manipulation experiments in the primate hippocampal formation shape our hypotheses and theories of function in these medial temporal lobe structures. In rodents, perturbing ripples severely impairs memory-dependent behaviors (2). Given our findings that ripples in the primate behave in a similar fashion to those in naturally behaving rodents, it seems necessary to assess whether the sharp-wave ripple is as critical in primates for proper memory consolidation after learning, and whether ripple generation in primates is strongly influenced by acetylcholine dynamics (2). With respect to waking oscillations, optogenetic manipulations in rodents highlight the proclivity of the hippocampal microcircuitry to oscillate at specific frequencies within the theta range (3). We do not observe sustained oscillations of a particular frequency in primates, and similar theta-pacing studies can directly assess whether this is because the network itself does not inherently oscillate, even with a periodic extrinsic drive. On the other hand, if the primate hippocampus can be induced into a sustained oscillatory state, what influence does that have on exploratory behaviors? Because of previous connections to theta bouts and eye movements (4, 5, 6), does a sustained theta rhythm in the hippocampus somehow induce a series of non-stop search behaviors that would otherwise not be present in monkeys? Additionally, theta manipulation work in rodents highlights a necessity for cholinergic and glutamatergic drive to the hippocampus for proper theta-range oscillatory dynamics (3, 7). To date, we have no direct evidence for how specific neurotransmitters in the macaque hippocampus enable or prohibit the oscillatory phenotypes we observe and only circuitous evidence from anesthesia studies of a role of acetylcholine (8). Applying these state of the art, cell specific manipulations in the monkey hippocampus would not only be flashy but could provide real insight into expected phenotypes after neurodegeneration in this region, such as after severe Alzheimer's or epilepsy.

Ultimately, many of our theories of dysfunction in the human hippocampus stem from studies in rodents. However, comparing studies of function between rodents and primates suggests large physiological discrepancies that ultimately make identifying disruptive phenotypes difficult. Non-human primates are the critical bridge to understanding how a healthy primate hippocampus should operate, what its physiology should look like, and what neurotransmitters critically contribute to proper physiology and function. By improving our tools for analyzing the complex network dynamics elicited by the hippocampus and manipulating the dynamic-generating neurocircuitry, scientists will be able to both elevate the field of monkey hippocampology and make more definitive translational claims about how the healthy primate hippocampus contributes to proper learning and memory function.

LITERATURE CITED

CHAPTER 1:

1. Andersen, Per and others (eds), The Hippocampus Book, Oxford Neuroscience Series (New York, 2006; online edn, Oxford Academic, 1 May 2009), https://doi.org/10.1093/acprof:oso/9780195100273.001.0001.
2. O'Keefe J, Dostrovsky J. The hippocampus as a spatial map. Preliminary evidence from unit activity in the freely-moving rat. Brain Res. 1971 Nov;34(1):171-5. doi: 10.1016/0006-8993(71)90358-1. PMID: 5124915.
3. Fyhn M, Molden S, Witter MP, Moser EI, Moser MB. Spatial representation in the entorhinal cortex. Science. 2004 Aug 27;305(5688):1258-64. doi: 10.1126/science.1099901. PMID: 15333832.
4. O'Keefe, J; Nadel, L; (1978) The Hippocampus as a Cognitive Map. Oxford University Press: Oxford, UK.
5. Eichenbaum H. The Hippocampus as a Cognitive Map … of Social Space. Neuron. 2015 Jul 1;87(1):9-11. doi: 10.1016/j.neuron.2015.06.013. PMID: 26139366.
6. Dusek JA, Eichenbaum H. The hippocampus and memory for orderly stimulus relations. Proc Natl Acad Sci U S A. 1997 Jun 24;94(13):7109-14. doi: 10.1073/pnas.94.13.7109. PMID: 9192700; PMCID: PMC21293.
7. SCOVILLE WB, MILNER B. Loss of recent memory after bilateral hippocampal lesions. J Neurol Neurosurg Psychiatry. 1957 Feb;20(1):11-21. doi: 10.1136/jnnp.20.1.11. PMID: 13406589; PMCID: PMC497229.
8. Beason-Held LL, Rosene DL, Killiany RJ, Moss MB. Hippocampal formation lesions produce memory impairment in the rhesus monkey. Hippocampus. 1999;9(5):562-74. doi: 10.1002/(SICI)1098-1063(1999)9:5<562::AID-HIPO10>3.0.CO;2-X. PMID: 10560927.
9. Basile BM, Templer VL, Gazes RP, Hampton RR. Preserved visual memory and relational cognition performance in monkeys with selective hippocampal lesions. Sci Adv. 2020 Jul 17;6(29):eaaz0484. doi: 10.1126/sciadv.aaz0484. PMID: 32832615; PMCID: PMC7439495.
10. Rolls ET, O'Mara SM. View-responsive neurons in the primate hippocampal complex. Hippocampus. 1995;5(5):409-24. doi: 10.1002/hipo.450050504. PMID: 8773254.
11. Strange BA, Witter MP, Lein ES, Moser EI. Functional organization of the hippocampal longitudinal axis. Nat Rev Neurosci. 2014 Oct;15(10):655-69. doi: 10.1038/nrn3785. PMID: 25234264.
12. Garcia AD, Buffalo EA. Anatomy and Function of the Primate Entorhinal Cortex. Annu Rev Vis Sci. 2020 Sep 15;6:411-432. doi: 10.1146/annurev-vision-030320-041115. Epub 2020 Jun 24. PMID: 32580662.
13. Rueckemann JW, Sosa M, Giocomo LM, Buffalo EA. The grid code for ordered experience. Nat Rev Neurosci. 2021 Oct;22(10):637-649. doi: 10.1038/s41583-021-00499-9. Epub 2021 Aug 27. PMID: 34453151; PMCID: PMC9371942.
14. Witter MP. Organization of the entorhinal-hippocampal system: a review of current anatomical data. Hippocampus. 1993;3 Spec No:33-44. PMID: 8287110.
15. Insausti R, Marcos MP, Mohedano-Moriano A, Arroyo-Jiminez MM, Corcoles-Parada M, Artacho-Perula E, Ubero-Martinez MM, Munoz-Lopez M (2017) The nonhuman primate hippocampus: neuroanatomy and patterns of cortical connectivity. In: The hippocampus from cells to systems: structure, connectivity, and functional contributions to memory and flexible cognition (Hannula DE, Duff MC , eds), pp 3–36. Cham: Springer.
16. Insausti R, Muñoz-López M, Insausti AM, Artacho-Pérula E. The Human Periallocortex: Layer Pattern in Presubiculum, Parasubiculum and Entorhinal Cortex. A Review. Front Neuroanat. 2017 Oct 4;11:84. doi: 10.3389/fnana.2017.00084. PMID: 29046628; PMCID: PMC5632821.

17. BRODAL A. The hippocampus and the sense of smell; a review. Brain. 1947 Jun;70(Pt 2):179-222. doi: 10.1093/brain/70.2.179. PMID: 20261820.
18. Architecture of the Entorhinal Cortex A Review of Entorhinal Anatomy in Rodents with Some Comparative Notes
19. Papez JW. A proposed mechanism of emotion. 1937. J Neuropsychiatry Clin Neurosci. 1995 Winter;7(1):103-12. doi: 10.1176/jnp.7.1.103. PMID: 7711480.
20. Klüver Heinrich Bucy PC. "Psychic Blindness" and Other Symptoms Following Bilateral Temporal Lobectomy in Rhesus Monkeys. s.n; 1937.
21. MISHKIN M. Visual discrimination performance following partial ablations of the temporal lobe. II. Ventral surface vs. hippocampus. J Comp Physiol Psychol. 1954 Jun;47(3):187-93. doi: 10.1037/h0057551. PMID: 13163252.
22. Muñoz KE, Meyer-Lindenberg A, Hariri AR, Mervis CB, Mattay VS, Morris CA, Berman KF. Abnormalities in neural processing of emotional stimuli in Williams syndrome vary according to social vs. non-social content. Neuroimage. 2010 Mar;50(1):340-6. doi: 10.1016/j.neuroimage.2009.11.069. Epub 2009 Dec 11. PMID: 20004252; PMCID: PMC3013360.
23. Aggleton JP. The contribution of the amygdala to normal and abnormal emotional states. Trends Neurosci. 1993 Aug;16(8):328-33. doi: 10.1016/0166-2236(93)90110-8. PMID: 7691009.
24. Brown Sanger and Sharpey-Schafer Edward Albert 1888XI. An investigation into the functions of the occipital and temporal lobes of the monkey's brain. Phil. Trans. R. Soc. Lond. B179: 303–327. http://doi.org/10.1098/rstb.1888.0011
25. Morris RG, Garrud P, Rawlins JN, O'Keefe J. Place navigation impaired in rats with hippocampal lesions. Nature. 1982 Jun 24;297(5868):681-3. doi: 10.1038/297681a0. PMID: 7088155.
26. Clark RE, Zola SM, Squire LR. Impaired recognition memory in rats after damage to the hippocampus. J Neurosci. 2000 Dec 1;20(23):8853-60. doi: 10.1523/JNEUROSCI.20-23-08853.2000. PMID: 11102494; PMCID: PMC6773055.
27. van Strien NM, Cappaert NL, Witter MP. The anatomy of memory: an interactive overview of the parahippocampal-hippocampal network. Nat Rev Neurosci. 2009 Apr;10(4):272-82. doi: 10.1038/nrn2614. PMID: 19300446.
28. Eichenbaum H, Sauvage M, Fortin N, Komorowski R, Lipton P. Towards a functional organization of episodic memory in the medial temporal lobe. Neurosci Biobehav Rev. 2012 Aug;36(7):1597-608. doi: 10.1016/j.neubiorev.2011.07.006. Epub 2011 Jul 23. PMID: 21810443; PMCID: PMC3227798.
29. Rueckemann JW, Buffalo EA. Spatial Responses, Immediate Experience, and Memory in the Monkey Hippocampus. Curr Opin Behav Sci. 2017 Oct;17:155-160. doi: 10.1016/j.cobeha.2017.08.008. Epub 2017 Sep 5. PMID: 29255777; PMCID: PMC5731786.
30. Beason-Held LL, Rosene DL, Killiany RJ, Moss MB. Hippocampal formation lesions produce memory impairment in the rhesus monkey. Hippocampus. 1999;9(5):562-74. doi: 10.1002/(SICI)1098-1063(1999)9:5<562::AID-HIPO10>3.0.CO;2-X. PMID: 10560927.
31. Lavenex PB, Amaral DG, Lavenex P. Hippocampal lesion prevents spatial relational learning in adult macaque monkeys. J Neurosci. 2006 Apr 26;26(17):4546-58. doi: 10.1523/JNEUROSCI.5412-05.2006. PMID: 16641234; PMCID: PMC6674053.
32. Heuer E, Bachevalier J. Effects of selective neonatal hippocampal lesions on tests of object and spatial recognition memory in monkeys. Behav Neurosci. 2011 Apr;125(2):137-49. doi: 10.1037/a0022539. PMID: 21341885; PMCID: PMC3072249.
33. Zola-Morgan SM, Squire LR. The primate hippocampal formation: evidence for a time-limited role in memory storage. Science. 1990 Oct 12;250(4978):288-90. doi: 10.1126/science.2218534. PMID: 2218534.
34. Nilssen ES, Doan TP, Nigro MJ, Ohara S, Witter MP. Neurons and networks in the entorhinal cortex: A reappraisal of the lateral and medial entorhinal subdivisions mediating parallel cortical

pathways. Hippocampus. 2019 Dec;29(12):1238-1254. doi: 10.1002/hipo.23145. Epub 2019 Aug 13. Erratum in: Hippocampus. 2020 Aug;30(8):909. PMID: 31408260.

35. Ramirez JJ, Campbell D, Poulton W, Barton C, Swails J, Geghman K, Courchesne SL, Wentworth S. Bilateral entorhinal cortex lesions impair acquisition of delayed spatial alternation in rats. Neurobiol Learn Mem. 2007 Feb;87(2):264-8. doi: 10.1016/j.nlm.2006.09.002. Epub 2006 Oct 16. PMID: 17049284; PMCID: PMC1839929.
36. Robinson NTM, Priestley JB, Rueckemann JW, Garcia AD, Smeglin VA, Marino FA, Eichenbaum H. Medial Entorhinal Cortex Selectively Supports Temporal Coding by Hippocampal Neurons. Neuron. 2017 May 3;94(3):677-688.e6. doi: 10.1016/j.neuron.2017.04.003. Epub 2017 Apr 20. PMID: 28434800; PMCID: PMC5465388.
37. Leonard BW, Amaral DG, Squire LR, Zola-Morgan S. Transient memory impairment in monkeys with bilateral lesions of the entorhinal cortex. J Neurosci. 1995 Aug;15(8):5637-59. doi: 10.1523/JNEUROSCI.15-08-05637.1995. PMID: 7643207; PMCID: PMC6577641.
38. Buckmaster CA, Eichenbaum H, Amaral DG, Suzuki WA, Rapp PR. Entorhinal cortex lesions disrupt the relational organization of memory in monkeys. J Neurosci. 2004 Nov 3;24(44):9811-25. doi: 10.1523/JNEUROSCI.1532-04.2004. PMID: 15525766; PMCID: PMC6730224.
39. Colgin LL. Five Decades of Hippocampal Place Cells and EEG Rhythms in Behaving Rats. J Neurosci. 2020 Jan 2;40(1):54-60. doi: 10.1523/JNEUROSCI.0741-19.2019. Epub 2019 Aug 26. PMID: 31451578; PMCID: PMC6939480.
40. Grieves RM, Wood ER, Dudchenko PA. Place cells on a maze encode routes rather than destinations. Elife. 2016 Jun 10;5:e15986. doi: 10.7554/eLife.15986. PMID: 27282386; PMCID: PMC4942257.
41. Ormond, J, O’Keefe’ JO. Hippocampal place cells use vector computations to navigate. bioRxiv. 2021.06.23.449621; doi: https://doi.org/10.1101/2021.06.23.449621
42. Hainmueller T, Bartos M. Dentate gyrus circuits for encoding, retrieval and discrimination of episodic memories. Nat Rev Neurosci. 2020 Mar;21(3):153-168. doi: 10.1038/s41583-019-0260-z. Epub 2020 Feb 10. PMID: 32042144; PMCID: PMC7115869.
43. Senzai Y, Buzsáki G. Physiological Properties and Behavioral Correlates of Hippocampal Granule Cells and Mossy Cells. Neuron. 2017 Feb 8;93(3):691-704.e5. doi: 10.1016/j.neuron.2016.12.011. Epub 2017 Jan 26. PMID: 28132824; PMCID: PMC5293146.
44. Simonnet J, Brecht M. Burst Firing and Spatial Coding in Subicular Principal Cells. J Neurosci. 2019 May 8;39(19):3651-3662. doi: 10.1523/JNEUROSCI.1656-18.2019. Epub 2019 Feb 28. PMID: 30819796; PMCID: PMC6510334.
45. Ledergerber D, Battistin C, Blackstad JS, Gardner RJ, Witter MP, Moser MB, Roudi Y, Moser EI. Task-dependent mixed selectivity in the subiculum. Cell Rep. 2021 May 25;35(8):109175. doi: 10.1016/j.celrep.2021.109175. PMID: 34038726; PMCID: PMC8170370.
46. Sharp PE. Subicular place cells generate the same "map" for different environments: comparison with hippocampal cells. Behav Brain Res. 2006 Nov 11;174(2):206-14. doi: 10.1016/j.bbr.2006.05.034. Epub 2006 Jul 21. PMID: 16859764.
47. Dong C, Madar AD, Sheffield MEJ. Distinct place cell dynamics in CA1 and CA3 encode experience in new environments. Nat Commun. 2021 May 20;12(1):2977. doi: 10.1038/s41467-021-23260-3. PMID: 34016996; PMCID: PMC8137926.
48. Diehl GW, Hon OJ, Leutgeb S, Leutgeb JK. Grid and Nongrid Cells in Medial Entorhinal Cortex Represent Spatial Location and Environmental Features with Complementary Coding Schemes. Neuron. 2017 Apr 5;94(1):83-92.e6. doi: 10.1016/j.neuron.2017.03.004. Epub 2017 Mar 23. PMID: 28343867; PMCID: PMC5444540.
49. Mao D, Avila E, Caziot B, Laurens J, Dickman JD, Angelaki DE. Spatial modulation of hippocampal activity in freely moving macaques. Neuron. 2021 Nov 3;109(21):3521-3534.e6. doi: 10.1016/j.neuron.2021.09.032. Epub 2021 Oct 12. PMID: 34644546; PMCID: PMC8571030.

50. Konig SD, Buffalo EA. Remembering What We’ve Seen: The Hippocampus and Relational Memory. UW Libraries. 2017.
51. Browning JI, Buffalo EA. Monkey Hippocampal Neurons Track Ongoing Experiences. UW Libraries. 2021.
52. Killian NJ, Jutras MJ, Buffalo EA. A map of visual space in the primate entorhinal cortex. Nature. 2012 Nov 29;491(7426):761-4. doi: 10.1038/nature11587. Epub 2012 Oct 28. PMID: 23103863; PMCID: PMC3565234.
53. Eichenbaum H. Time cells in the hippocampus: a new dimension for mapping memories. Nat Rev Neurosci. 2014 Nov;15(11):732-44. doi: 10.1038/nrn3827. Epub 2014 Oct 1. PMID: 25269553; PMCID: PMC4348090.
54. Bright IM, Meister MLR, Cruzado NA, Tiganj Z, Buffalo EA, Howard MW. A temporal record of the past with a spectrum of time constants in the monkey entorhinal cortex. Proc Natl Acad Sci U S A. 2020 Aug 18;117(33):20274-20283. doi: 10.1073/pnas.1917197117. Epub 2020 Aug 3. PMID: 32747574; PMCID: PMC7443936.
55. Aronov D, Nevers R, Tank DW. Mapping of a non-spatial dimension by the hippocampal-entorhinal circuit. Nature. 2017 Mar 29;543(7647):719-722. doi: 10.1038/nature21692. PMID: 28358077; PMCID: PMC5492514.
56. Baraduc P, Duhamel JR, Wirth S. Schema cells in the macaque hippocampus. Science. 2019 Feb 8;363(6427):635-639. doi: 10.1126/science.aav5404. PMID: 30733419.
57. Rueckemann JW, Buffalo EA. Neuroscience: Auditory landscape on the cognitive map. Nature. 2017 Mar 29;543(7647):631-632. doi: 10.1038/543631a. PMID: 28358066.
58. McNaughton BL, Battaglia FP, Jensen O, Moser EI, Moser MB. Path integration and the neural basis of the 'cognitive map'. Nat Rev Neurosci. 2006 Aug;7(8):663-78. doi: 10.1038/nrn1932. PMID: 16858394.
59. McNaughton BL, Battaglia FP, Jensen O, Moser EI, Moser MB. Path integration and the neural basis of the 'cognitive map'. Nat Rev Neurosci. 2006 Aug;7(8):663-78. doi: 10.1038/nrn1932. PMID: 16858394.
60. Buzsaki, G. (2006) Rhythms of the Brain. Oxford University Press, Oxford. http://dx.doi.org/10.1093/acprof:oso/9780195301069.001.0001
61. Liu AA, Henin S, Abbaspoor S, Bragin A, Buffalo EA, Farrell JS, Foster DJ, Frank LM, Gedankien T, Gotman J, Guidera JA, Hoffman KL, Jacobs J, Kahana MJ, Li L, Liao Z, Lin JJ, Losonczy A, Malach R, van der Meer MA, McClain K, McNaughton BL, Norman Y, Navas-Olive A, de la Prida LM, Rueckemann JW, Sakon JJ, Skelin I, Soltesz I, Staresina BP, Weiss SA, Wilson MA, Zaghloul KA, Zugaro M, Buzsáki G. A consensus statement on detection of hippocampal sharp wave ripples and differentiation from other fast oscillations. Nat Commun. 2022 Oct 12;13(1):6000. doi: 10.1038/s41467-022-33536-x. PMID: 36224194; PMCID: PMC9556539.
62. Sanes JN, Donoghue JP. Oscillations in local field potentials of the primate motor cortex during voluntary movement. Proc Natl Acad Sci U S A. 1993 May 15;90(10):4470-4. doi: 10.1073/pnas.90.10.4470. PMID: 8506287; PMCID: PMC46533.
63. Rickert J, Oliveira SC, Vaadia E, Aertsen A, Rotter S, Mehring C. Encoding of movement direction in different frequency ranges of motor cortical local field potentials. J Neurosci. 2005 Sep 28;25(39):8815-24. doi: 10.1523/JNEUROSCI.0816-05.2005. PMID: 16192371; PMCID: PMC6725584.
64. Khorasani A, Heydari Beni N, Shalchyan V, Daliri MR. Continuous Force Decoding from Local Field Potentials of the Primary Motor Cortex in Freely Moving Rats. Sci Rep. 2016 Oct 21;6:35238. doi: 10.1038/srep35238. PMID: 27767063; PMCID: PMC5073334.
65. Jung, R., Kornmüller, A.E. Eine Methodik der Ableitung Iokalisierter Potentialschwankungen aus subcorticalen Hirngebieten. Archiv f. Psychiatrie 109, 1–30 (1938). https://doi.org/10.1007/BF02157817

66. Vanderwolf CH. Hippocampal electrical activity and voluntary movement in the rat. Electroencephalogr Clin Neurophysiol. 1969 Apr;26(4):407-18. doi: 10.1016/0013-4694(69)90092-3. PMID: 4183562.
67. Buzsáki G, Leung LW, Vanderwolf CH. Cellular bases of hippocampal EEG in the behaving rat. Brain Res. 1983 Oct;287(2):139-71. doi: 10.1016/0165-0173(83)90037-1. PMID: 6357356.
68. Kennedy JP, Zhou Y, Qin Y, Lovett SD, Sheremet A, Burke SN, Maurer AP. A Direct Comparison of Theta Power and Frequency to Speed and Acceleration. J Neurosci. 2022 May 25;42(21):4326-4341. doi: 10.1523/JNEUROSCI.0987-21.2022. Epub 2022 Apr 27. PMID: 35477905; PMCID: PMC9145239.
69. Ranade S, Hangya B, Kepecs A. Multiple modes of phase locking between sniffing and whisking during active exploration. J Neurosci. 2013 May 8;33(19):8250-6. doi: 10.1523/JNEUROSCI.3874-12.2013. PMID: 23658164; PMCID: PMC3785235.
70. Skaggs WE, McNaughton BL, Wilson MA, Barnes CA. Theta phase precession in hippocampal neuronal populations and the compression of temporal sequences. Hippocampus. 1996;6(2):149-72. doi: 10.1002/(SICI)1098-1063(1996)6:2<149::AID-HIPO6>3.0.CO;2-K. PMID: 8797016.
71. Dragoi G, Buzsáki G. Temporal encoding of place sequences by hippocampal cell assemblies. Neuron. 2006 Apr 6;50(1):145-57. doi: 10.1016/j.neuron.2006.02.023. PMID: 16600862.
72. Brandon MP, Bogaard AR, Libby CP, Connerney MA, Gupta K, Hasselmo ME. Reduction of theta rhythm dissociates grid cell spatial periodicity from directional tuning. Science. 2011 Apr 29;332(6029):595-9. doi: 10.1126/science.1201652. PMID: 21527714; PMCID: PMC3252766.
73. Bolding KA, Ferbinteanu J, Fox SE, Muller RU. Place cell firing cannot support navigation without intact septal circuits. Hippocampus. 2020 Mar;30(3):175-191. doi: 10.1002/hipo.23136. Epub 2019 Jul 13. PMID: 31301167.
74. Jutras MJ, Fries P, Buffalo EA. Oscillatory activity in the monkey hippocampus during visual exploration and memory formation. Proc Natl Acad Sci U S A. 2013 Aug 6;110(32):13144-9. doi: 10.1073/pnas.1302351110. Epub 2013 Jul 22. PMID: 23878251; PMCID: PMC3740906.
75. Eliav T, Geva-Sagiv M, Yartsev MM, Finkelstein A, Rubin A, Las L, Ulanovsky N. Nonoscillatory Phase Coding and Synchronization in the Bat Hippocampal Formation. Cell. 2018 Nov 1;175(4):1119-1130.e15. doi: 10.1016/j.cell.2018.09.017. Epub 2018 Oct 11. PMID: 30318145.
76. Davis ZW, Benigno GB, Fletterman C, Desbordes T, Steward C, Sejnowski TJ, H Reynolds J, Muller L. Spontaneous traveling waves naturally emerge from horizontal fiber time delays and travel through locally asynchronous-irregular states. Nat Commun. 2021 Oct 18;12(1):6057. doi: 10.1038/s41467-021-26175-1. PMID: 34663796; PMCID: PMC8523565.
77. Jutras MJ, Fries P, Buffalo EA. Gamma-band synchronization in the macaque hippocampus and memory formation. J Neurosci. 2009 Oct 7;29(40):12521-31. doi: 10.1523/JNEUROSCI.0640-09.2009. PMID: 19812327; PMCID: PMC2785486.
78. Gulli RA, Duong LR, Corrigan BW, Doucet G, Williams S, Fusi S, Martinez-Trujillo JC. Context-dependent representations of objects and space in the primate hippocampus during virtual navigation. Nat Neurosci. 2020 Jan;23(1):103-112. doi: 10.1038/s41593-019-0548-3. Epub 2019 Dec 23. PMID: 31873285.
79. Norman Y, Yeagle EM, Khuvis S, Harel M, Mehta AD, Malach R. Hippocampal sharp-wave ripples linked to visual episodic recollection in humans. Science. 2019 Aug 16;365(6454):eaax1030. doi: 10.1126/science.aax1030. PMID: 31416934.
80. Wilson MA, McNaughton BL. Reactivation of hippocampal ensemble memories during sleep. Science. 1994 Jul 29;265(5172):676-9. doi: 10.1126/science.8036517. PMID: 8036517.
81. Pfeiffer BE, Foster DJ. Hippocampal place-cell sequences depict future paths to remembered goals. Nature. 2013 May 2;497(7447):74-9. doi: 10.1038/nature12112. Epub 2013 Apr 17. PMID: 23594744; PMCID: PMC3990408.

82. Girardeau G, Benchenane K, Wiener SI, Buzsáki G, Zugaro MB. Selective suppression of hippocampal ripples impairs spatial memory. Nat Neurosci. 2009 Oct;12(10):1222-3. doi: 10.1038/nn.2384. Epub 2009 Sep 13. PMID: 19749750.
83. Leonard TK, Hoffman KL. Sharp-Wave Ripples in Primates Are Enhanced near Remembered Visual Objects. Curr Biol. 2017 Jan 23;27(2):257-262. doi: 10.1016/j.cub.2016.11.027. Epub 2016 Dec 29. PMID: 28041797.
84. Hussin AT, Leonard TK, Hoffman KL. Sharp-wave ripple features in macaques depend on behavioral state and cell-type specific firing. Hippocampus. 2020 Jan;30(1):50-59. doi: 10.1002/hipo.23046. Epub 2018 Nov 22. PMID: 30371963; PMCID: PMC7004038.
85. Buzsáki G. Hippocampal sharp wave-ripple: A cognitive biomarker for episodic memory and planning. Hippocampus. 2015 Oct;25(10):1073-188. doi: 10.1002/hipo.22488. PMID: 26135716; PMCID: PMC4648295.
86. Buzsáki G. Hippocampal sharp wave-ripple: A cognitive biomarker for episodic memory and planning. Hippocampus. 2015 Oct;25(10):1073-188. doi: 10.1002/hipo.22488. PMID: 26135716; PMCID: PMC4648295.
87. den Bakker H, Van Dijck M, Sun J, Kloosterman F. Sharp-wave ripple associated activity in the medial prefrontal cortex supports spatial rule switching. bioRxiv; 2022. DOI: 10.1101/2022.11.03.515023.
88. tM2 muscarinic acetylcholine receptor knock-out mice show deficits in behavioral flexibility, working memory, and hippocampal plasticity. J Neurosci. 2004 Nov 10;24(45):10117-27. doi: 10.1523/JNEUROSCI.3581-04.2004. PMID: 15537882; PMCID: PMC6730182.
89. Robinson J, Manseau F, Ducharme G, Amilhon B, Vigneault E, El Mestikawy S, Williams S. Optogenetic Activation of Septal Glutamatergic Neurons Drive Hippocampal Theta Rhythms. J Neurosci. 2016 Mar 9;36(10):3016-23. doi: 10.1523/JNEUROSCI.2141-15.2016. PMID: 26961955; PMCID: PMC6601761.
90. Liu X, Ramirez S, Pang PT, Puryear CB, Govindarajan A, Deisseroth K, Tonegawa S. Optogenetic stimulation of a hippocampal engram activates fear memory recall. Nature. 2012 Mar 22;484(7394):381-5. doi: 10.1038/nature11028. PMID: 22441246; PMCID: PMC3331914.
91. Robinson NTM, Descamps LAL, Russell LE, Buchholz MO, Bicknell BA, Antonov GK, Lau JYN, Nutbrown R, Schmidt-Hieber C, Häusser M. Targeted Activation of Hippocampal Place Cells Drives Memory-Guided Spatial Behavior. Cell. 2020 Dec 10;183(6):1586-1599.e10. doi: 10.1016/j.cell.2020.09.061. Epub 2020 Nov 6. Erratum in: Cell. 2020 Dec 23;183(7):2041-2042. PMID: 33159859; PMCID: PMC7754708.
92. Tamura K, Takeda M, Setsuie R, Tsubota T, Hirabayashi T, Miyamoto K, Miyashita Y. Conversion of object identity to object-general semantic value in the primate temporal cortex. Science. 2017 Aug 18;357(6352):687-692. doi: 10.1126/science.aan4800. PMID: 28818944.

CHAPTER 2:

1. Aggleton JP. 1986. A description of the amygdalo-hippocampal interconnections in the macaque monkey. Exp. Brain Res. 64(3):515–26
2. Aghajan ZM, Schuette P, Fields TA, Tran ME, Siddiqui SM, et al. 2017. Theta oscillations in the human medial temporal lobe during real-world ambulatory movement. Curr. Biol. 27(24):3743–51.e3
3. Aguirre GK, Detre JA, Alsop DC, D’Esposito M. 1996. The parahippocampus subserves topographical learning in man. Cereb. Cortex 6(6):823–29
4. Amaral DG, Cowan WM. 1980. Subcortical afferents to the hippocampal formation in the monkey. J. Comp. Neurol. 189(4):573–91
5. Amaral DG, Insausti R, Cowan WM. 1987. The entorhinal cortex of the monkey: I. Cytoarchitectonic organization. J. Comp. Neurol. 264(3):326–55

6. Baxter MG, Hadfield WS, Murray EA. 1999. Rhinal cortex lesions produce mild deficits in visual discrimination learning for an auditory secondary reinforcer in rhesus monkeys. Behav. Neurosci. 113(2):243–52
7. Blair HT, Schafe GE, Bauer EP, Rodrigues SM, LeDoux JE. 2001. Synaptic plasticity in the lateral amygdala: a cellular hypothesis of fear conditioning. Learn. Mem. 8(5):229–42
8. Bohbot VD, Copara MS, Gotman J, Ekstrom AD. 2017. Low-frequency theta oscillations in the human hippocampus during real-world and virtual navigation. Nat. Commun. 8:14415
9. Bright IM, Meister MLR, Cruzado NA, Tiganj Z, Howard MW, Buffalo EA. 2019. A temporal record of the past with a spectrum of time constants in the monkey entorhinal cortex. bioRxiv 688341. https://doi.org/10.1101/688341
10. Brodmann K, Garey LJ. 2006. Brodmann's: Localisation in the Cerebral Cortex. Berlin: Springer
11. Buckmaster CA, Eichenbaum H, Amaral DG, Suzuki WA, Rapp PR. 2004. Entorhinal cortex lesions disrupt the relational organization of memory in monkeys. J. Neurosci. 24(44):9811–25
12. Buffalo EA. 2015. Bridging the gap between spatial and mnemonic views of the hippocampal formation. Hippocampus 25(6):713–18
13. Buffalo EA, Ramus SJ, Clark RE, Teng E, Squire LR, Zola SM. 1999. Dissociation between the effects of damage to perirhinal cortex and area TE. Learn. Mem. 6(6):572–99
14. Buffalo EA, Ramus SJ, Squire LR, Zola SM. 2000. Perception and recognition memory in monkeys following lesions of area TE and perirhinal cortex. Learn. Mem. 7(6):375–82
15. Burgess N, Barry C, O'Keefe J. 2007. An oscillatory interference model of grid cell firing. Hippocampus 17(9):801–12
16. Burwell RD. 2006. The parahippocampal region: corticocortical connectivity. Ann. N. Y. Acad. Sci. 911(1):25–42
17. Burwell RD, Amaral DG. 1998. Perirhinal and postrhinal cortices of the rat: interconnectivity and connections with the entorhinal cortex. J. Comp. Neurol. 391(3):293–321
18. Carmichael ST, Clugnet M-C, Price JL. 1994. Central olfactory connections in the macaque monkey. J. Comp. Neurol. 346(3):403–34
19. Carpenter F, Burgess N, Barry C. 2017. Modulating medial septal cholinergic activity reduces medial entorhinal theta frequency without affecting speed or grid coding. Sci. Rep. 7:14573
20. Chaplin TA, Rosa MGP, Lui LL. 2018. Auditory and visual motion processing and integration in the primate cerebral cortex. Front. Neural Circuits 12:93
21. Chen LL, Lin L-H, Green EJ, Barnes CA, McNaughton BL. 1994. Head-direction cells in the rat posterior cortex. Exp. Brain Res. 101(1):8–23
22. Chrobak JJ, Amaral DG. 2007. Entorhinal cortex of the monkey: VII. Intrinsic connections. J. Comp. Neurol. 500(4):612–33
23. Chudasama Y, Izquierdo A, Murray EA. 2009. Distinct contributions of the amygdala and hippocampus to fear expression. Eur. J. Neurosci. 30(12):2327–37
24. Clark BJ, Bassett JP, Wang SS, Taube JS. 2010. Impaired head direction cell representation in the anterodorsal thalamus after lesions of the retrosplenial cortex. J. Neurosci. 30(15):5289–5302
25. Constantinescu AO, O'Reilly JX, Behrens TEJ. 2016. Organizing conceptual knowledge in humans with a gridlike code. Science 352(6292):1464–68
26. Constantinou M, Cogno SG, Elijah DH, Kropff E, Gigg J, et al. 2016. Bursting neurons in the hippocampal formation encode features of LFP rhythms. Front. Comput. Neurosci. 10:133
27. Courellis HS, Nummela SU, Metke M, Diehl GW, Bussell R, et al. 2019. Spatial encoding in primate hippocampus during free navigation. PLOS Biol. 17(12):e3000546
28. Deshmukh SS, Knierim JJ. 2011. Representation of non-spatial and spatial information in the lateral entorhinal cortex. Front. Behav. Neurosci. 5:69
29. Desimone R, Ungerleider LG. 1986. Multiple visual areas in the caudal superior temporal sulcus of the macaque. J. Comp. Neurol. 248(2):164–89

30. Diehl GW, Hon OJ, Leutgeb S, Leutgeb JK. 2017. Grid and nongrid cells in medial entorhinal cortex represent spatial location and environmental features with complementary coding schemes. Neuron 94(1):83–92.e6
31. Doan TP, Lagartos-Donate MJ, Nilssen ES, Ohara S, Witter MP. 2019. Convergent Projections from Perirhinal and Postrhinal Cortices Suggest a Multisensory Nature of Lateral, but Not Medial, Entorhinal Cortex. Cell Rep. 29(3):617-627.e7
32. Doeller CF, Barry C, Burgess N. 2010. Evidence for grid cells in a human memory network. Nature 463(7281):657–61
33. Dolleman-Van Der Weel MJ, Witter MP. 1996. Projections from the nucleus reuniens thalami to the entorhinal cortex, hippocampal field CA1, and the subiculum in the rat arise from different populations of neurons. J. Comp. Neurol. 364(4):637–50
34. Dragoi G, Carpi D, Recce M, Csicsvari J, Buzsáki G. 1999. Interactions between hippocampus and medial septum during sharp waves and theta oscillation in the behaving rat. J. Neurosci. 19(14):6191–99
35. Eichenbaum H. 2017. The role of the hippocampus in navigation is memory. J. Neurophysiol. 117(4):1785–96
36. Eliav T, Geva-Sagiv M, Finkelstein A, Yartsev MM, Rubin A, et al. 2015. Synchronicity without rhythmicity in the hippocampal formation of behaving bats. Soc. Neurosci. Abstr. 632:01
37. Evrard HC. 2019. The organization of the primate insular cortex. Front. Neuroanat. 14:43
38. Fahy FL, Riches IP, Brown MW. 1993. Neuronal activity related to visual recognition memory: long-term memory and the encoding of recency and familiarity information in the primate anterior and medial inferior temporal and rhinal cortex. Exp. Brain Res. 96(3):457–72
39. Fritz J, Mishkin M, Saunders RC. 2005. In search of an auditory engram. PNAS 102(26):9359–64
40. Fyhn M, Molden S, Witter MP, Moser EI, Moser MB. 2004. Spatial representation in the entorhinal cortex. Science 305(5688):1258–64
41. Gaffan D, Murray EA. 1992. Monkeys (Macaca fascicularis) with rhinal cortex ablations succeed in object discrimination learning despite 24-hr intertrial intervals and fail at matching to sample despite double sample presentations. Behav. Neurosci. 106(1):30–38
42. Hafting T, Fyhn M, Molden S, Moser MB, Moser EI. 2005. Microstructure of a spatial map in the entorhinal cortex. Nature 436(7052):801–6
43. Hoffman KL, Dragan MC, Leonard TK, Micheli C, Montefusco-Siegmund R, Valiante TA. 2013. Saccades during visual exploration align hippocampal 3–8 Hz rhythms in human and non-human primates. Front. Syst. Neurosci. 7:43
44. Horner AJ, Bisby JA, Zotow E, Bush D, Burgess N. 2016. Grid-like processing of imagined navigation. Curr. Biol. 26(6):842–47
45. Insausti R, Amaral DG. 2008. Entorhinal cortex of the monkey: IV. Topographical and laminar organization of cortical afferents. J. Comp. Neurol. 509(6):608–41
46. Insausti R, Amaral DG, Cowan WM. 1987a. The entorhinal cortex of the monkey: II. Cortical afferents. J. Comp. Neurol. 264(3):356–95
47. Insausti R, Amaral DG, Cowan WM. 1987b. The entorhinal cortex of the monkey: III. Subcortical afferents. J. Comp. Neurol. 264(3):396–408
48. Jacobs J, Kahana MJ, Ekstrom AD, Mollison MV, Fried I. 2010. A sense of direction in human entorhinal cortex. PNAS 107(14):6487–92
49. Jacobs J, Miller J, Lee SA, Coffey T, Watrous AJ, et al. 2016. Direct electrical stimulation of the human entorhinal region and hippocampus impairs memory. Neuron 92(5):983–90
50. Jacobs J, Weidemann CT, Miller JF, Solway A, Burke JF, et al. 2013. Direct recordings of grid-like neuronal activity in human spatial navigation. Nat. Neurosci. 16(9):1188–90
51. Julian JB, Keinath AT, Frazzetta G, Epstein RA. 2018. Human entorhinal cortex represents visual space using a boundary-anchored grid. Nat. Neurosci. 21(2):191–94
52. Jutras MJ, Buffalo EA. 2010. Recognition memory signals in the macaque hippocampus. PNAS 107(1):401–6

53. Jutras MJ, Buffalo EA. 2014. Oscillatory correlates of memory in non-human primates. NeuroImage 85(2):694–701
54. Jutras MJ, Fries P, Buffalo EA. 2013. Oscillatory activity in the monkey hippocampus during visual exploration and memory formation. PNAS 110(32):13144–49
55. Khan UA, Liu L, Provenzano FA, Berman DE, Profaci CP, et al. 2014. Molecular drivers and cortical spread of lateral entorhinal cortex dysfunction in preclinical Alzheimer's disease. Nat. Neurosci. 17(2):304–11
56. Killian NJ, Jutras MJ, Buffalo EA. 2012. A map of visual space in the primate entorhinal cortex. Nature 491(7426):761–64
57. Killian NJ, Potter SM, Buffalo EA. 2015. Saccade direction encoding in the primate entorhinal cortex during visual exploration. PNAS 112(51):15743–48
58. Komisaruk BR. 1970. Synchrony between limbic system theta activity and rhythmical behavior in rats. J. Comp. Physiol. Psychol. 70(3):482–92
59. Kondo H, Zaborszky L. 2016. Topographic organization of the basal forebrain projections to the perirhinal, postrhinal, and entorhinal cortex in rats. J. Comp. Neurol. 524(12):2503–15
60. LaLumiere RT. 2014. Optogenetic dissection of amygdala functioning. Front. Behav. Neurosci. 8:107
61. Lega BC, Jacobs J, Kahana M. 2012. Human hippocampal theta oscillations and the formation of episodic memories. Hippocampus 22(4):748–61
62. Leonard BW, Amaral DG, Squire LR, Zola-Morgan S. 1995. Transient memory impairment in monkeys with bilateral lesions of the entorhinal cortex. J. Neurosci. 15(8):5637–59
63. Liu AKL, Chang RC-C, Pearce RKB, Gentleman SM. 2015. Nucleus basalis of Meynert revisited: anatomy, history and differential involvement in Alzheimer's and Parkinson's disease. Acta Neuropathol. 3:527–40
64. Maass A, Berron D, Libby LA, Ranganath C, Düzel E. 2015. Functional subregions of the human entorhinal cortex. eLife 4:e06426
65. Meister MLR, Buffalo EA. 2018. Neurons in primate entorhinal cortex represent gaze position in multiple spatial reference frames. J. Neurosci. 38(10):2430–41
66. Mesulam M-M, Mufson EJ, Levey AI, Wainer BH. 1983. Cholinergic innervation of cortex by the basal forebrain: cytochemistry and cortical connections of the septal area, diagonal band nuclei, nucleus basalis (substantia innominata), and hypothalamus in the rhesus monkey. J. Comp. Neurol. 214(2):170–97
67. Meunier M, Bachevalier J, Mishkin M, Murray EA. 1993. Effects on visual recognition of combined and separate ablations of the entorhinal and perirhinal cortex in rhesus monkeys. J. Neurosci. 13(12):5418–32
68. Miller EK, Desimone R. 1994. Parallel neuronal mechanisms for short-term memory. Science 263(5146):520–22
69. Miller EK, Erickson CA, Desimone R. 1996. Neural mechanisms of visual working memory in prefrontal cortex of the macaque. J. Neurosci. 16(16):5154–67
70. Miller EK, Li L, Desimone R. 1993. Activity of neurons in anterior inferior temporal cortex during a short-term memory task. J. Neurosci. 13(4):1460–78
71. Milner B. Disorders of learning and memory after temporal lobe lesions in man. Clin Neurosurg. 1972;19:421–446
72. Mishkin M. A memory system in the monkey. Philos Trans R Soc Lond B Biol Sci. 1982;298(1089):83–95
73. Mitchell SJ, Rawlins JNP, Steward O, Olton DS. 1982. Medial septal area lesions disrupt θ rhythm and cholinergic staining in medial entorhinal cortex and produce impaired radial arm maze behavior in rats. J. Neurosci. 2(3):292–302
74. Murray EA, Mishkin M. 1998. Object recognition and location memory in monkeys with excitotoxic lesions of the amygdala and hippocampus. J. Neurosci. 18(16):6568–82

75. Nau M, Julian JB, Doeller CF. 2018a. How the brain's navigation system shapes our visual experience. Trends Cogn. Sci. 22(9):810–25
76. Nau M, Navarro Schröder T, Bellmund JLS, Doeller CF. 2018b. Hexadirectional coding of visual space in human entorhinal cortex. Nat. Neurosci. 21(2):188–90
77. Naya Y, Chen H, Yang C, Suzuki WA, Squire LR. 2017. Contributions of primate prefrontal cortex and medial temporal lobe to temporal-order memory. PNAS 114(51):13555–60
78. Naya Y, Suzuki WA. 2011. Integrating what and when across the primate medial temporal lobe. Science 333(6043):773–76
79. Nemanic S, Alvarado MC, Bachevalier J. 2004. The hippocampal/parahippocampal regions and recognition memory: insights from visual paired comparison versus object-delayed nonmatching in monkeys. J. Neurosci. 24(8):2013–26
80. O'Keefe J, Dostrovsky J. 1971. The hippocampus as a spatial map: preliminary evidence from unit activity in the freely-moving rat. Brain Res. 34(1):171–75
81. O'Keefe J, Nadel L. 1978. The Hippocampus as a Cognitive Map. Oxford, UK: Clarendon Press
82. Pascalis O, Bachevalier J. 1999. Neonatal aspiration lesions of the hippocampal formation impair visual recognition memory when assessed by paired-comparison task but not by delayed nonmatching-to-sample task. Hippocampus 9(6):609–16
83. Ramón y Cajal S. 1899. Estudios sobre la corteza cerebral humana. I. Corteza visual. Riv. Trimest. Microgr. 4(1):1–63
84. Ramos JMJ. 2014. Essential role of the perirhinal cortex in complex tactual discrimination tasks in rats. Cereb. Cortex 24(8):2068–80
85. Rempel-Clower NL. 2000. The laminar pattern of connections between prefrontal and anterior temporal cortices in the rhesus monkey is related to cortical structure and function. Cereb. Cortex 10(9):851–65
86. Ren Y, Zhang L, Lu Y, Yang H, Westlund KN. 2009. Central lateral thalamic neurons receive noxious visceral mechanical and chemical input in rats. J. Neurophysiol. 102(1):244–58
87. Riches IP, Wilson FAW, Brown MW. 1991. The effects of visual stimulation and memory on neurons of the hippocampal formation and the neighboring parahippocampal gyrus and inferior temporal cortex of the primate. J. Neurosci. 11(6):1763–79
88. Sargolini F, Fyhn M, Hafting T, McNaughton BL, Witter MP, et al. 2006. Conjunctive representation of position, direction, and velocity in entorhinal cortex. Science 312(5774):758–62
89. Saunders RC, Weiskrantz L. 1989. The effects of fornix transection and combined fornix transection, mammillary body lesions and hippocampal ablations on object-pair association memory in the rhesus monkey. Behav. Brain Res. 35(2):85–94
90. Schiller D, Eichenbaum H, Buffalo EA, Davachi L, Foster DJ, et al. 2015. Memory and space: towards an understanding of the cognitive map. J. Neurosci. 35(41):13904–11
91. Schröder TN, Haak KV, Jimenez NIZ, Beckmann CF, Doeller CF. 2015. Functional topography of the human entorhinal cortex. eLife 4:e06738
92. Schroeder CE, Wilson DA, Radman T, Scharfman H, Lakatos P. 2010. Dynamics of active sensing and perceptual selection. Curr. Opin. Neurobiol. 20(2):172–76
93. Setogawa T, Mizuhiki T, Matsumoto N, Akizawa F, Kuboki R, et al. 2019. Neurons in the monkey orbitofrontal cortex mediate reward value computation and decision-making. Commun. Biol. 2:126
94. Solstad T, Boccara CN, Kropff E, Moser MB, Moser EI. 2008. Representation of geometric borders in the entorhinal cortex. Science 322(5909):1865–68
95. Squire LR, Zola-Morgan S. The medial temporal lobe memory system. Science. 1991;253(5026):1380–1386Strange BA, Witter MP, Lein ES, Moser EI. 2014. Functional organization of the hippocampal longitudinal axis. Nat. Rev. Neurosci. 15(10):655–69
96. Suthana N, Haneef Z, Stern J, Mukamel R, Behnke E, et al. 2012. Memory enhancement and deep-brain stimulation of the entorhinal area. N. Engl. J. Med. 366(6):502–10

97. Suzuki WA, Amaral DG. 1994. Topographic organization of the reciprocal connections between the monkey entorhinal cortex and the perirhinal and parahippocampal cortices. J. Neurosci. 14(3):1856–77
98. Suzuki WA, Miller EK, Desimone R. 1997. Object and place memory in the macaque entorhinal cortex. J. Neurophysiol. 78(2):1062–81
99. Talakoub O, Sayegh PF, Womelsdorf T, Zinke W, Fries P, et al. 2019. Hippocampal and neocortical oscillations are tuned to behavioral state in freely-behaving macaques. bioRxiv 552877. https://doi.org/10.1101/552877
100. Tamura K, Takeda M, Setsuie R, Tsubota T, Hirabayashi T, et al. 2017. Conversion of object identity to object-general semantic value in the primate temporal cortex. Science 357(6352):687–92
101. Tsao A, Moser MB, Moser EI. 2013. Traces of experience in the lateral entorhinal cortex. Curr. Biol. 23(5):399–405
102. Tsao A, Sugar J, Lu L, Wang C, Knierim JJ, et al. 2018. Integrating time from experience in the lateral entorhinal cortex. Nature 561(7721):57–62
103. Ulanovsky N, Moss CF. 2007. Hippocampal cellular and network activity in freely moving echolocating bats. Nat. Neurosci. 10(2):224–33
104. Van Hoesen GW, Pandya DN. 1975a. Some connections of the entorhinal (area 28) and perirhinal (area 35) cortices of the rhesus monkey. I. Temporal lobe afferents. Brain Res. 95(1):1–24
105. Van Hoesen GW, Pandya DN. 1975b. Some connections of the entorhinal (area 28) and perirhinal (area 35) cortices of the rhesus monkey. III. Efferent connections. Brain Res. 95(1):39–59
106. Vanderwolf C. 1969. Hippocampal electrical activity and voluntary movement in the rat. Electroencephalogr. Clin. Neurophysiol. 26(4):407–18
107. Vertes RP, Kocsis B. 1997. Brainstem-diencephalo-septohippocampal systems controlling the theta rhythm of the hippocampus. Neuroscience 81(4):893–926
108. Walton ME, Mars RB. 2007. Probing human and monkey anterior cingulate cortex in variable environments. Cogn. Affect. Behav. Neurosci. 7(4):413–22
109. Wilming N, König P, König S, Buffalo EA. 2018. Entorhinal cortex receptive fields are modulated by spatial attention, even without movement. eLife 7:e31745
110. Witter MP. 2007. The perforant path: projections from the entorhinal cortex to the dentate gyrus. Prog. Brain Res. 163:43–61
111. Witter MP, Amaral DG. 1991. Entorhinal cortex of the monkey: V. Projections to the dentate gyrus, hippocampus, and subicular complex. J. Comp. Neurol. 307(3):437–59
112. Witter MP, Doan TP, Jacobsen B, Nilssen ES, Ohara S. 2017. Architecture of the entorhinal cortex a review of entorhinal anatomy in rodents with some comparative notes. Front. Syst. Neurosci. 11:46
113. Witter MP, Van Hoesen GW, Amaral DG. 1989. Topographical organization of the entorhinal projection to the dentate gyrus of the monkey. J. Neurosci. 9(1):216–28
114. Yartsev MM, Ulanovsky N. 2013. Representation of three-dimensional space in the hippocampus of flying bats. Science 340(6130):367–72
115. Yartsev MM, Witter MP, Ulanovsky N. 2011. Grid cells without theta oscillations in the entorhinal cortex of bats. Nature 479(7371):103–7
116. Zola-Morgan S, Squire LR. 1985. Medial temporal lesions in monkeys impair memory on a variety of tasks sensitive to human amnesia. Behavioral Neuroscience, 99(1), 22–34
117. Zola SM, Squire LR, Teng E, Stefanacci L, Buffalo EA, Clark RE. 2000. Impaired recognition memory in monkeys after damage limited to the hippocampal region. J. Neurosci. 20(1):451–63

CHAPTER 3:

1. Boyden, E.S.; Zhang, F.; Bamberg, E.; Nagel, G.; Deisseroth, K. Millisecond-timescale, genetically targeted optical control of neural activity. Nat. Neurosci. 2005, 8, 1263–1268.
2. Yizhar, O.; Fenno, L.E.; Davidson, T.J.; Mogri, M.; Deisseroth, K. Optogenetics in neural systems. Neuron 2011, 71, 9–34.
3. Ting, J.T.; Feng, G. Recombineering strategies for developing next generation BAC transgenic tools for optogenetics and beyond. Front. Behav. Neurosci. 2014, 8, 1–13.
4. Mehta, A.M.; Sonabend, A.M.; Bruce, J.N. Convection-Enhanced Delivery. Neurotherapeutics 2017, 14, 358–371.
5. René, C.A.; Parks, R.J. Delivery of therapeutic agents to the central nervous system and the promise of extracellular vesicles. Pharmaceutics 2021, 13, 492.
6. Bobo, R.H.; Laske, D.W.; Akbasak, A.; Morrison, P.F.; Dedrick, R.L.; Oldfield, E.H. Convection-enhanced delivery of macromolecules in the brain. Proc. Natl. Acad. Sci. USA 1994, 91, 2076–2080.
7. Krauze, M.T.; Saito, R.; Noble, C.; Tamas, M.; Bringas, J.; Park, J.W.; Berger, M.S.; Bankiewicz, K. Reflux-free cannula for convection-enhanced high-speed delivery of therapeutic agents. J. Neurosurg. 2005, 103, 923–929.
8. Yazdan-Shahmorad, A.; Diaz-Botia, C.; Hanson, T.L.; Kharazia, V.; Ledochowitsch, P.; Maharbiz, M.M.; Sabes, P.N. “A Large-Scale Interface for Optogenetic Stimulation and Recording in Nonhuman Primates. Neuron 2016, 89, 927–939.
9. Yazdan-Shahmorad, A.; Tian, N.; Kharazia, V.; Samaranch, L.; Kells, A.; Bringas, J.; He, J.; Bankiewicz, K.; Sabes, P.N. Widespread optogenetic expression in macaque cortex obtained with MR-guided, convection enhanced delivery (CED) of AAV vector to the thalamus. J. Neurosci. Methods 2018, 293, 347–358.
10. Lieberman, D.M.; Laske, D.W.; Morrison, P.F.; Bankiewicz, K.S.; Oldfield, E.H. Convection-enhanced distribution of large molecules in gray matter during interstitial drug infusion. J. Neurosurg. 1995, 82, 1021–1029.
11. Lonser, R.R.; Gogate, N.; Morrison, P.F.; Wood, J.D.; Oldfield, E.H. Direct convective delivery of macromolecules to the spinal cord. J. Neurosurg. 1998, 89, 616–622.
12. Lonser, R.R.; Walbridge, S.; Garmestani, K.; Butman, J.A.; Walters, H.A.; Vortmeyer, O.; Morrison, P.F.; Brechbiel, M.W.; Oldfield, E.H. Successful and safe perfusion of the primate brainstem: In vivo magnetic resonance imaging of macromolecular distribution during infusion. J. Neurosurg. 2002, 97, 905–913.
13. Sanftner, L.M.; Sommer, J.M.; Suzuki, B.M.; Smith, P.H.; Vijay, S.; Vargas, J.A.; Forsayeth, J.R.; Cunningham, J.; Bankiewicz, K.S.; Kao, H.; et al. AAV2-mediated gene delivery to monkey putamen: Evaluation of an infusion device and delivery parameters. Exp. Neurol. 2005, 194, 476–483.
14. Szerlip, N.J.; Walbridge, S.; Yang, L.; Morrison, P.F.; Degen, J.W.; Jarrell, S.T.; Kouri, J.; Kerr, P.B.; Kotin, R.; Oldfield, E.H.; et al. Real-time imaging of convection-enhanced delivery of viruses and virus-sized particles. J. Neurosurg. 2007, 107, 560–567.
15. Kells, A.P.; Hadaczek, P.; Yin, D.; Bringas, J.; Varenika, V.; Forsayeth, J.; Bankiewicz, K.S. Efficient gene therapy-based method for the delivery of therapeutics to primate cortex. Proc. Natl. Acad. Sci. USA 2009, 106, 2407–2411.
16. Yazdan-Shahmorad, A.; Diaz-Botia, C.; Hanson, T.; Ledochowitsch, P.; Maharabiz, M.M.; Sabes, P.N. Demonstration of a setup for chronic optogenetic stimulation and recording across cortical areas in non-human primates. SPIE BiOS 2015, 9305, 231–236.
17. Macknik, S.L.; Alexander, R.G.; Caballero, O.; Chanovas, J.; Nielsen, K.J.; Nishimura, N.; Schaffer, C.B.; Slovin, H.; Babayoff, A.; Barak, R.; et al. Advanced Circuit and Cellular Imaging Methods in Nonhuman Primates. J. Neurosci. 2019, 39, 8267–8274.

18. Khateeb, K.; Griggs, D.J.; Sabes, P.N.; Yazdan-Shahmorad, A. Convection Enhanced Delivery of Optogenetic Adeno-associated Viral Vector to the Cortex of Rhesus Macaque Under Guidance of Online MRI Images. J. Vis. Exp. 2019, 147, e59232.
19. Ojemann, W.K.; Griggs, D.J.; Ip, Z.; Caballero, O.; Jahanian, H.; Martinez-Conde, S.; Macknik, S.; Yazdan-Shahmorad, A. A mri-based toolbox for neurosurgical planning in nonhuman primates. J. Vis. Exp. 2020, 2020, e61098.
20. Chen, Z.J.; Gillies, G.T.; Broaddus, W.C.; Prabhu, S.S.; Fillmore, H.; Mitchell, R.M.; Corwin, F.D.; Fatouros, P.P. A realistic brain tissue phantom for intraparenchymal infusion studies. J. Neurosurg. 2004, 101, 314–322.
21. Pomfret, R.; Miranpuri, G.; Sillay, K. The substitute brain and the potential of the gel model. Ann. Neurosci. 2013, 20, 118–122.
22. Yazdan-Shahmorad, A.; Silversmith, D.B.; Kharazia, V.; Sabes, P.N. Targeted cortical reorganization using optogenetics in non-human primates. eLife 2018, 7, e31034.
23. Yazdan-Shahmorad, A.; Hanson, T.; Tian, N.; He, J.; Sabes, P. A novel technique for infusion of optogenetics viral vectors in nonhuman primates (NHPs) cortex using MR-guided convection enhanced delivery (CED). In Proceedings of the 6th International IEEE/EMBS Conference on Neural Engineering (NER), San Diego, CA, USA, 6–8 November 2013; pp. 5–8.
24. Klapoetke, N.C.; Murata, Y.; Kim, S.S.; Pulver, S.R.; Birdsey-Benson, A.; Cho, Y.K.; Morimoto, T.K.; Chuong, A.S.; Carpenter, E.J.; Tian, Z.; et al. Independent optical excitation of distinct neural populations. Nat. Methods 2014, 11, 338–346.
25. Mao, T.; Kusefoglu, D.; Hooks, B.M.; Huber, D.; Petreanu, L.; Svoboda, K. Long-Range Neuronal Circuits Underlying the Interaction between Sensory and Motor Cortex. Neuron 2011, 72, 111–123.
26. Fredericks, J.M.; Dash, K.E.; Jaskot, E.M.; Bennett, T.W.; Lerchner, W.; Dold, G.; Ide, D.; Cummins, A.C.; Der Minassian, V.H.; Turchi, J.N.; et al. Methods for mechanical delivery of viral vectors into rhesus monkey brain. J. Neurosci. Methods 2020, 339, 108730.
27. Prezelski, K.; Keiser, M.; Stein, J.M.; Lucas, T.H.; Davidson, B.; Gonzalez-Alegre, P.; Vitale, F. Design and Validation of a MultiPoint Injection Technology for MR-Guided Convection Enhanced Delivery in the Brain. Front. Med. Technol. 2021, 3, 1–12.
28. Seunguk, O.H.; Odland, R.; Wilson, S.R.; Kroeger, K.M.; Liu, C.; Lowenstein, P.R.; Castro, M.G.; Hall, W.A.; Ohlfest, J.R. “Improved distribution of small molecules and viral vectors in the murine brain using a hollow fiber catheter. J. Neurosurg. 2007, 107, 568–577.
29. Tremblay, S.; Acker, L.; Afraz, A.; Albaugh, D.L.; Amita, H.; Andrei, A.R.; Angelucci, A.; Aschner, A.; Balan, P.F.; Basso, M.A.; et al. An Open Resource for Non-human Primate Optogenetics. Neuron 2020, 108, 1075–1090.
30. Belloir, T.; Montalgo Vargo, S.; Ahmed, Z.; Griggs, D.; Fisher, S.; Brown, T.; Chamanzar, M.; Yazdan-Shahmorad, A. Large-scale multimodal surface neural interfaces for non-human primates. iScience. under revision.
31. Bloch, J.; Shea-brown, E.; Harchaoui, Z.; Shojai, A. E Network structure mediates functional reorganization induced by optogenetic stimulation of non-human primate sensorimotor cortex. iScience 2022, 25, 104285.
32. Griggs, D.J.; Belloir, T.; Yazdan-Shahmorad, A. Large-scale neural interfaces for optogenetic actuators and sensors in non-human primates. SPIE BiOS 2021, 1166305, 17.
33. Griggs, D.J.; Bloch, J.; Fisher, S.; Ojemann, W.K.S.; Coubrough, K.M.; Khateeb, K.; Chu, M.; Yazdan-Shahmorad, A. Demonstration of an Optimized Large-scale Optogenetic Cortical Interface for Non-human Primates. IEEE EMBC 2022, 119395, 7–15.
34. Griggs, D.J.; Khateeb, K.; Philips, S.; Chan, J.W.; Ojemann, W.K.S.; Yazdan-Shahmorad, A. Optimized large-scale optogenetic interface for non-human primates. SPIE BiOS 2019, 1086605, 3.

35. Griggs, D.J.; Khateeb, K.; Zhou, J.; Liu, T.; Wang, R.; Yazdan-Shahmorad, A. Multi-modal artificial dura for simultaneous large-scale optical access and large-scale electrophysiology in non-human primate cortex. J. Neural Eng. 2021, 18, 055006.
36. Komatsu, M.; Sugano, E.; Tomita, H.; Fujii, N. A chronically implantable bidirectional neural interface for non-human primates. Front. Neurosci. 2017, 11, 514.
37. Ledochowitsch, P.; Yazdan-Shahmorad, A.; Bouchard, K.E.; Diaz-Botia, C.; Hanson, T.L.; He, J.W.; Seybold, B.A.; Olivero, E.; Phillips, E.A.; Blanche, T.J.; et al. Strategies for optical control and simultaneous electrical readout of extended cortical circuits. J. Neurosci. Methods 2015, 256, 220–231.
38. Rajalingham, R.; Sorenson, M.; Azadi, R.; Bohn, S.; DiCarlo, J.J.; Afraz, A. Chronically implantable LED arrays for behavioral optogenetics in primates. Nat. Methods 2021, 18, 1112–1116.
39. Yazdan-Shahmorad, A.; Silversmith, D.B.; Sabes, P.N. Novel techniques for large-scale manipulations of cortical networks in non-human primates. In Proceedings of the 40th Annual International Conference of the IEEE Engineering in Medicine and Biology Society (EMBC), Honolulu, HI, USA, 17–21 July 2018; pp. 5479–5482.
40. Strange, B.A.; Witter, M.P.; Lein, E.S.; Moser, E.I. Functional organization of the hippocampal longitudinal axis. Nat. Rev. Neurosci. 2014, 15, 655–669.
41. Zola, S.M.; Squire, L.R.; Teng, E.; Stefanacci, L.; Buffalo, E.A.; Clark, R.E. Impaired recognition memory in monkeys after damage limited to the hippocampal region. J. Neurosci. 2000, 20, 451–463.
42. Hampton, R.R.; Buckmaster, C.A.; Anuszkiewicz-Lundgren, D.; Murray, E.A. Method for making selective lesions of the hippocampus in Macaque monkeys using NMDA and a longitudinal surgical approach. Hippocampus 2004, 14, 9–18.
43. Simmons, J.M.; Saad, Z.S.; Lizak, M.J.; Ortiz, M.; Koretsky, A.P.; Richmond, B.J. Mapping prefrontal circuits in vivo with manganese-enhanced magnetic resonance imaging in monkeys. J. Neurosci. 2008, 28, 7637–7647.
44. Russell, W.; Burch, R. The Principles of Humane Experimental Technique; Methuen: London, UK, 1959.
45. Prescott, M.J.; Poirier, C. The role of MRI in applying the 3Rs to non-human primate neuroscience. Neuroimage 2021, 225, 117521.

CHAPTER 4:

1. Liu AA, Henin S, Abbaspoor S, Bragin A, Buffalo EA, Farrell JS, Foster DJ, Frank LM, Gedankien T, Gotman J, Guidera JA, Hoffman KL, Jacobs J, Kahana MJ, Li L, Liao Z, Lin JJ, Losonczy A, Malach R, van der Meer MA, McClain K, McNaughton BL, Norman Y, Navas-Olive A, de la Prida LM, Rueckemann JW, Sakon JJ, Skelin I, Soltesz I, Staresina BP, Weiss SA, Wilson MA, Zaghloul KA, Zugaro M, Buzsáki G. A consensus statement on detection of hippocampal sharp wave ripples and differentiation from other fast oscillations. Nat Commun. 2022 Oct 12;13(1):6000. doi: 10.1038/s41467-022-33536-x. PMID: 36224194; PMCID: PMC9556539.
2. Buzsáki G, Leung LW, Vanderwolf CH. Cellular bases of hippocampal EEG in the behaving rat. Brain Res. 1983 Oct;287(2):139-71. doi: 10.1016/0165-0173(83)90037-1. PMID: 6357356.
3. Colgin LL. Five Decades of Hippocampal Place Cells and EEG Rhythms in Behaving Rats. J Neurosci. 2020 Jan 2;40(1):54-60. doi: 10.1523/JNEUROSCI.0741-19.2019. Epub 2019 Aug 26. PMID: 31451578; PMCID: PMC6939480.
4. Sullivan D, Csicsvari J, Mizuseki K, Montgomery S, Diba K, Buzsáki G. Relationships between hippocampal sharp waves, ripples, and fast gamma oscillation: influence of dentate and entorhinal cortical activity. J Neurosci. 2011 Jun 8;31(23):8605-16. doi: 10.1523/JNEUROSCI.0294-11.2011. PMID: 21653864; PMCID: PMC3134187.

5. Csicsvari J, Hirase H, Czurkó A, Mamiya A, Buzsáki G. Fast network oscillations in the hippocampal CA1 region of the behaving rat. J Neurosci. 1999 Aug 15;19(16):RC20. doi: 10.1523/JNEUROSCI.19-16-j0001.1999. PMID: 10436076; PMCID: PMC6782850.
6. Yu JY, Kay K, Liu DF, Grossrubatscher I, Loback A, Sosa M, Chung JE, Karlsson MP, Larkin MC, Frank LM. Distinct hippocampal-cortical memory representations for experiences associated with movement versus immobility. Elife. 2017 Aug 3;6:e27621. doi: 10.7554/eLife.27621. PMID: 28826483; PMCID: PMC5576488.
7. Vanderwolf CH. Hippocampal electrical activity and voluntary movement in the rat. Electroencephalogr Clin Neurophysiol. 1969 Apr;26(4):407-18. doi: 10.1016/0013-4694(69)90092-3. PMID: 4183562.
8. Lee AK, Wilson MA. Memory of sequential experience in the hippocampus during slow wave sleep. Neuron. 2002 Dec 19;36(6):1183-94. doi: 10.1016/s0896-6273(02)01096-6. PMID: 12495631.
9. Girardeau G, Benchenane K, Wiener SI, Buzsáki G, Zugaro MB. Selective suppression of hippocampal ripples impairs spatial memory. Nat Neurosci. 2009 Oct;12(10):1222-3. doi: 10.1038/nn.2384. Epub 2009 Sep 13. PMID: 19749750.
10. Jadhav SP, Kemere C, German PW, Frank LM. Awake hippocampal sharp-wave ripples support spatial memory. Science. 2012 Jun 15;336(6087):1454-8. doi: 10.1126/science.1217230. Epub 2012 May 3. PMID: 22555434; PMCID: PMC4441285.
11. Jadhav SP, Kemere C, German PW, Frank LM. Awake hippocampal sharp-wave ripples support spatial memory. Science. 2012 Jun 15;336(6087):1454-8. doi: 10.1126/science.1217230. Epub 2012 May 3. PMID: 22555434; PMCID: PMC4441285.
12. Hussin AT, Leonard TK, Hoffman KL. Sharp-wave ripple features in macaques depend on behavioral state and cell-type specific firing. Hippocampus. 2020 Jan;30(1):50-59. doi: 10.1002/hipo.23046. Epub 2018 Nov 22. PMID: 30371963; PMCID: PMC7004038.
13. Patel J, Schomburg EW, Berényi A, Fujisawa S, Buzsáki G. Local generation and propagation of ripples along the septotemporal axis of the hippocampus. J Neurosci. 2013 Oct 23;33(43):17029-41. doi: 10.1523/JNEUROSCI.2036-13.2013. PMID: 24155307; PMCID: PMC3807028.
14. Strange BA, Witter MP, Lein ES, Moser EI. Functional organization of the hippocampal longitudinal axis. Nat Rev Neurosci. 2014 Oct;15(10):655-69. doi: 10.1038/nrn3785. PMID: 25234264.
15. Chawla, MPS. PCA and ICA processing methods for removal of artifacts and noise in electrocardiograms: A survey and comparison. Appl. Soft Comput. 11 (2011): 2216-2226.
16. Kaczorowska, M, Plechawska-Wójcik, M, Tokovarov, M, & Dmytruk, R (2017). Comparison of the ICA and PCA methods in correction of EEG signal artefacts. 2017 10th International Symposium on Advanced Topics in Electrical Engineering (ATEE), 262-267.
17. Maier N, Nimmrich V, Draguhn A. Cellular and network mechanisms underlying spontaneous sharp wave-ripple complexes in mouse hippocampal slices. J Physiol. 2003 Aug 1;550(Pt 3):873-87. doi: 10.1113/jphysiol.2003.044602. Epub 2003 Jun 13. PMID: 12807984; PMCID: PMC2343079.
18. Ylinen A, Bragin A, Nádasdy Z, Jandó G, Szabó I, Sik A, Buzsáki G. Sharp wave-associated high-frequency oscillation (200 Hz) in the intact hippocampus: network and intracellular mechanisms. J Neurosci. 1995 Jan;15(1 Pt 1):30-46. doi: 10.1523/JNEUROSCI.15-01-00030.1995. PMID: 7823136; PMCID: PMC6578299.
19. Kondo H, Lavenex P, Amaral DG. Intrinsic connections of the macaque monkey hippocampal formation: II. CA3 connections. J Comp Neurol. 2009 Jul 20;515(3):349-77. doi: 10.1002/cne.22056. PMID: 19425110; PMCID: PMC4386899.
20. Imbrosci B, Nitzan N, McKenzie S, Donoso JR, Swaminathan A, Böhm C, Maier N, Schmitz D. Subiculum as a generator of sharp wave-ripples in the rodent hippocampus. Cell Rep. 2021 Apr 20;35(3):109021. doi: 10.1016/j.celrep.2021.109021. PMID: 33882307; PMCID: PMC9239734.

21. Sullivan D, Csicsvari J, Mizuseki K, Montgomery S, Diba K, Buzsáki G. Relationships between hippocampal sharp waves, ripples, and fast gamma oscillation: influence of dentate and entorhinal cortical activity. J Neurosci. 2011 Jun 8;31(23):8605-16. doi: 10.1523/JNEUROSCI.0294-11.2011. PMID: 21653864; PMCID: PMC3134187.
22. Mölle M, Yeshenko O, Marshall L, Sara SJ, Born J. Hippocampal sharp wave-ripples linked to slow oscillations in rat slow-wave sleep. J Neurophysiol. 2006 Jul;96(1):62-70. doi: 10.1152/jn.00014.2006. Epub 2006 Apr 12. PMID: 16611848.
23. Tang W, Jadhav SP. Sharp-wave ripples as a signature of hippocampal-prefrontal reactivation for memory during sleep and waking states. Neurobiol Learn Mem. 2019 Apr;160:11-20. doi: 10.1016/j.nlm.2018.01.002. Epub 2018 Jan 10. PMID: 29331447; PMCID: PMC6039287.
24. Skelin I, Zhang H, Zheng J, Ma S, Mander BA, Kim McManus O, Vadera S, Knight RT, McNaughton BL, Lin JJ. Coupling between slow waves and sharp-wave ripples engages distributed neural activity during sleep in humans. Proc Natl Acad Sci U S A. 2021 May 25;118(21):e2012075118. doi: 10.1073/pnas.2012075118. PMID: 34001599; PMCID: PMC8166184.
25. Joo HR, Frank LM. The hippocampal sharp wave-ripple in memory retrieval for immediate use and consolidation. Nat Rev Neurosci. 2018 Dec;19(12):744-757. doi: 10.1038/s41583-018-0077-1. PMID: 30356103; PMCID: PMC6794196.
26. Isaacson JS, Scanziani M. How inhibition shapes cortical activity. Neuron. 2011 Oct 20;72(2):231-43. doi: 10.1016/j.neuron.2011.09.027. PMID: 22017986; PMCID: PMC3236361.
27. Skaggs WE, McNaughton BL, Permenter M, Archibeque M, Vogt J, Amaral DG, Barnes CA. EEG sharp waves and sparse ensemble unit activity in the macaque hippocampus. J Neurophysiol. 2007 Aug;98(2):898-910. doi: 10.1152/jn.00401.2007. Epub 2007 May 23. PMID: 17522177.

CHAPTER 5:

1. Buzsáki G, Anastassiou CA, Koch C. The origin of extracellular fields and currents--EEG, ECoG, LFP and spikes. Nat Rev Neurosci. 2012 May 18;13(6):407-20. doi: 10.1038/nrn3241. PMID: 22595786; PMCID: PMC4907333.
2. Gui DY, Yu T, Hu Z, Yan J, Li X. Dissociable functional activities of cortical theta and beta oscillations in the lateral prefrontal cortex during intertemporal choice. Sci Rep. 2018 Jul 25;8(1):11233. doi: 10.1038/s41598-018-21150-1. Erratum in: Sci Rep. 2019 Aug 15;9(1):12141. PMID: 30046152; PMCID: PMC6060123.
3. Khanna P, Carmena JM. Beta band oscillations in motor cortex reflect neural population signals that delay movement onset. Elife. 2017 May 3;6:e24573. doi: 10.7554/eLife.24573. PMID: 28467303; PMCID: PMC5468088.
4. Vijayan S, Lepage KQ, Kopell NJ, Cash SS. Frontal beta-theta network during REM sleep. Elife. 2017 Jan 25;6:e18894. doi: 10.7554/eLife.18894. PMID: 28121613; PMCID: PMC5266493.
5. Vanderwolf CH. Hippocampal electrical activity and voluntary movement in the rat. Electroencephalogr Clin Neurophysiol. 1969 Apr;26(4):407-18. doi: 10.1016/0013-4694(69)90092-3. PMID: 4183562.
6. Colgin LL. Five Decades of Hippocampal Place Cells and EEG Rhythms in Behaving Rats. J Neurosci. 2020 Jan 2;40(1):54-60. doi: 10.1523/JNEUROSCI.0741-19.2019. Epub 2019 Aug 26. PMID: 31451578; PMCID: PMC6939480.
7. Feng T, Silva D, Foster DJ. Dissociation between the experience-dependent development of hippocampal theta sequences and single-trial phase precession. J Neurosci. 2015 Mar 25;35(12):4890-902. doi: 10.1523/JNEUROSCI.2614-14.2015. PMID: 25810520; PMCID: PMC4389593.

8. Kleinfeld D, Deschênes M, Ulanovsky N. Whisking, Sniffing, and the Hippocampal θ-Rhythm: A Tale of Two Oscillators. PLoS Biol. 2016 Feb 18;14(2):e1002385. doi: 10.1371/journal.pbio.1002385. PMID: 26890361; PMCID: PMC4758648.
9. Brandon MP, Koenig J, Leutgeb JK, Leutgeb S. New and distinct hippocampal place codes are generated in a new environment during septal inactivation. Neuron. 2014 May 21;82(4):789-96. doi: 10.1016/j.neuron.2014.04.013. PMID: 24853939; PMCID: PMC4294702.
10. Jutras MJ, Fries P, Buffalo EA. Oscillatory activity in the monkey hippocampus during visual exploration and memory formation. Proc Natl Acad Sci U S A. 2013 Aug 6;110(32):13144-9. doi: 10.1073/pnas.1302351110. Epub 2013 Jul 22. PMID: 23878251; PMCID: PMC3740906.
11. Mao D, Avila E, Caziot B, Laurens J, Dickman JD, Angelaki DE. Spatial modulation of hippocampal activity in freely moving macaques. Neuron. 2021 Nov 3;109(21):3521-3534.e6. doi: 10.1016/j.neuron.2021.09.032. Epub 2021 Oct 12. PMID: 34644546; PMCID: PMC8571030.
12. Browning JI, Buffalo EA. Monkey Hippocampal Neurons Track Ongoing Experiences. UW Libraries. 2021.
13. Baraduc P, Duhamel JR, Wirth S. Schema cells in the macaque hippocampus. Science. 2019 Feb 8;363(6427):635-639. doi: 10.1126/science.aav5404. PMID: 30733419.
14. Altemus KL, Lavenex P, Ishizuka N, Amaral DG. Morphological characteristics and electrophysiological properties of CA1 pyramidal neurons in macaque monkeys. Neuroscience. 2005;136(3):741-56. doi: 10.1016/j.neuroscience.2005.07.001. PMID: 16344148.
15. Trimper JB, Galloway CR, Jones AC, Mandi K, Manns JR. Gamma Oscillations in Rat Hippocampal Subregions Dentate Gyrus, CA3, CA1, and Subiculum Underlie Associative Memory Encoding. Cell Rep. 2017 Nov 28;21(9):2419-2432. doi: 10.1016/j.celrep.2017.10.123. PMID: 29186681; PMCID: PMC5728687.
16. Herreras O. Local Field Potentials: Myths and Misunderstandings. Front Neural Circuits. 2016 Dec 15;10:101. doi: 10.3389/fncir.2016.00101. PMID: 28018180; PMCID: PMC5156830.
17. Harner RN. Singular value decomposition--a general linear model for analysis of multivariate structure in the electroencephalogram. Brain Topogr. 1990 Fall;3(1):43-7. doi: 10.1007/BF01128860. PMID: 2094312.
18. Cohen MX. A better way to define and describe Morlet wavelets for time-frequency analysis. Neuroimage. 2019 Oct 1;199:81-86. doi: 10.1016/j.neuroimage.2019.05.048. Epub 2019 May 27. PMID: 31145982.
19. Talakoub O, Sayegh P, Womelsdorf T, Zinke W, Fries P, Lewis CM, Hoffman KL. Hippocampal and neocortical oscillations are tuned to behavioral state in freely-behaving macaques. BioRxiv. 2019 Feb 18; 552877; doi: https://doi.org/10.1101/552877
20. Kaczorowska, M, Plechawska-Wójcik, M, Tokovarov, M, & Dmytruk, R (2017). Comparison of the ICA and PCA methods in correction of EEG signal artefacts. 2017 10th International Symposium on Advanced Topics in Electrical Engineering (ATEE), 262-267.
21. Chawla, MPS. PCA and ICA processing methods for removal of artifacts and noise in electrocardiograms: A survey and comparison. Appl. Soft Comput. 11 (2011): 2216-2226.

CHAPTER 6:

1. Nilssen ES, Doan TP, Nigro MJ, Ohara S, Witter MP. Neurons and networks in the entorhinal cortex: A reappraisal of the lateral and medial entorhinal subdivisions mediating parallel cortical pathways. Hippocampus. 2019 Dec;29(12):1238-1254. doi: 10.1002/hipo.23145. Epub 2019 Aug 13. Erratum in: Hippocampus. 2020 Aug;30(8):909. PMID: 31408260.
2. Jarzebowski P, Tang CS, Paulsen O, Hay YA. Impaired spatial learning and suppression of sharp wave ripples by cholinergic activation at the goal location. Elife. 2021 Apr 6;10:e65998. doi: 10.7554/eLife.65998. PMID: 33821790; PMCID: PMC8064750.

3. Robinson J, Manseau F, Ducharme G, Amilhon B, Vigneault E, El Mestikawy S, Williams S. Optogenetic Activation of Septal Glutamatergic Neurons Drive Hippocampal Theta Rhythms. J Neurosci. 2016 Mar 9;36(10):3016-23. doi: 10.1523/JNEUROSCI.2141-15.2016. PMID: 26961955; PMCID: PMC6601761.
4. Jutras MJ, Fries P, Buffalo EA. Oscillatory activity in the monkey hippocampus during visual exploration and memory formation. Proc Natl Acad Sci U S A. 2013 Aug 6;110(32):13144-9. doi: 10.1073/pnas.1302351110. Epub 2013 Jul 22. PMID: 23878251; PMCID: PMC3740906.
5. Mao D, Avila E, Caziot B, Laurens J, Dickman JD, Angelaki DE. Spatial modulation of hippocampal activity in freely moving macaques. Neuron. 2021 Nov 3;109(21):3521-3534.e6. doi: 10.1016/j.neuron.2021.09.032. Epub 2021 Oct 12. PMID: 34644546; PMCID: PMC8571030.
6. Talakoub O, Sayegh P, Womelsdorf T, Zinke W, Fries P, Lewis CM, Hoffman KL. Hippocampal and neocortical oscillations are tuned to behavioral state in freely-behaving macaques. BioRxiv. 2019 Feb 18; 552877; doi: https://doi.org/10.1101/552877
7. Vandecasteele M, Varga V, Berényi A, Papp E, Barthó P, Venance L, Freund TF, Buzsáki G. Optogenetic activation of septal cholinergic neurons suppresses sharp wave ripples and enhances theta oscillations in the hippocampus. Proc Natl Acad Sci U S A. 2014 Sep 16;111(37):13535-40. doi: 10.1073/pnas.1411233111. Epub 2014 Sep 2. PMID: 25197052; PMCID: PMC4169920.
8. Stewart M, Fox SE. Hippocampal theta activity in monkeys. Brain Res. 1991 Jan 4;538(1):59-63. doi: 10.1016/0006-8993(91)90376-7. PMID: 2018932.